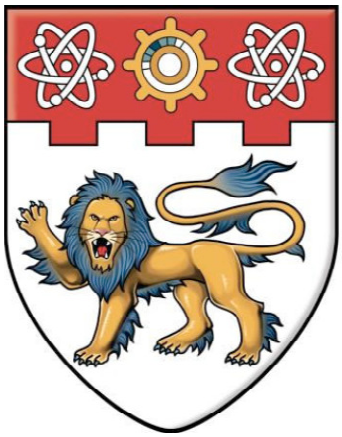

NANYANG TECHNOLOGICAL UNIVERSITY

SYNTHESIS, STRUCTURE AND PROPERTIES OF LEAD-FREE PIEZOELECTRIC CERAMICS

TAN CHEE KIANG, IVAN

School of Materials Science and Engineering

2013

SYNTHESIS, STRUCTURE AND PROPERTIES OF LEAD-FREE PIEZOELECTRIC CERAMICS

TAN CHEE KIANG, IVAN

School of Materials Science and Engineering

A thesis submitted to the Nanyang Technological University in fulfillment of the requirement for the degree of Doctor of Philosophy

2013

Acknowledgements

First I would like to thank my supervisors, Dr Yao Kui from IMRE (Institute of Materials Research and Engineering), Associate Professor Thirumany Sritharan from NTU (Nanyang Technological University) as well as the late Prof. Ma Jan for their kind support, invaluable advices and supervision throughout the course of my PhD study. I gratefully acknowledge their time spent on reading and revising my manuscript patiently.

In addition, I have also received great assistances from several staff members in IMRE. I would like to express my gratitude to the following people: Mr Lim Poh Chong and Ms Lim Suo Hon for their valuable discussions on XRD results, Dr Zhang Tian Shu for his vast experience on ceramic processing, Dr Loh Xian Jun and Dr Liu Kerh Li for sharing their expertise on polymer chemistry, Ms Christina Tan Yuan Ling for laboratory assistances and the late Mr Tan Choon Wah (Physics workshop manager) at NUS for his kind technical advice. Furthermore, I would also like to thank my fellow colleagues: Dr Shannigrahi Santiranjan, Dr Jiang Ying, Dr Lim Yee Fun, Dr Zhang Lei, Dr Goh Phoi Chin, Dr Meysam Sharifzadeh Mirshekarloo, Ms Gan Bee Keen, Ms Sharon Oh Su Yin, Dr Tan Chin Yaw, Ms Alicia Huang Li Xia, Ms Tan Sze Yu, Mr Wong Ting Chong, Dr Dennis Tan Cheng Cheh, Dr Davy Cheong Wun Chet and Dr Wang Wei for helping me and discussing on technical issues. I also greatly appreciate the assistances from attachment students at IMRE: Derrick Ang Eng Seng, Indran, Gu Wen Yi, Tan Jun Ming, Song Xiao Feng, Liu Li Fu and Peter Low.

I gratefully acknowledged the financial supports received from A*STAR (Agency for Science, Technology and Research) under scientific staff development award.

Finally, I wish to thank my parents, parents-in-law and friends for their encouragement, understanding and constant support during my PhD studies. Although there

are a lots of personal problems encountered, they have accompanied me and faced them together all these years.

Last, but not least, I appreciate Shang Di, the Creator, who is behind all marvelous creation. My heartfelt thanks to my beloved wife, Tiffany Tham Lai San, her constant support, love, sacrifice for me and our daughters, Curie Tan Jing En and Cara Tan Jing Ci, and they have always been a source of motivation and bundles of happiness to me.

Table of Contents

Abstract

Since the discovery of $PbZrO_3$-$PbTiO_3$ (PZT) ceramic in 1950s, lead-based piezoelectric materials have been widely used in sensors, actuators, transducers and many other electronic devices. The increasing application of these devices generates increasingly aggravated health and environmental concerns because these conventional lead-based ceramics contain more than 60% of lead by weight. During recent years, intensive efforts have been made to develop lead-free alternatives.

Candidates of the lead-free ceramic systems $0.94(K_{0.5}Na_{0.5})NbO_3$-$0.06LiNbO_3$ (0.94KNN-0.06LN) and $0.5Ba(Zr_{0.2}Ti_{0.8})O_3$-$0.5(Ba_{0.7}Ca_{0.3})TiO_3$ (0.5BZT-0.5BCT) exhibit promising properties with application potential among the lead-free piezoelectric ceramics. Hence, they are chosen for the current investigation in this project. However, lead-free KNN based ceramics usually suffer from volatile loss of the alkali ions during the calcination process, which is more serious before the formation of the perovskite structure. This leads to stoichiometry deviation and consequent degradation of properties. Therefore, special attention should be paid to suppress alkali volatility by promoting synthesis at lower temperatures. Another problem with solid state synthesis involves the long hours of ball milling, which is time consuming and is a potential source for contamination.

Two approaches are investigated in this project to address alkali volatility. Firstly, ultrasonic irradiation during synthesis is systematically studied. Results show that ultrasonic irradiation facilitates the carbonate decomposition and promotes the formation of perovskite phase at a substantially lower temperature. Secondly, effect of polyvinylpyrrolidone (PVP) as a chemical additive to suppress the loss of alkali ions is investigated. The results of the addition reveals that chemical interaction exists between PVP and the starting alkali

carbonates in their uncalcined state which subsequently reduces the volatilization of potassium and sodium during calcination. The in-situ heat generated by decomposition of PVP might also promote decomposition of the carbonates and promote the perovskite phase formation.

In addition, two additional lead-free compositions are explored. One is $Ba_{0.85}Ca_{0.15}Zr_{0.1}Ti_{0.9}O_3$ (BCZT) doped with LiF and synthesized with ultrasonic irradiation assistance. In this ceramic, the LiF dopant lowers the polymorphic phase transition (PPT) temperature and enhances the electrical properties at room temperature. Second is another novel KNN-LN based ceramic with BCZT as the dopant which was prepared with ultrasonic irradiation. A new compositional morphotropic phase boundary (MPB) was discovered with improved piezoelectric properties.

List of Publications

Journal Publications

1. **Tan**, **C. K. I.,** Yao, K., & Ma, J. (2011). Effects of ultrasonic irradiation on the structural and electrical properties of lead-free $0.94(K_{0.5}Na_{0.5})NbO_3–0.06LiNbO_3$ ceramics. *Journal of the American Ceramic Society*, 94, 776-781 .
2. **Tan, C. K. I.,** Yao, K., Goh, P. C., & Ma, J. (2012). $0.94(K_{0.5}Na_{0.5})NbO_3–0.06LiNbO_3$ piezoelectric ceramics prepared from solid state reaction modified with polyvinylpyrrolidone (PVP) of different molecular weights. *Ceramics International*, 38, 2513-2519.
3. **Tan**, **C. K. I.,** Yao, K., & Ma, J. (2013). Effects of LiF on the structural and properties of $Ba_{0.85}Ca_{0.15}Zr_{0.1}Ti_{0.9}O_3$ lead-free piezoelectric ceramics. *International Journal of Applied Ceramic Technology*, 10,701-706.
4. **Tan**, **C. K. I.,** Shannigrahi, S., Yao, K., & Ma, J. (2013). Structure, dielectric and piezoelectric properties $(1-x)K_{0.48}Na_{0.48}Li_{0.04}NbO_3$-$xBa_{0.85}Ca_{0.15}Ti_{0.9}Zr_{0.1}O_3$ ceramics. *Journal of Electroceramics*, (*Under review*).
5. **Tan, C. K. I.,** Jiang, Y., Tan, D. C. C., Yao, K., & Sritharan, T. (2013). Reaction kinetics for lead-free $0.94(K_{0.5}Na_{0.5})NbO_3$-$0.06LiNbO_3$ ceramic synthesis with ultrasonic irradiation. *International Journal of Applied Ceramic Technology,* (*Accepted*).

Conference Presentations

1. **Tan**, **C. K. I.,** Yao, K., & Ma, J. (2009). Preparation and properties of lead-free $0.94(K_{0.5}Na_{0.5})NbO_3$-$0.06LiNbO_3$ piezoelectric ceramics with excess alkali elements. *International Conference on Materials for Advanced Technologies (ICMAT 2009)*, Singapore. [Poster Presentation]
2. **Tan**, **C. K. I.,** Yao, K., & Ma, J. (2011). Effects of ultrasonic irradiation on the structural and electrical properties of lead-free $0.94(K_{0.5}Na_{0.5})NbO_3$–$0.06LiNbO_3$ ceramics. *Molecular Materials Meeting (M3 @ Singapore 2011)*. [Poster Presentation]
3. **Tan, C. K. I.,** Yao, K., Goh, P. C., & Ma, J. (2012). $0.94(K_{0.5}Na_{0.5})NbO_3$–$0.06LiNbO_3$ piezoelectric ceramics prepared from solid state reaction modified with polyvinylpyrrolidone (PVP) of different molecular weights. *Molecular Materials Meeting (M3 @ Singapore 2012)*. [Poster Presentation]
4. **Tan, C. K. I.,** Yao, K., & Ma, J. (2012). Synthesis and characterization of $K_{0.5}Na_{0.5}NbO_3$ based advanced ceramics. *3rd Trilateral Conference on Advances in Nanomaterials (MRS India @ IIT Bombay 2012)*. Invited speaker [Oral Presentation]
5. **Tan, C. K. I.,** Yao, K., & Ma, J. (2013). Effects of LiF on the structure and properties of $Ba_{0.85}Ca_{0.15}Zr_{0.1}Ti_{0.9}O_3$ lead-free piezoelectric ceramics. *Molecular Materials Meeting (M3 @ Singapore 2013)*. [Oral Presentation]

Patent Applications

1. Yao, K., Tan, C. Y., Zhang, L., **Tan, C. K. I.**, & Wong, T. C. (2012). A self-powered remote control device. Singapore 201203340-3.

List of Figures

List of Tables

List of Abbreviations

Chemical Reagents

PVP	Poly(vinylpyrrolidone)
K_2CO_3	Potassium carbonate
Na_2CO_3	Sodium carbonate
Li_2CO_3	Lithium carbonate
Nb_2O_5	Niobium oxide
$BaCO_3$	Barium carbonate
TiO_2	Titanium dioxide
$CaCO_3$	Calcium carbonate
ZrO_2	Zirconium oxide
LiF	Lithium fluoride
PVB	Polyvinyl butyral
PVA	Polyvinyl alcohol

Material Compositions

PZT	Lead zirconate titanate, $Pb(Zr_xTi_{1-x})O_3$
PZN-PT	Lead zinc niobate-lead titanate, $Pb(Zn_{1/3}Nb_{2/3})O_3$-$PbTiO_3$
PMN-PT	Lead magnesium niobate-lead titanate, $Pb(Mg_{1/3}Nb_{2/3}O_3)$-$PbTiO_3$
BTO	Barium titanate, $BaTiO_3$
BNT	Bismuth sodium titanate, $(Bi_{0.5}Na_{0.5})TiO_3$
KNN	Potassium sodium niobate, $(K_{0.5}Na_{0.5})NbO_3$
LN	Lithium niobate, $LiNbO_3$
BZT	Barium zirconate titanate, $Ba(Zr_{0.2}Ti_{0.8})O_3$
BCT	Barium calcium titanate, $(Ba_{0.7}Ca_{0.3})TiO_3$
BIT	Bismuth titanate, $Bi_4Ti_3O_{12}$
KLN	Potassium lithium niobate, $K_3Li_2Nb_5O_{15}$
KSN	Potassium strontium niobate, $KSr_2Nb_5O_{15}$

PEG	Poly(ethylene glycol)	KBT	Potssium bismuth titanate, $(K_{0.5}Bi_{0.5})TiO_3$
EDTA	Ethylenediaminetetraacetic acid	KN	Potassium niobate, $KNbO_3$
DEA	Diethanolamine	NN	Sodium niobate, $NaNbO_3$
ZnO	Zinc oxide	KCN	Potassium copper niobate, $K_4CuNb_8O_{23}$
CuO	Copper oxide	KCT	Potassium copper tantalate, $K_{5.4}Cu_{1.3}Ta_{10}O_{29}$
MnO_2	Manganese oxide	BF	Bismuth ferrite, $BiFeO_3$
		BST	Barium tin titanate, $Ba(Sn_{0.12}Ti_{0.88})O_3$
		BCZT	Barium calcium zirconate titanate, $(Ba_{0.85}Ca_{0.15})(Zr_{0.1}Ti_{0.9})O_3$

Characterization Techniques

SEM	Scanning Electron Microscopy
FTIR	Fourier Transform Infrared Spectroscopy
XPS	X-Ray Photoelectron Spectroscopy
TGA	Thermogravimetry Analysis
DSC	Differential Scanning Calorimetry
XRD	X-Ray Diffraction

Processing Techniques

SPS	Spark plasma sintering
HP	Hot pressing
CSD	Chemical solution deposition
PC	Polymerized complex method

Chapter 1

Introduction

1.1 Background

Most commonly used piezoelectric devices available in the market are made from lead-based piezoelectric materials. [1, 2] Their compositions include $Pb(Zr_xTi_{1-x})O_3$ (PZT), $Pb(Zn_{1/3}Nb_{2/3})O_3$-$PbTiO_3$ (PZN-PT) and $Pb(Mg_{1/3}Nb_{2/3})O_3$-$PbTiO_3$ (PMN-PT) which exhibit high electromechanical properties within the morphotropic phase boundary (MPB) region. [3, 4] A typical PZT material phase diagram is illustrated in Fig. 1.1 to indicate the MPB region between the rhombohedral and tetragonal phases.

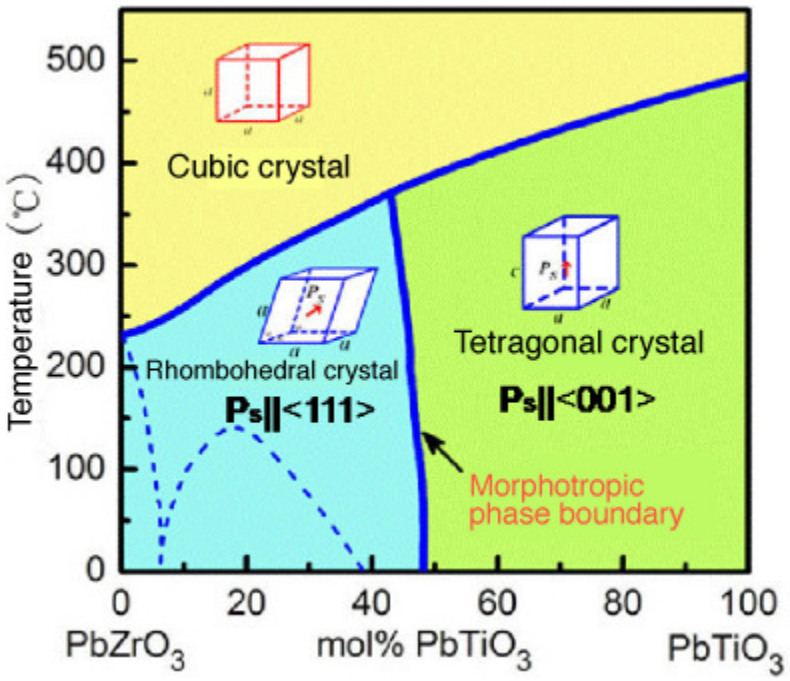

Fig. 1.1. A typical PZT material phase diagram. [5]

However, these lead-based piezoelectric materials, despite their excellent electromechanical performances, contain more than 60 % lead by weight. Because of the high toxicity of lead, these materials are detrimental to human health and environment. [6] Lead gradually builds up in human's body and causes serious medical problems as shown in Fig. 1.2. Especially, young children are more vulnerable to lead, as it can affect their growth.

Fig. 1.2. Some common effects of lead poisoning. [7]

The European legislations have banned certain hazardous substances of being used for electronic appliances. This legislation essentially applies to gradual removal of lead based devices. [8] Other countries around the world have also established similar activities and regulations. [9] Since the most commercially available sensors, actuators and other electronic devices are based on lead zirconates and lead titanates, [10, 11] it is important to look for substitutes to replace the current lead-based piezoelectric materials, especially with those having comparable properties.

There are many different types of lead free piezoelectric ceramics, such as tungsten bronze structure ferroelectrics (TBSFs), [12-14] bismuth layer structure ferroelectrics (BLSFs), [15-19] improved $BaTiO_3$ (BTO), [20-26] ($Bi_{0.5}Na_{0.5}TiO_3$) (BNT) [27-33] and $K_{0.5}Na_{0.5}NbO_3$ (KNN) [34-40] ceramics. There has been a growing interest on modified KNN based ceramics after the report by Saito and his colleagues on 2004. This team at Toyota Central Research Laboratory found a lead-free piezoelectric material based on KNN doped with Li, Sb, Ta elements having piezoelectric properties comparable with PZT families at room temperature (Fig. 1.3). [41]

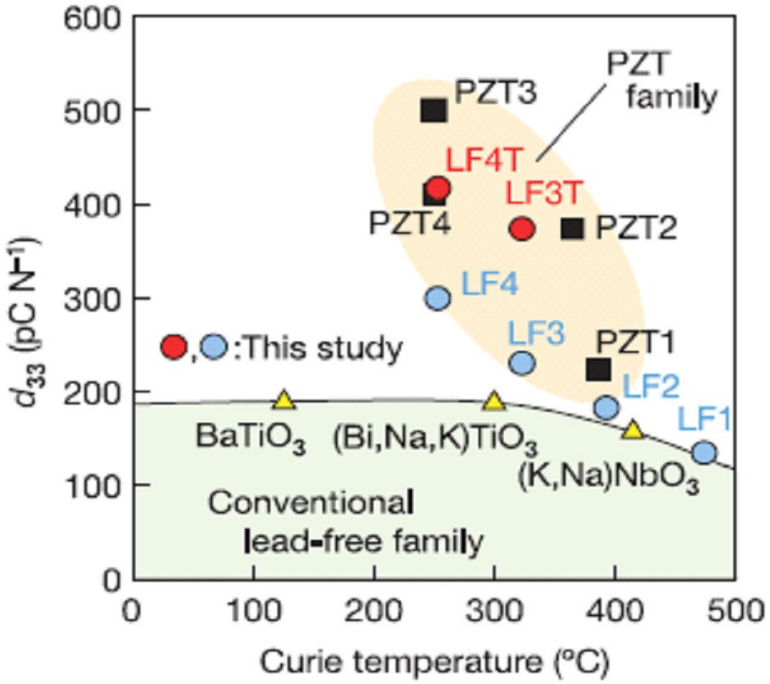

Fig. 1.3. Comparison of the piezoelectric properties d_{33} at 25 °C among the developed LF ceramics and commercial available PZT. The chemical composition for LF4 is $(K_{0.44}Na_{0.52}Li_{0.04})Nb_{0.86}Ta_{0.10}Sb_{0.04})O_3$. [41]

Since then, the KNN based ceramics have attracted great interest of scientists all over the world. [42-71] Although the LF4 piezoelectric ceramics exhibit promising piezoelectric

properties, their Curie temperature is merely about 253 ^{o}C. Furthermore the preparation process of LF4T is complex and not cost effective for mass production. In the same year, another group by Guo and Kakimoto *et al.* investigated the (1-x)($K_{0.5}Na_{0.5}$)NbO_3-x($LiNbO_3$) (KNN-LN), an alkali niobate based solid solution, and reported a MPB region in the proximity of 5-7 mol% $LiNbO_3$ and possessing excellent piezoelectric properties, d_{33} of 200 - 235 pC/N, and very high Curie temperature T_c of 450 - 510 ^{o}C, as displayed in Fig. 1.4 and Fig. 1.5, respectively. [72]

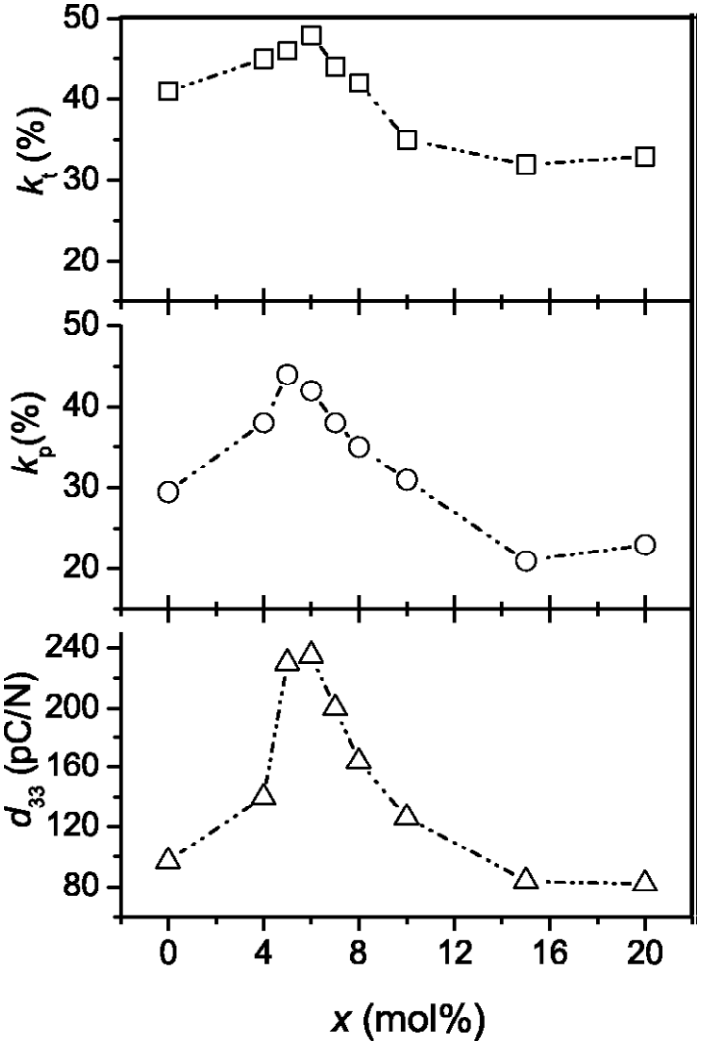

Fig. 1.4. Electrical properties of (1-x)KNN-xLN ceramics as a function of the $LiNbO_3$ content. [72]

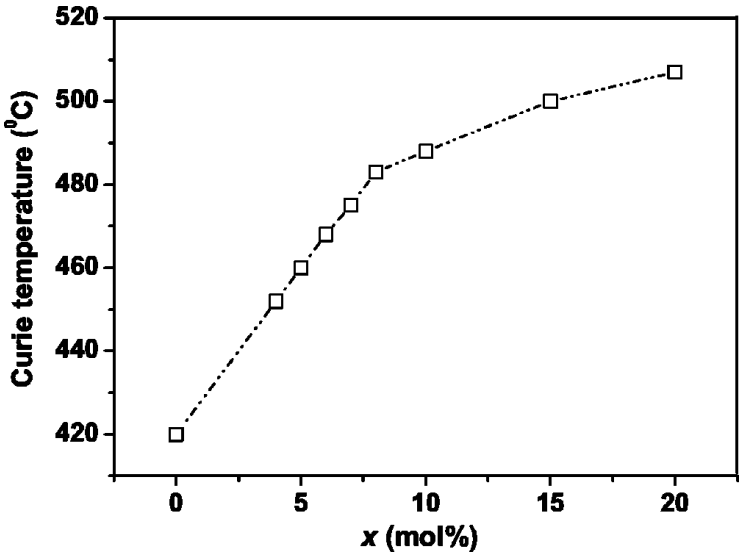

Fig. 1.5. Concentration dependence of the Curie temperature (T_c) for (1-x)KNN-xLN ceramics. [72]

However, the raw carbonate powders are very moisture sensitive and often result in hygroscopic secondary phases in the samples. Such samples will easily disintegrate upon contact with air. In addition, it is well known that the raw carbonate powders, like K_2CO_3, Na_2CO_3 and Li_2CO_3, have low melting point ranging from 700-900 ^oC. Upon heating process, the alkali oxides can become moderately volatile and make it difficult to achieve chemical stoichiometry. Therefore it is important to find an effective way to modify the starting materials and control the alkali volatility issue. However, there are limited studies on effective control of the serious alkali metal ions volatility issue. In addition, most bulk ceramic processing procedures involve long hours of ball milling, which is not cost effective, and can potentially introduce considerable contaminations during the mechanical milling process.

In a more recent work Liu *et al.* [73] discovered an extremely high piezoelectric coefficient of d_{33} = 300-600 pC/N in well optimized $Ba(Zr_{0.2}Ti_{0.8})O_3$-$(Ba_{0.7}Ca_{0.3})TiO_3$,

abbreviated as BZT-BCT. The MPB design in this compound starts from a triple point, as shown in Fig. 1.6 (a), which has a very low energy barrier for polarization rotation and lattice distortion.

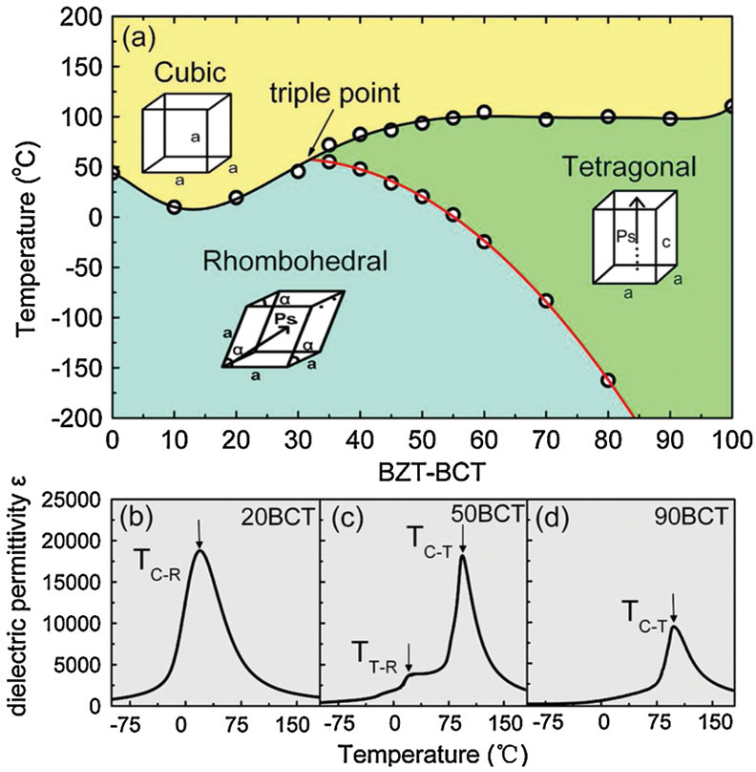

Fig. 1.6. (a) Phase diagram of pseudo-binary ferroelectric system $Ba(Zr_{0.2}Ti_{0.8})O_3$-$(Ba_{0.7}Ca_{0.3})TiO_3$, abbreviated as BZT-BCT. (b) - (d) Dielectric permittivity curves for 20BCT, 50BCT, and 90BCT, respectively. [73]

However, the low Curie temperature T_c of 93 ^oC at MPB with 50BCT content as shown in Fig. 1.6 (c) hindered many practical applications in higher temperature region. Moreover, to obtain the stoichiometric composition of $Ba_{0.85}Ca_{0.15}Zr_{0.1}Ti_{0.9}O_3$ (BCZT) piezoelectric ceramics, it is required to synthesize the individual powders of perovskite BZT and BCT before mixing them with 1:1 molar ratio. Hence the preparation involves multiple processing

steps and long processing time, which is not cost effective for mass production. Therefore, it is necessary to find an alternative way to synthesize this promising material with excellent piezoelectric properties and improved T_c value in a more effective route.

1.2 Research objectives

The objectives of this thesis are to explore various channels to achieve cost effective and promising lead-free piezoelectric ceramics with high piezoelectric performances. Of the existing lead-free materials, KNN-LN and BCZT systems are the most promising ceramic materials, and are chosen to be investigated in this thesis. The objectives are further elaborated as follows:

a) To understand the relationship among the composition, processing, structure and property in lead-free KNN-LN and BCZT ceramic systems, including exploring a new, fast and cost effective ceramic processing route to synthesize lead-free piezoelectric compositions with relatively high density and without any special powder treatment like cold isostatic pressing (CIP).

b) To explore an effective solution to address the alkali volatility issue in lead-free KNN-LN piezoelectric ceramics.

c) To engineer new compositions of lead-free piezoelectric ceramic by modifying BCZT and KNN-LN systems and exploring new MPB phase boundaries.

1.3 Scientific approaches

- To apply ultrasonic irradiation method for preparation of lead-free piezoelectric ceramics with significantly reduced processing time and tailored the reaction kinetics.
- To use polyvinylpyrrolidone (PVP) polymer as an additive to stabilize the metal ions through possible interaction between the metal ions and the oxygen or nitrogen atoms on the five membered nitrogen containing heterocycles of PVP. This interaction may mitigate the serious alkali volatility problem in KNN-based system.
- To modify the BCZT with chemical doping (LiF) and to explore new phase boundary between KNN-LN and BCZT with improved piezoelectric properties and T_c.

1.4 Organization of the thesis

- Chapter 2 first gives an overview of ferroelectric and piezoelectric materials, emphasizing perovskite structure based on $(K_{0.5}Na_{0.5})NbO_3$ (KNN) and $BaTiO_3$ (BTO) lead-free ceramic systems. The fundamental principles of several ceramic processing routes, such as conventional ball milling, hot pressing, spark plasma sintering, ultrasonic irradiation and polymer assisted ceramic processing are explained. Literature reviews on studies of KNN and BTO ceramics with enhanced electrical properties are conducted. Further review is given on the effect of chemical dopants in KNN and BTO lead-free ceramics on their MPB and Polymorphic Phase Transition (PPT).
- Chapter 3 is about characterization techniques used to test and analyze the electrical performance of the lead-free piezoelectric ceramics.

- Chapter 4 studies the MPB composition of lead-free 0.94KNN-0.06LN piezoelectric ceramics prepared by ultrasonic irradiation method. It also explores the effect of ultrasonic irradiation on the phase changes, reaction kinetics, microstructure and electrical properties of the KNN-LN ceramics.
- Chapter 5 explores role of polyvinylpyrrolidone's (PVP) as chemical additive in suppressing alkali volatility in lead-free 0.94KNN-0.06LN piezoelectric ceramics prepared by solid state reaction. The reaction mechanism in PVP doped lead-free KNN-LN piezoelectric ceramics are discussed and piezoelectric properties are measured. Effects of PVP polymer additive with different molecular weights are studied from which optimum molecular weight with the lowest alkali loss and highest piezoelectric coefficient is determined.
- Chapter 6 examines the effect of LiF doping in lead-free BCZT ceramics. The polymorphic phase transition temperature of rhombohedral-tetragonal phase is found to shift nearer to room temperature with Li doping and resulting in an improved piezoelectric coefficient of d_{33} = 380 pC/N. Systematic study of the LiF doping effect on lead-free BCZT electrical properties are investigated.
- Chapter 7 examines the effect of $Ba_{0.85}Ca_{0.15}Zr_{0.1}Ti_{0.9}O_3$ (BCZT) doping in orthorhombic phase of $0.96(K_{0.5}Na_{0.5})NbO_3$-$0.04LiNbO_3$ (KNN-LN) lead-free ceramics. It is found that BCZT dopants improves the ceramic density and creates a MPB region leading to improved piezoelectric properties d_{33} from 100 to 180 pC/N. The phase structure, temperature dependent dielectric and ferroelectric properties are studied in details.
- Chapter 8 summarizes the conclusions for this thesis and suggested future work.

Chapter 2:

Literature Review

2.1 Introduction of ferroelectric materials

Ferroelectric materials have a spontaneous electric polarization that can be reoriented between two or more states by applying an external electric field. [74] Without any external electric field condition, crystal structure of ferroelectric is non-centrosymmetric based on the configuration of the cations and anions within the unit cell. [1] From crystallographic perspectives, all crystals can be categorized into 32 symmetry point groups. These 32 symmetry point groups can be further distinguished into two classes: 21 point groups which are non-centrosymmetric and 11 groups are centrosymmetric. Piezoelectric materials belong to the non-centrosymmetric point groups, except for the (432) point group. [3] Within the 20 non-centrosymmetric point groups, only 10 point groups possess pyroelectricity and their spontaneous polarization changes with temperature. A simple diagram to illustrate the classes of ferroelectric materials on the basis of crystal symmetry is shown in Fig. 2.1. A ferroelectric material is responsive to temperature. This is related to the ions within the material's crystal lattice that are usually configured in an arrangement that minimizes the energy system internally. Therefore, temperature variations of the materials system will change the crystal symmetry and affect its ferroelectric behaviour.

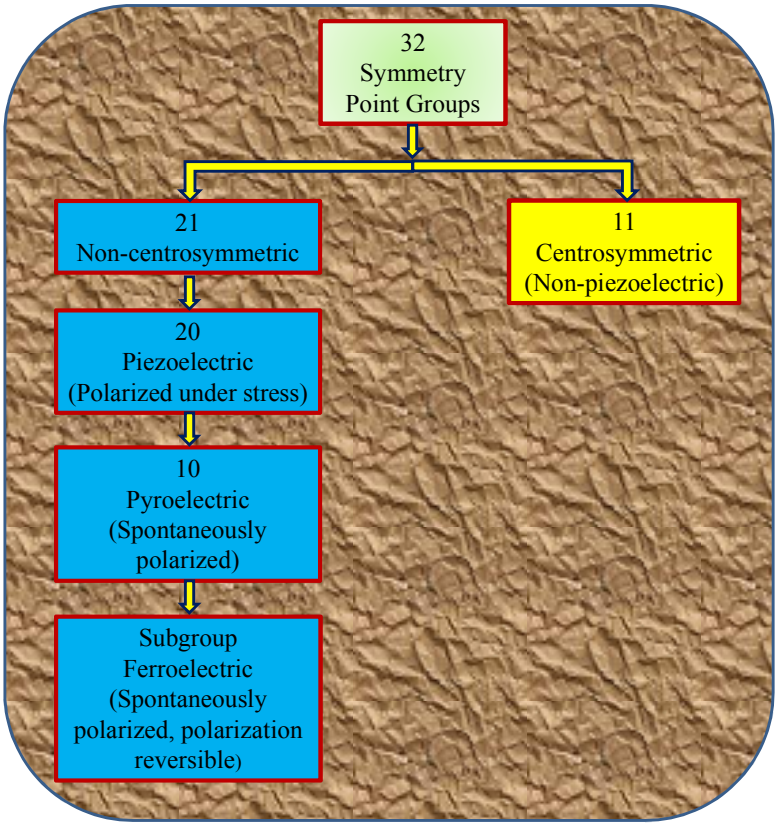

Fig. 2.1. Classes of ferroelectric materials on the basis of crystal symmetry. [75]

Figure 2.2 shows the schematic drawing of unit cell of a perovskite ABO_3 structure of PZT material where A-site is the cation comprising of Pb^{2+} that occupies the eight corners, and B-site is the cation comprising of Ti^{4+} and Zr^{4+} that position at the centre, while O is the oxygen anion situated at the six faces of the unit cell making a octahedral cage with B-site cation within the center of the octahedral cage.

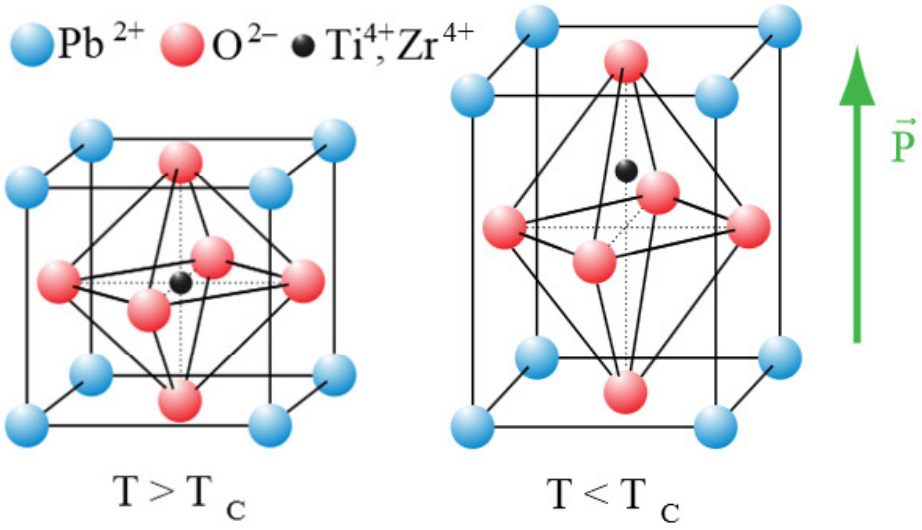

Fig. 2.2. Schematic drawing of the perovskite ABO_3 structure of PZT.

As can be seen from Fig. 2.2 when $T > T_c$, PZT exhibits cubic crystal symmetry where the centers of both positive (+) and negative (-) charges coincide at equilibrium state and thus there is no net spontaneous polarization. On the other hand, when temperature $T < T_c$, ferroelectric PZT material exhibits non-centrosymmetric structure which results in a spontaneous polarization in the materials. When an electric field is applied, the B site cations can be directionally polarized. A net polarization induced by applying electric field to distort the unit cell aligns in the same direction. Furthermore, the polarization can be switched, simply by applying electric field in the opposite direction. Therefore, it is possible to polarize the structure between two states by switching the applied external electric field. This is due to the existence of multiple equivalent thermodynamic states as illustrated on a potential energy diagram as shown in Fig. 2.3. However, an energy barrier has to be overcome in order to switch the polarization.

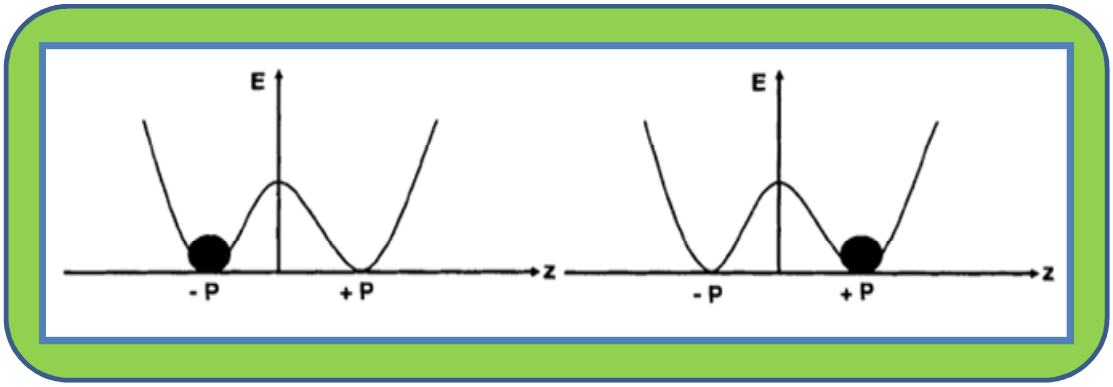

Fig. 2.3 Schematic diagram to illustrate the potential energy diagram for two polarization states. [76]

The polarization switching phenomenon can be described with Fig. 2.4. By increasing the electric field strength (from zero), dipole moments within domain start to align in the positive direction that gives rise to maximum polarization in the unit cell by a maximum B-site displacement (Point A). By drawing a tangential line from Point A to intercept the polarization axis, the spontaneous polarization (P_s) can be determined. However, when the external field is removed, the polarization does not fall to zero because some domains still maintain the orientation and thus the remnant polarization (P_r) (Point B) is retained. The polarization cannot be completely reversed unless an adequately high electric field is applied to overcome the energy barrier and cause domain switching. This external field is defined as the coercive electric field (E_c) (Point C). With strength of the reverse field increased, maximum polarization is reached in the opposite direction (Point D). After that, when the electric field is reversed back to zero (Point E), polarization reaches $-P_r$, and then the polarization can be brought back to zero by application of the positive coercive electric field, ($+E_c$) (Point F). Finally, a complete ferroelectric hysteresis loop is obtained.

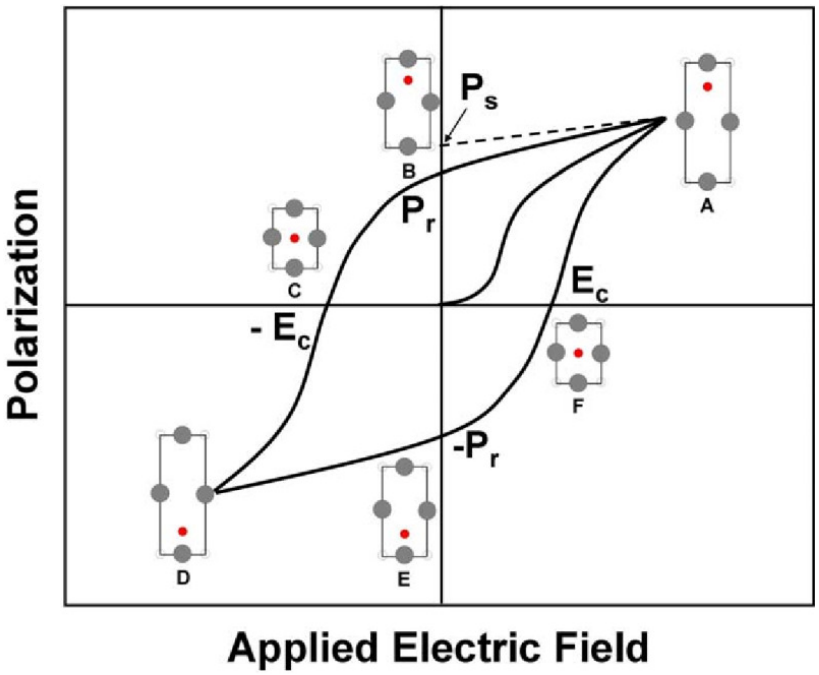

Fig. 2.4 Typical hysteresis loop of ferroelectric materials with schematic diagram of crystal lattice cell. [61]

2.2 Introduction of piezoelectric materials

The discovery of piezoelectricity was discovered by Pierre and Jacques Curie in the year 1880. [77] As mentioned previously in Fig. 2.1, piezoelectric materials belong to the non-centrosymmetric point groups. These non-centrosymmetric piezoelectric materials exhibit an electrical polarization directly proportional to an applied mechanical stress (compressive or tensile). This is called the direct piezoelectric effect. [4] The direct piezoelectric effect is referred to the electric charge generation when the material is deformed. When the piezoelectric material is exposed to an electric field, the unit cell expands or contracts linearly. This is known as the converse piezoelectric effect. Fig. 2.5

illustrates both direct and converse effects in a piezoelectric ceramic. Many electronic devices utilize both direct and converse effects for industrial applications.

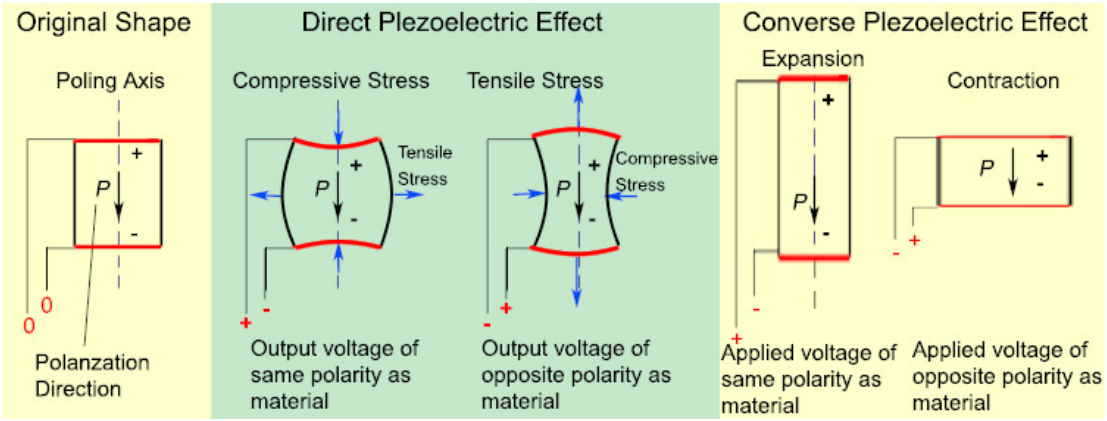

Fig. 2.5. Direct and converse piezoelectric effects in a piezoelectric ceramic. [31]

In polycrystalline ferroelectric-based piezoelectric materials, polar domains are usually randomly oriented after sintering. As a result, zero net polarization is obtained in the material as illustrated in Fig. 2.6 (a). However, the material can be switched into polarized state by applying a high direct current (DC) electric field, normally 2-3 times of the coercive electric field E_c. This process is often called poling as shown in Fig. 2.6 (b). Upon removal of the electric field, most of the polar domains are almost aligned close to the applied electric field and locked into a remnant polarization configuration, as shown in Fig. 2.6 (c). The piezoelectric material is now poled with net polarization and exhibits piezoelectric properties.

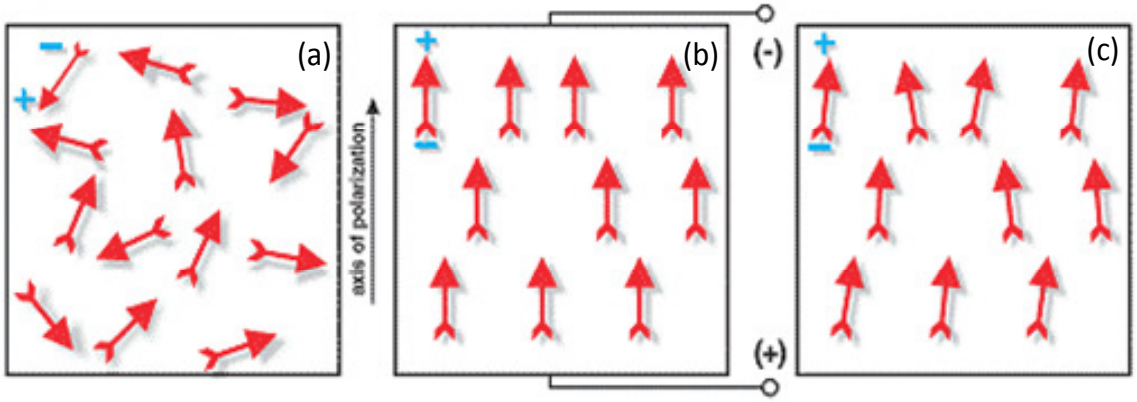

Fig. 2.6. Polarizing of a piezoelectric ceramic, (a) random orientation of polar domains prior to poling, (b) poling in DC electric field, (c) remnant polarization after electric field is removed. [71]

2.3 Ceramic processing methods

In this section, the preparation of lead-free piezoelectric ceramics using conventional solid state reaction routes including ball milling process will be discussed and explained. In addition, other modified processing routes like using spark plasma sintering and hot-pressing which are very effective to achieve high ceramic density in lead free piezoelectric ceramics will also be described. However, it should be noted that both of the two techniques are very expensive and not suitable for mass production applications. Furthermore, the cost effective, fast and clean ultrasonic irradiation processing method and the polymer modified ceramic processing method will be discussed.

2.3.1 Conventional solid state reaction route

As reported in the literature, most of the preparation methods of lead-free piezoelectric ceramics utilize carbonate and oxide powders via mechanical mixing and

conventional solid state reaction route. [72] Fig. 2.7 gives a schematic diagram to illustrate the typical solid state ceramic processing flow.

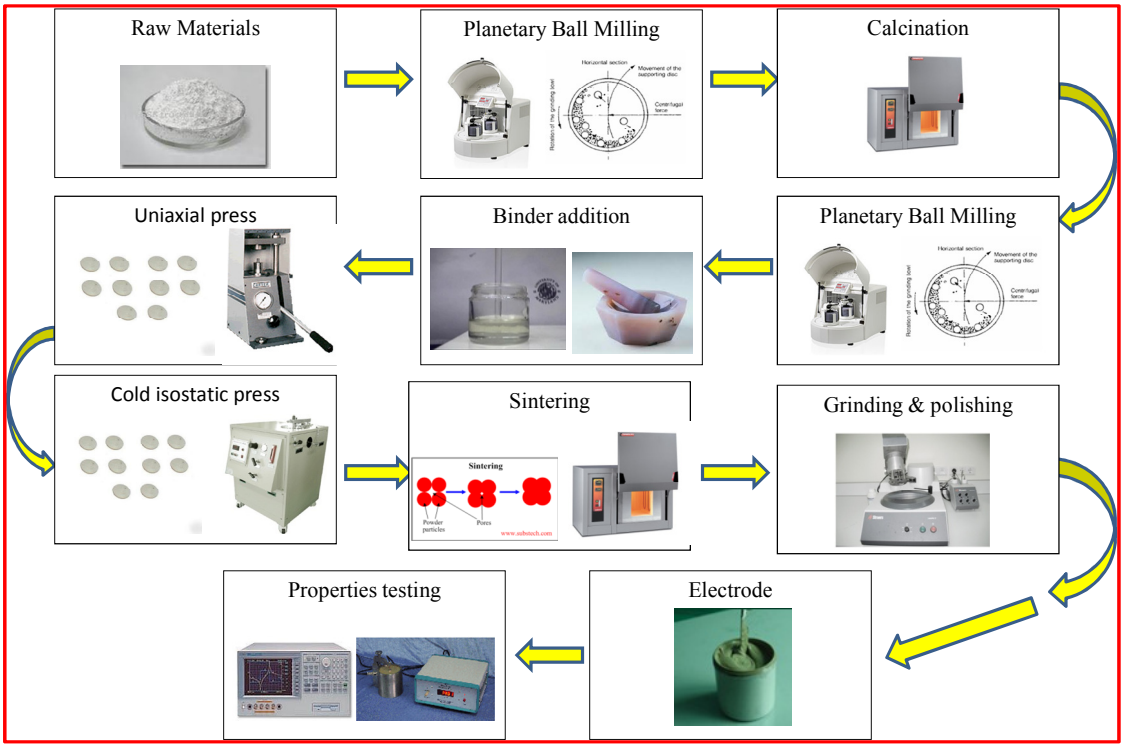

Fig. 2.7. A typical solid state ceramic processing scheme.

Firstly, starting materials are weighed according to the stoichiometric formula and placed into an agate jar with balls. Typically 24 h of ball milling in ethanol or water as medium is conducted to ensure homogenous mixing. After complete mixing, the slurry is dried in a convention oven. The dried powder is placed into alumina crucible and then calcined in a high temperature furnace. The calcined powders are further ball milled again for another 24 h to break down the hard powder agglomerates. The slurry is dried again in the oven and the dried powder is ground and mixed with binder, typically polyvinyl butyral (PVB) or polyvinyl alcohol (PVA), so that the mixture can be uniformly pressed into circular ceramic disks without any cracking. In order to achieve high ceramic density, the pellets can be

further pressed using cold isostatic press machine prior to final sintering process at high temperature. The sintered pellets are polished using silicon carbide paper by lapping machine prior to silver electroding. Lastly, the ceramic disk samples are ready for poling and electrical properties testing, such as dielectric, ferroelectric and piezoelectric testing.

2.3.2 Modified solid state reaction route

The conventional solid state reaction route as described above is commonly used by most ceramists. However, there are still sinterability problems encountered in many lead-free piezoelectric materials to achieve high ceramic density. In order to resolve this problem, some researchers introduced spark plasma sintering (SPS) as a sintering technique to improve ceramic density for many types of lead-free materials. [40, 78-89]

The main features of SPS uses the pulsed DC current passes through the powder graphite die directly and the heat is generated internally. This allows a very rapid heating or cooling rate up to 1000 ^{o}C/min. Therefore, the sintering process time can be within a few minutes. This fast sintering process has great potential to produce dense ceramic samples with nano grains or nanostructure while avoiding grain coarsening. Fig. 2.8 gives a schematic diagram to illustrate the SPS process. [90]

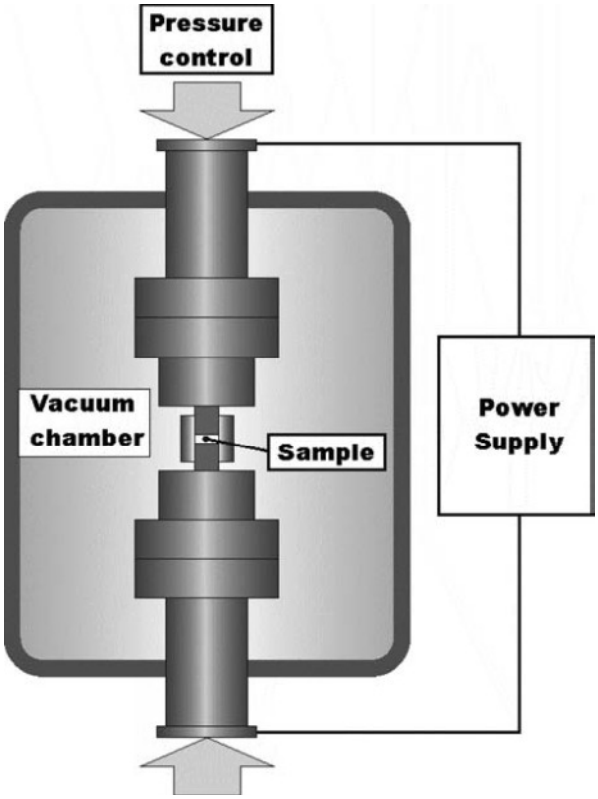

Fig. 2.8. Schematic illustration of spark plasma sintering process. [90]

Hot pressing (HP) is another technique reported in literature to achieve high density ceramics in lead-free materials. [13, 35, 91-99] This technique is a process of applying simultaneous external pressure and temperature to densify ceramics. It is performed by placing ceramic powder into a graphite die set, and applying uniaxial pressure while the whole system is held at an increasing temperature. However, as mentioned earlier both SPS and HP techniques of achieving high density ceramics are not cost effective and not suitable for mass production.

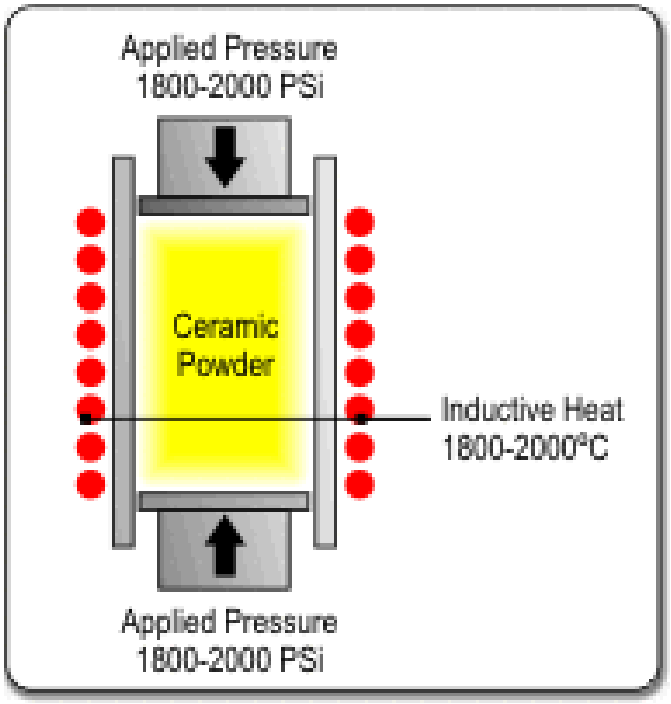

Fig. 2.9. Schematic illustration of hot pressing process. [100]

2.3.3 Ultrasonic irradiation assisted route

In 1963, Webster reported that cavitation in liquid results in a few effects, like erosion, emulsification, and the initiation of chemical reactions. However during that time, the cause of the effects was not well understood. [101] Later on, Suslick *et al.* did extensive research to understand the effect of ultrasonic irradiation and reported that collapse of ultrasound induced cavitation bubbles upon could lead to local temperature of ~ 5000 K and pressures of ~ 1000 bar. [102] This can lead to several effects on the surface morphology and characteristics of inorganic solids and also increase their surface area significantly. [103-110] Fig. 2.10 schematically illustrates a typical ultrasonic probe apparatus.

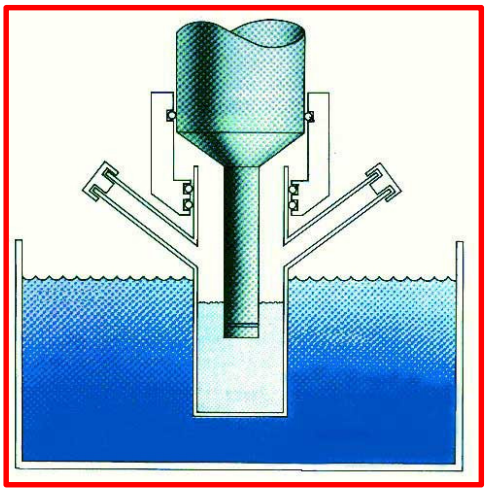

Fig. 2.10. Schematic illustration of a typical ultrasonic probe apparatus. [111]

Barantchikov *et al.* found that ultrasonic treatment significantly affects the kinetic and reaction mechanism of the solid-phase synthesis of ferrite materials and reported that ultrasound may induce more extended reaction zones at the initial stage of reaction and enhance the material's reactivity. [112-114] Prozorov *et al.* discovered that the collapse of cavitation bubble generates intense shock waves that propagate in the liquid at high velocity and create high collisions rate among solid particles. Upon the point of impact, the solid particles collision leads to extreme heating, which generates effective localized melting. [115] Ultrasonic irradiation has also been used to synthesize piezoelectric materials. Xu *et al.* reported synthesize of nearly mono-sized spherical $BaTiO_3$ powders, with different sizes ranging from micro- to nano-meter, by adjusting the solution concentration. [116] More recently, Dang *et al.* discovered a new effect using ultrasonic irradiation to synthesize nano-sized $BaTiO_3$ particles. The original particles, treated with ultrasonic irradiation, were identified to aggregate in common crystal axis and form larger particles; the aggregated particles had a single crystal structure. [21] Till now, there are very limited reports on

preparation of major lead-free piezoelectric materials (such as KNN system) by ultrasonic irradiation method.

2.3.4 Polymer assisted route

In the last decade, polymers have been introduced into the chemical precursor solutions in the chemical solution deposition (CSD) process to solve the film cracking problem when a single-cycle coating exceeds a critical film thickness. [117, 118] In addition, it is noted that introducing polymer as additives allows the ability to modify and change the electrical and mechanical properties, [119] and improve the quality of the epitaxial metal-oxide growth films. [120] Yao and his groups also investigated the significant effect of polymer on ceramic processing, particularly in $Pb(Zn_{1/3}Nb_{2/3})O_3$ (PZN)-based ferroelectric thin films prepared through a chemical solution approach. [7, 121-123] They found that the addition of polymer in the solution dramatically promoted the perovskite phase while suppressing the pyrochlore phase.

It is commonly known that obtaining single phase perovskite structure in $Pb(Zn_{1/3}Nb_{2/3})O_3$−$PbTiO_3$ (PZN-PT) relaxor ferroelectrics is difficult due to formation of pyrochlore phases during their synthesis process. In order to achieve pure perovskite phase, Swartz and Shrout [124] developed a two-stage calcination technique named as the columbite method. Recently, Yu *et al.* have used the polymer assisting process to synthesize solid state $Pb(Mg_{1/3}Nb_{2/3})O_3$−$PbTiO_3$ ceramics without the use of columbite method. [125, 126] They found that poly(ethylene glycol) (PEG) polymer interacts with lead oxide, and suppresses the formation of the Pb-deficient pyrochlore phase and promotes the perovskite formation.

The lead-free KNN films produced by CSD method typically have large leakage currents, and it is very difficult to obtain well-saturated polarization hysteresis loops. [127]

Wang *et al.* has made KNN films prepared from polyvinylpyrrolidone (PVP)-modified chemical solution. They found that PVP has the ability to maintain chemical stoichiometry by preventing the loss of alkali ions during annealing and obtained a large effective piezoelectric coefficient d_{33}, of 61 pm/V and a well-saturated polarization hysteresis loop. [5, 128-131] In a more recent work, Goh *et al.* have introduced ethylenediaminetetraacetic acid (EDTA) and diethanolamine (DEA) as stabilizing agents which help to bind the metal ions in KNN solution prior to annealing and keep the film homogenenity and chemical stoichiometry. By this approach, they were able to produce low leakage current films with outstanding large piezoelectric coefficients. [132, 133]

It is well known that the high volatility of potassium and sodium during heat treatment has made it challenging to achieve chemical stoichiometry and high density in KNN ceramics. The main solution currently is to add excess K and Na to achieve compositions close to the stoichiometric one and improve the ceramic performance property. [134] There are very limited studies on the use of polymers to suppress the alkali volatility problem in lead-free piezoelectric ceramics prepared by solid state reaction route.

2.4 Types of lead-free piezoelectric ceramics materials

In this section, several types of lead-free ceramic materials based on their crystal structures like bismuth layer structure, tungsten bronze structure and perovskite structure, will be discussed. The discussion is focused on perovskite structure especially $K_{0.5}Na_{0.5}NbO_3$ (KNN)-based and $BaTiO_3$ (BTO)-based ceramics. The use of proper chemical dopants and innovations on the processing techniques to improve the ceramic density and electrical properties will be addressed. In addition, the reported studies about creating a morphotropic phase boundary (MPB) in KNN-based and BTO-based ceramics and tailoring the

polymorphic phase transition (PPT) temperature to improve the dielectric, ferroelectric and piezoelectric properties will be introduced.

2.4.1 Bismuth layer structure

It is commonly known that $Bi_4Ti_3O_{12}$ (BIT) is a bismuth layer-structured ferroelectric material which exhibits low dielectric constant, high Curie temperatures (T_c) and high anisotropy in the electromechanical coupling factor in longitudinal and transverse directions. These characteristics make it suitable for high temperature pyroelectric sensor materials. [135-137] However, this material has problems such as large coercive field and low resistivity. [15, 16, 18, 19] It also contains heavy and volatile element of bismuth.

2.4.2 Tungsten bronze structure

$K_3Li_2Nb_5O_{15}$ (KLN) and $KSr_2Nb_5O_{15}$ (KSN) are typical ferroelectric materials with tetragonal tungsten bronze structure that gives strong photorefractive, piezoelectric and pyroelectric effects. [12, 138] However, their piezoelectric properties are typically inferior to perovskite structure due to the difficulty of domain switching by external electric field during poling. Therefore they are not competitive enough to replace the lead-based piezoceramics.

2.4.3 Perovskite structure

Barium titanate perovskite structure

$BaTiO_3$ (BTO) is a well-known lead-free ferroelectric perovskite structure. Historically, it was found earlier than PZT. It was the discovered by Wul and Goldman in the year 1945. [139] However, it's piezoelectric properties are not competitive to lead-based

systems and it has low Curie temperature, which has restricted its commercial applications as sensors and actuators.

Bismuth-based perovskite structure

Pure bismuth sodium titanate $(Bi_{0.5}Na_{0.5})TiO_3$ (BNT) ceramic can be recognized to be one of the ideal candidates for lead-free piezoelectric material because of its high remnant polarization (P_r = 38 μC/cm^2). [140, 141] However, it is quite difficult to pole BNT due to its large coercive field and high conductivity which lead to poor piezoelectric properties. For this purpose, many studies have been conducted to improve its piezoelectric properties by combining it with other ferroelectrics like $(K_{0.5}Bi_{0.5})TiO_3$ (KBT) [142] and $BaTiO_3$ to form solid solution. [143] It is important to take note that although bismuth is considered to be less toxic to humans as compared to other heavy metals like lead, however bismuth and its salts have been known to cause kidney damage. Large doses can be fatal. [33] Currently, there is no well-established information on bismuth toxicity. Therefore, whether the usage of bismuth is human and environment friendly, still remains questionable.

Alkali niobate-based perovskite structure

Ferroelectricity of $KNbO_3$ (KN) was first reported by Matthias in 1949 [144]. Its crystal structure is orthorhombic at room temperature. The phase transitions in KN are similar to $BaTiO_3$ (BTO) [145, 146] and follow the sequence of rhombohedral, orthorhombic, tetragonal and cubic upon increasing the temperature but the transition occurs at higher temperatures. Fig. 2.11 shows the dielectric constant versus temperature for $KNbO_3$ single crystal. [4] At the temperature below 0 ^oC, the first polymorphic phase transition is

rhombohedral to orthorhombic phase. The transition temperature can be -60 ^{o}C or -20 ^{o}C, depending on whether it is heating up or cooling down, respectively.

The second polymorphic phase transition happens at 220 ^{o}C (heating up) or 190 ^{o}C (cooling down) which corresponds to orthorhombic to tetragonal phase transformation. The last polymorphic phase transition which is also an indication of the Curie temperature of KN falls at temperature of 420 ^{o}C (heating up) or 400 ^{o}C (cooling down) which corresponds to ferroelectric tetragonal to paraelectric cubic phase transformation.

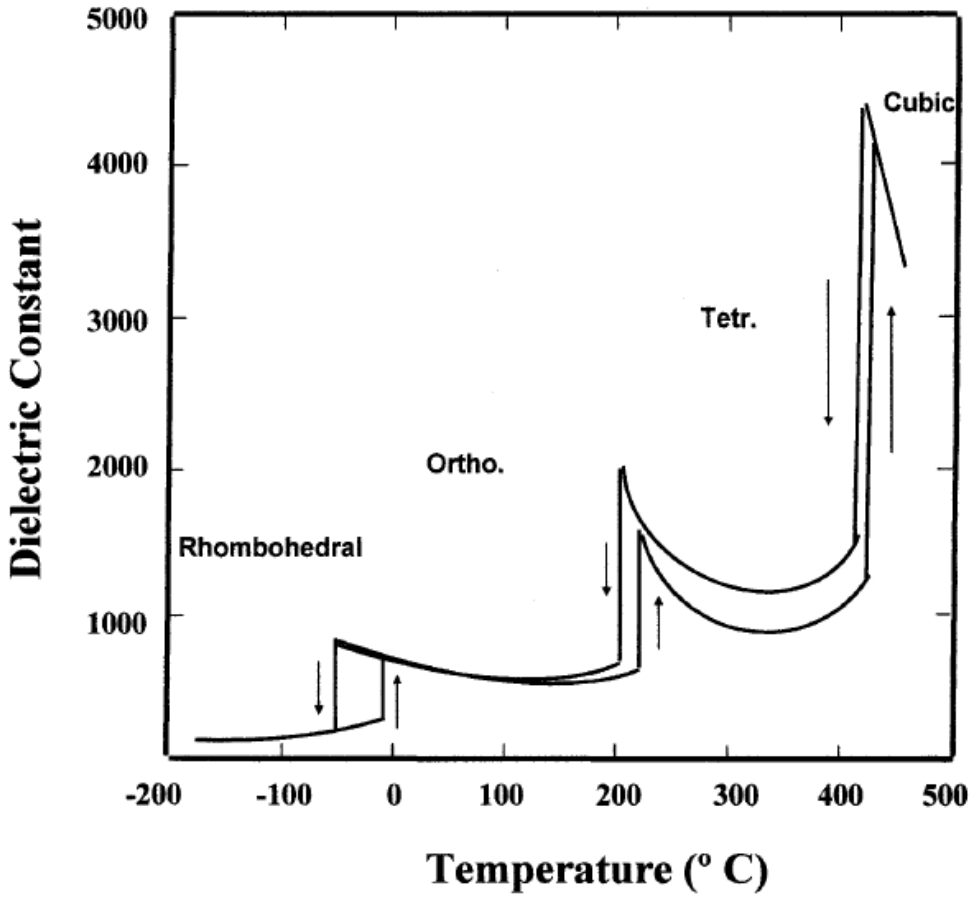

Fig. 2.11. Dielectric constant versus temperature curve of $KNbO_3$ single crystal. [4]

By the addition of $NaNbO_3$ (NN) into potassium niobate (KN) system, several polymorphic phase boundaries can form as seen in the phase diagram of $KNbO_3$-$NaNbO_3$

system in Fig. 2.12. [4] It is reported by Egerton [147] that at the vicinity of 50:50 ratio of K^+:Na^+, high radial coupling coefficients are observed. In this composition, the piezoelectric coefficient showed improved values as can be seen in Fig. 2.13.

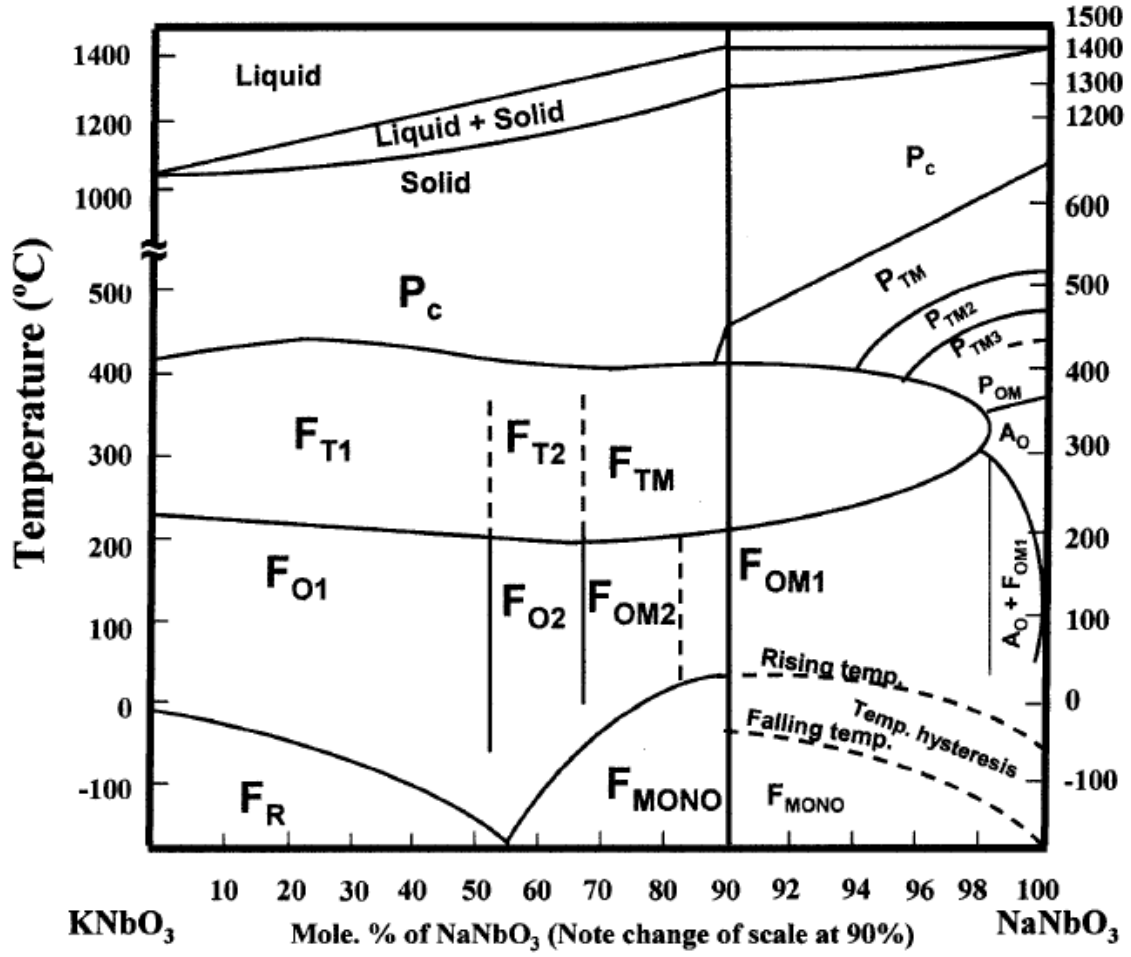

Fig. 2.12. Polymorphic phase diagram of $KNbO_3$-$NaNbO_3$ system. [4]

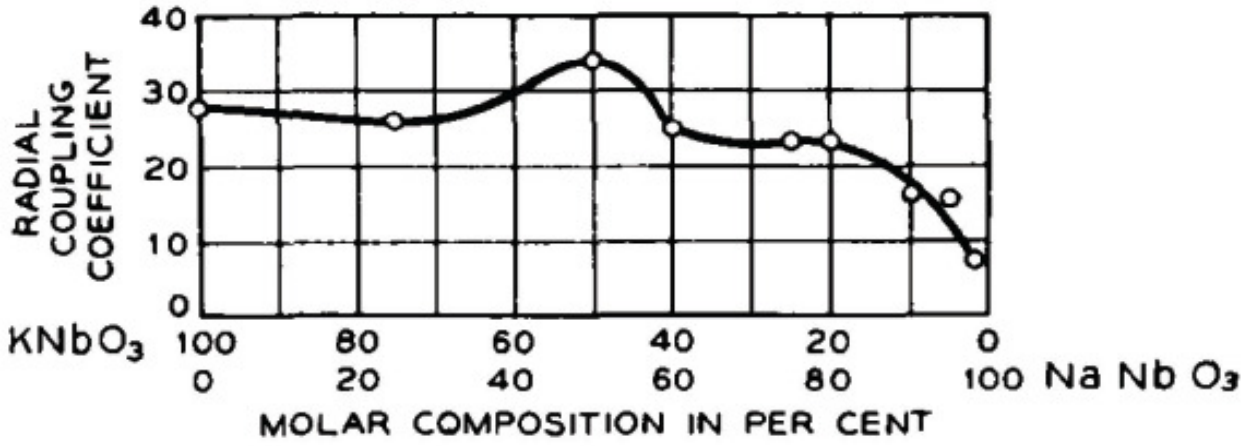

Fig. 2.13. Room temperature radial piezoelectric coupling coefficient of $KNbO_3$-$NaNbO_3$ system. [147]

$K_{0.5}Na_{0.5}NbO_3$ (KNN) ceramics produced via pressure-less sintering do not have good sinterability which leads to poor density of resulting ceramic samples and poor piezoelectric properties. Egerton has reported that hot pressing of KNN ceramics have proven to be an effective method to improve their piezoelectric performance as compared to normal air-fired samples. [35] Fig. 2.14 shows the comparison of dielectric constant and radial coupling coefficients of air-fired and hot-pressed samples for $KNbO_3$-$NaNbO_3$ system. Table 2.1 has summarized the characteristics of $K_{0.5}Na_{0.5}NbO_3$ ceramics at room temperature in air-fired and hot-pressed samples.

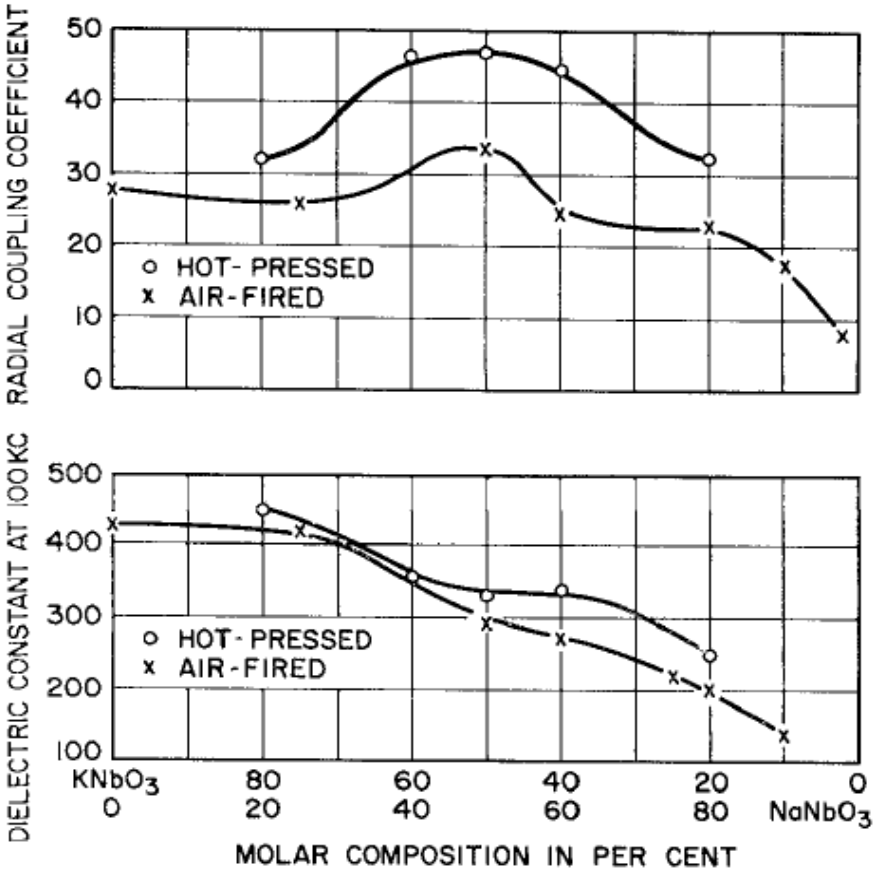

Fig. 2.14. Comparison of dielectric constant and radial coupling coefficients of air fired and hot-pressed samples for $KNbO_3$-$NaNbO_3$ system. [35]

Later on Haertling also used hot pressing method on the same system and confirmed that the maximum electromechanical planar coupling coefficient was observed at the 50/50 composition. [93] Nevertheless, hot-pressing process is not very suitable method for industrial mass production applications.

Table 2.1. Characteristics of $K_{0.5}Na_{0.5}NbO_3$ ceramics at room temperature in air-fired and hot pressed samples. [35]

Property	Air-fired sample	Hot-pressed sample
Dielectric constant (at 100 kHz)	290	420
Electrical *Q* (at 100 kHz)	~50	~70
Specific resistivity (ohm-cm)	$\sim 10^{12}$	$\sim 10^{12}$
Density (g/cm^3)	4.25	4.46
Poisson's ratio (assumed)	0.27	0.27
Frequency constant (Hz-m)	1650	1700
Mechanical *Q*	130	240
Young modulus (N/m^2)	1.04×10^{11}	1.15×10^{11}
Piezoelectric charge coefficient		
d_{33} (pC/N)	80	160
d_{31} (pC/N)	32	49
Piezoelectric voltage coefficient		
g_{33} (mV/N) $\times 10^{-3}$	31.5	43
g_{31} (mV/N) $\times 10^{-3}$	12.6	13.1
Planar coupling coefficient		
k_p	0.36	0.45
k_{31}	0.22	0.27

2.5 Enhancing the properties of lead-free piezoelectric ceramics with perovskite structure

2.5.1 Modified lead-free KNN ceramics

Chemical doping and processing techniques

As we knew earlier from Egerton [35], KNN ceramics have very poor sinterability and often lead to low ceramic density. Although hot-pressing process is able to solve the ceramic density problem, this process is expensive and not convenient for mass production. Thus, this has created interest to researchers to use chemical doping or other processing techniques to improve the properties of KNN ceramics. Below are some reported studies in the literature:

- Addition of ZnO to KNN ceramics was very effective in both improving the piezoelectric properties and preventing the deliquescence problem. It was found that the presence of liquid phase improved the sinterability and might be responsible for the increase in bulk density which led to good piezoelectric properties. Sample with 1 mol% ZnO sintered at 1050 ^{o}C for 2 h possessed good dielectric and piezoelectric properties of $\varepsilon = 500$, $d_{33} = 123$, and $k_p = 0.4$. [148]
- The preparation and introduction of $K_4CuNb_8O_{23}$ (KCN) as sintering additive promoted the sinterability of KNN ceramics. It was confirmed that the formation of liquid phase improved the sinterability of the KNN ceramics. With the addition of 0.5 mol% KCN to KNN ceramics, the density reached 4.40 g/cm^3, which corresponds to 97.5 % of its theoretical density (4.51 g/cm^3), and the electrical properties were also greatly improved (d_{33} = 180 pm/V, Q_m = 1200 and k_p = 0.4). [149] Later on, the same

group also developed a new sintering aid $K_{5.4}Cu_{1.3}Ta_{10}O_{29}$ (KCT) and showed significant improvement in the sinterability of KNN ceramics in air atmosphere. The optimum content of KCT is 0.38% and with this composition KNN ceramics possessed Q_m of 1300, k_p of 0.41 and d_{33} of 190 pm/V. [150]

- The introduction of 0.5 mol% of $AETiO_3$ (AE = Mg, Ca, Sr, Ba) to $(K_{0.5}Na_{0.5})NbO_3$ ceramics was investigated by Y. Chang *et al.* The results showed that adding $CaTiO_3$ and $SrTiO_3$ can promote densification process and improve the electrical properties. The improved properties can be obtained from $CaTiO_3$ as dopant to KNN ceramics (ε = 411, *tan* δ = 0.024, d_{33} = 116 pC/N, k_p = 0.39, Q_m = 176, P_r = 15.7 μC/cm^2, E_c = 8.03 kV/cm and T_c = 397 ^oC). [151]
- By adding 0.5-2 mol% of CuO to KNN ceramics, the densification process was significantly improved and the sintering temperature was lowered. Double polarization-electric hysteresis loops were observed for CuO addition of greater or equal to 0.5 mol%. It is reported the double hysteresis loops are due to defect dipoles that are formed by the acceptor dopant ions Cu^{2+} and O^{2-} vacancies along the polarization direction which remain in the original orientation, giving a strong restoring force to reverse the switched polarization. As a result, sample with CuO doping more or equal to 0.5 mol% possessed extraordinary high Q_m (825-2523) and the electromechanical properties still remained reasonably good where k_p = 39%, k_t = 47% and d_{33} = 82 pC/N). [152]
- D. Lin *et al.* studied that effect of MnO_2 doping and co-doping with MnO_2 and CuO to KNN ceramics. They found out that the doping of MnO_2 and CuO is effective in promoting the densification process through formation of liquid phase and the sintering temperature is reduced by about (100-250 ^oC). KNN ceramics doped with

MnO_2 exhibit piezoelectric properties as follows: d_{33} = 105-108 pC/N, k_p =0.43-0.47 and k_t =0.46-0.48. Furthermore, KNN ceramics co-doped with MnO_2 and CuO possess high Q_m of 1205. [153]

- H. Yang *et al.* reported the preparation of KNN ceramics by Polymerized Complex Method (PC), based on the Pechini-type reaction route. Chemical methods using polymeric precursors have offered an alternative to synthesize small chemically homogeneous particles. The authors used solution-based chemical methods to prepare nanocrystalline KNN ceramic powders. Results showed that dense KNN ceramics sintered at 1100 ^oC were superior to those sintered KNN ceramic counterparts made by conventional solid-state method. [39]
- It is common for KNN ceramics to suffer from abnormal grain growth which leads to poor sinterability. Recently it is found that abnormal grain growth can be suppressed by controlling the sintering atmosphere. Samples sintered in reducing environment show time delay in the onset of abnormal grain growth. Partial roughening of the grain edges and corners can be found in the samples sintered in H_2 atmosphere. It is discussed that the decrease in edge free energy decreases the critical driving force necessary for 2D nucleation-controlled grain growth, causing the grain growth characteristic to change from abnormal to pseudo-normal followed by abnormal growth. [154]
- Another method to densify KNN ceramics has been introduced by means of spark plasma sintering (SPS) instead of conventional hot pressing method. The advantage of this method is rapid heating rate and short soaking time. This allowed sintering temperature as low as 920 ^oC with good density of the ceramics. The dielectric

constant of 606 at 1 kHz and piezoelectric coefficient of d_{33} = 148 pC/N are achieved. [155]

- B. Malic *et al.* have shown addition of ZrO_2 hinders the exaggerated grain growth encountered in KNN. The refinement of the microstructure to the matrix grain-growth inhibition is found to be due to ZrO_2 addition. The dielectric permittivity and loss at 10 kHz, and piezoelectric coefficient d_{33} of KNN-ZrO_2 are 905, 0.04 and 100 pC/N, respectively. [156]
- T. Liu *et al.* studied Sr and Mn codoped KNN ceramics, and found that K^+ volatility was inhibited after Mn doping. It is reported that both low dielectric loss and enhanced thermal stability are due to the pinning effect of Mn-introduced oxygen vacancies. ($tan\ \delta$ = 1.6% and k_p = 41%). [157]
- High volatility of potassium and sodium during heat treatment has obstructed the achievement of stoichiometric KNN ceramics with high density. Recently, Y. Lee at al. have introduced excess K/Na to improve the sinterability and achieved compositions close to stoichiometric compounds. With the excess K (0.44 mol%) / Na (0.22 mol%) in the KNN ceramics, the piezoelectric coupling constant (k_p), quality factor (Q_m), dielectric constant, and piezoelectric coefficient (d_{33}) are approximately 0.341, 116, 361, and 126 pC/N, respectively. [134]

Creating an MPB and shifting of PPT toward room temperature

It is reported that Li, Ta and Sb co-doped KNN materials are promising substitute for current PZT materials, but the preparation of LF4 and LF4T is a complex and difficult process to produce effective piezoelectric materials for

industrial application. [41, 158] Therefore, researchers are exploring new compositions by means of creating an MPB in KNN-based system.

- Lin *et al.* reported that 1-x($K_{0.5}Na_{0.5}$)NbO_3 - x$BaTiO_3$ - y mol% CuO ceramic at x = 0.06 and y = 1.00 exhibits the optimum properties: d_{33} = 193 pC/N, k_p = 0.43, k_t = 0.40, and T_c = 314 °C. Both the Curie temperature (T_c) and orthorhombic and tetragonal polymorphic phase transition temperature (T_{O-T}) decreased with addition of $BaTiO_3$. A MPB was found near room temperature when $0.04 \leq x \leq 0.06$ and y = 1.00 at room temperature. [159]
- Zuo *et al.* reported that 1-x($K_{0.5}Na_{0.5}$)NbO_3 - x$BiFeO_3$, (1-x)KNN - xBF solid solution ceramics exhibited a MPB between orthorhombic and rhombohedral phases near the 1-2 mol% of BF content. On top of that, they found that addition of BF promotes the sintering of KNN ceramics, inhibits the grain growth and improves the ceramic density. The optimum composition of 0.99KNN - 0.01BF ceramics possess superior properties of P_r = 23.3 μC/cm^2, d_{33} = 185 pC/N, and k_p = 46%. [160] The same group also synthesized a solid solution of new lead free 1-x($K_{0.5}Na_{0.5}$)NbO_3 - x$BiScO_3$, (1-x)KNN - xBS ceramics. They reported that with 2 mol%-BS substituted to NKN, a MPB between orthorhombic and rhombohedral phases exists at room temperature. In addition, the polymorphic phase temperature shifted to lower temperature with BS addition. At the MPB composition with x = 0.02, the piezoelectric coefficient d_{33} of 210 pC/N, k_p of 45 %, and T_c of 340 ^oC were achieved. [161]
- Guo *et al.* studied a new composition of 1-x($Na_{0.5}K_{0.5}$)NbO_3 - x$LiTaO_3$ solid solution and found that a MPB between orthorhombic and tetragonal phases existed at x = 5 to 6 mol%. Superior piezoelectric and electromechanical responses, $d_{33} \sim$ 200 pC/N, $k_p \sim$ 36 %, were obtained for those samples with the composition near MPB region. [162]

A few other groups explored $LiTaO_3$-doped KNN system due to its excellent electrical properties. [163-167]

- Yang *et al.* studied a new composition of 1-x$(K_{0.5}Na_{0.5})NbO_3$ - x$LiSbO_3$, (1-x)KNN-xLS solid solution and found that a MPB between orthorhombic and pseudocubic phases coexisted at $0.06 \leq x \leq 0.10$. The 0.94KNN - 0.06LS possessed excellent electrical properties as follows: $d_{33} \sim 171$ pC/N, $k_p \sim 38\%$, and $T_c = 365\ ^oC$ obtained for those samples with the composition near MPB region. [168] This promising material has spurred out some interest to other groups to continue exploring the potential of using $LiSbO_3$-doped KNN to replace existing PZT materials. [98, 169-173]
- Guo *et al.* studied a new lead-free 1-x$(K_{0.5}Na_{0.5})NbO_3$-x$LiNbO_3$, (1-x)KNN - xLN piezoelectric composition exhibiting d_{33} of 200 - 235 pC/N and also very high Curie temperature, T_c = 450 - 510 ^oC. A morphotropic phase boundary between orthorhombic and tetragonal phases is found in the composition range $0.05 < x < 0.07$. [72] Till date, there are many researchers who still are extensively exploring this material system due to its excellent piezoelectric properties and high T_c which is suitable for high temperature applications. [174-204]

2.5.2 Modified lead-free BTO ceramics

Chemical doping and processing techniques

It is well known that $BaTiO_3$ possesses moderate piezoelectric coefficient, and currently is more popular for dielectrics applications. [205] Many researchers are trying to modify or tailor the $BaTiO_3$ electrical properties to make it more competitive

for piezoelectric applications. Only recently, there is a breakthrough in an optimized $Ba(Zr_{0.2}Ti_{0.8})O_3$ - $(Ba_{0.7}Ca_{0.3})TiO_3$ ceramic, abbreviated as BZT – BCT. It is found that at 50 mol% BZT - 50 mol% BCT, the ceramic possessed outstandingly high piezoelectric constant of 300 - 600 pC/N. [73] However, the Curie temperature is very low, T_c of 93 ^oC, and the complicated ceramic processing involving multiple steps, makes it difficult for practical applications. Since then, there are increasing studies on Ca and Zr co-doped $BaTiO_3$ based ceramics. [206-214]

- Bao *et al.* reported that $(1-x)Ba(Zr_{0.15}Ti_{0.85})O_3$ - $x(Ba_{0.8}Ca_{0.2})TiO_3$ showed a higher T_c of 114 ^oC at x = 0.53 by lowering the amount of Ca and Zr content. However, the piezoelectric coefficient d_{33} decreases significantly from the reported 600 pC/N by Liu and Ren [73] to 450 pC/N. They also found that the d_{33} along the morphotropic phase boundary (MPB) decreased when it deviated away from the cubic-tetragonal-rhombohedral triple critical point. [215]

Creating an MPB and shifting of PPT

The stoichiometric formula of the optimum $0.5Ba(Zr_{0.2}Ti_{0.8})O_3$-$0.5(Ba_{0.7}Ca_{0.3})TiO_3$, (BZT-BCT) composition can be calculated and written as $Ba_{0.85}Ca_{0.15}Zr_{0.1}Ti_{0.9}O_3$, (BCZT). Researchers have been interested to explore this system in more convenient and cost effective approach through single step mixed oxide solid state synthesis route.

- Li *et al.* have studied the Ca effects on BCZT ceramics system using conventional solid state reaction method. Their study identified the coexistence of rhombohedral and orthorhombic phases around room temperature in the composition range $0.14 < x < 0.18$. The optimum ceramic at x = 0.16 shows enhanced piezoelectric coefficient of

d_{33} = 328 pC/N, k_p = 37.6 % and dielectric constant ε = 4800. The polymorphic phase transition shifts toward lower temperature with increasing Ca amount. [216] Further studies were also done by Li and his group by increasing the Ti content in BCZT system while still optimizing the Ca doping amount. They reported that lead-free $(Ba_{1-x}Ca_x)(Ti_{0.98}Zr_{0.02})O_3$ at x = 0.01 ceramic exhibits high piezoelectric coefficient of d_{33} = 375 pC/N and planar electromechanical coupling factor of k_p = 44.1 % while maintaining relatively high Curie temperature T_c value of ~115 ^oC. The MPB between orthorhombic and tetragonal phases around room temperature were identified in the composition range of $0 < x < 0.03$. With the increase of Ca doping amount, the orthorhombic-tetragonal PPT temperature shifted towards room temperature. [217]

- Zhang *et al.* studied the effects of Zr content on lead-free $(Ba_{0.95}Ca_{0.05})(Ti_{1-x}Zr_x)O_3$ ceramics prepared by the solid-state reaction method and sintered in a reducing atmosphere. They found coexistence of orthorhombic and pseudocubic phases at $5 \leq x \leq 7$ mol%. The orthorhombic to pseudocubic PPT temperature was shifted towards room temperature. Piezoelectric coefficient of d_{33} = 338 pC/N, electromechanical coupling coefficient of k_p = 36 % and dielectric constant of 2070 were obtained at x = 4 mol%. [218]
- Recently, Xue *et al.* have designed another promising lead-free system that possesses similar tricritcal point as published in BZT-BCT system by Liu and Ren. [73] In their lead-free composition $Ba(Sn_{0.12}Ti_{0.88})O_3$ - $x(Ba_{0.7}Ca_{0.3})TiO_3$, (BST - xBCT), the Zr is replacing Sn. It is reported that at optimal composition of BST-30BCT, a high piezoelectric coefficient of d_{33} = 530 pC/N is obtained. However, the Curie temperature has reduced to ~ 75 ^oC. [219]

Chapter 3

Characterization Methodology

3.1 Thermal analysis on uncalcined powders

Prior to the thermal analysis, the uncalcined powders are first dried in an oven at 120 °C for 1 day. Thermogravimetry analysis - differential scanning calorimetry (TGA-DSC, SDT2960, TA Instruments, USA) instrument simultaneous SDT 2960 was used to study the decomposition temperature of organic compounds and the crystallization temperature of oxides. [220] TGA-DSC system is used to study the weight loss and heat flow of the uncalcined powders. The experiment was conducted from room temperature to 1000 °C with different ramping rates of 10, 20, 30, 50 °C/min in air ambient. TGA continuously records the weight change as a function of temperature and time. Differential Scanning Calorimeter (DSC) measures the heat flow that is emitted or absorbed from the sample as a function of time and temperature. [220]

3.2 Structures and morphologies

Prior to the X-ray powder diffraction (XRD) analysis, the surfaces of the ceramic pellets were polished using a 1000 grid SiC paper for 10 min followed by washing in water and drying in an oven at 120 °C for 15 min. As for X-ray photoelectron spectroscopy (XPS) analysis, the ceramic powders calcined at different temperatures were examined.

3.2.1 X-ray diffraction (XRD)

X-ray powder diffraction (XRD) is a technique used to determine the crystal structure, crystallite size and preferred orientation of polycrystalline samples. [221] By

comparing the XRD patterns with the databases in International Centre for Diffraction Data, the crystalline phases can be identified. In this work, crystallographic phases of both KNN and BCZT-based ceramics were examined with XRD (D8-ADVANCED, Bruker AXS GmbH, Karlsruhe, Germany), GADDS (General Area Detection Diffraction System) system at room temperature. Cu Kα radiation with λ = 0.15418 nm was used as the incident X-ray and the Bragg angle, 2θ was scanned between 10° and 65°.

3.2.2 X-ray photoelectron spectroscopy (XPS)

XPS is a surface chemical analysis technique used to study the elemental composition, chemical and electronic state of the surface of a sample. [222] In this work, the binding energy of potassium, sodium, niobium, and oxygen elements in KNN-based ceramics were identified using XPS (VG ESCALAB 2201-XL Imaging System, East Sussex, U.K.) under argon environment. XPS profiles of the samples were obtained using Al Kα source (1486.6 eV). C_{1s} peak (284.5eV) is used as the standard reference.

3.2.3 Fourier transform infrared spectroscopy (FTIR)

FTIR is a powerful tool for identifying the types of functional groups or chemical bonds in an organic or inorganic compound by producing an infrared absorption or transmittance spectrum which is like a "fingerprint" of the compound. [223] For KNN-based ceramics in this work, the FTIR (Spectrum 2000, Perkin Elmer, Waltham, MA) system was used to investigate the interactions of the uncalcined powders with PVP polymer. The samples were scanned at wavenumbers ranging from 400 cm^{-1} to 4000 cm^{-1} at room temperature.

3.2.4 Scanning electron microscopy (SEM)

SEM is a useful tool for examining the morphology of a material by scanning the surface of material by a focused beam of electrons, generated in an electron gun. The electron beam interacts with electrons in the material producing various signals, like secondary electrons and back scattered electrons, which then are converted into an image. It is used to determine the grain size and morphology of samples. [224] In this work, the surface morphology of KNN-based ceramics and BCZT based ceramics were examined with SEM (JSM-4700F, Tokyo, Japan) operated at 5 kV. Prior to the imaging process, ceramic samples were polished and thermal-etched at 100 ^{o}C below sintering temperature for 15 min with a ramp rate of 10 ^{o}C/min. They were put on a conductive double sided carbon tape and sputtered with a thin layer of gold for better conductivity for minimizing charging effects during observation.

3.3 Electrical properties

For the characterization of electrical properties (dielectric, ferroelectric and piezoelectric properties) of both KNN-based and BCZT-based ceramics, disk samples were polished to a thickness of 0.8 mm using a silicon carbide paper of 1200-grid size. To form electrodes, both sides of the circular disk samples were then coated with silver paste and dried in a conventional oven at 120 ^{o}C for 15 min to remove the organic solvent. Samples were then transferred to a high temperature furnace for silver paste firing at 550 ^{o}C for 15 min at ramp rate of 10 ^{o}C/min to form the silver electrodes with improved adhesion. The detailed state-of-the art individual property testing is as follows:

3.3.1 Dielectric properties

Impedance analyzer was used to measure the circular disk capacitance and loss tangent as a function of the frequency. The capacitance (C) and loss tangent values of the circular ceramic disks were measured between top and bottom electrodes of the sample. The capacitance (C) and tangent loss (*tan δ*) of the ceramics in this work were measured with a impedance analyzer (HP4294, Agilent Technologies Inc., Hyogo, Japan). The dielectric constant (ε_r) was calculated from equation (3.1) below:

$$\varepsilon_r = \frac{\mathrm{C} \times \mathrm{t}}{\varepsilon_o \times \mathrm{A}} \tag{3.1}$$

where C is the capacitance, t is the circular disk thickness, ε_o is the permittivity of free space with the value of 8.85 x 10^{-12} F/m, and A is the area of the electrodes. [225] Temperature dependent dielectric spectroscopy was also performed on KNN-based and BCZT-based ceramics to investigate the polymorphic phase transition temperature and Curie temperature.

3.3.2 Ferroelectric properties

Ferroelectric materials have spontaneous electric polarization that can be reversed by application of an external electric field. [226] In this work, the ferroelectric properties of both KNN and BCZT-based ceramics were characterized by obtaining the polarization and electric field (P-E) hysteresis loops connected with a high voltage interface using standard ferroelectric test system, (Premier II, Radiant Technologies Inc., Albuquerque, NM). In order to prevent electric arcing, the samples were submerged in silicone oil during measurements. The remnant polarization (P_r) and coercive field (E_c) are determined from the saturated

hysteresis loops. A ferroelectric testing jig was customized as shown in Fig 3.1 to hold the ceramic samples properly in the silicone oil.

Fig 3.1 Customized in-house jig for ferroelectric testing.

3.3.3 Poling process

Ferroelectric polycrystalline ceramics have randomly oriented domains with spontaneous polarization, and the net polarization could be equal to zero. By applying high external DC voltage to the ferroelectric ceramics, the net polarization can be obtained to get the piezoelectric effect, which is called poling. [227] The poling process aligns the dipoles of each domain parallel to the applied electric field direction and three important variable parameters can be varied: the time, the temperature, and the electric field. In order to prevent breakdown due to high electric leakage, materials need to possess high resistivity and breakdown strength. If the materials are poled at high temperature, much lower poling field is needed due to the decreased coercive field. It is important to take note that the poling field needs to be maintained during cooling to prevent de-poling due to domain re-switching. Our in-house poling jig was improved to pole up to maximum 6 pellets at one time as shown in Fig. 3.2.

Fig. 3.2. Customized in-house jig for poling of multiple samples.

3.3.4 Piezoelectric properties

Piezoelectric materials are able to generate an electric potential when mechanical stress is applied. The direct piezoelectric effect is known as generation of electric charges when applying external mechanical stress. The reverse piezoelectric effect is known as induced stress or strain due to an applied electric field. The piezoelectric constant was measured using a piezoelectric-d_{33} meter (ZJ-4B, Institute of Acoustics, Chinese Academy of Sciences). [225]

3.3.5 Planar electromechanical factor

For a poled ceramic disk, the planar electromechanical factor, k_p, is defined as the coupling between electric field parallel to the ceramics poling direction. The k_p was determined by the "resonance and anti-resonance" technique using an impedance analyzer, and calculated from the following equation:

$$1/k_p^2 = 0.395[f_r/(f_a - f_r)] + 0.574 \qquad (3.2)$$

where f_r and f_a are the resonance and anti-resonance frequencies, respectively. [228]

Chapter 4

Lead-free KNN-LN ceramics prepared by ultrasonic irradiation method

4.1 Introduction

Lead-free $0.94(K_{0.5}Na_{0.5})NbO_3$ - $0.06(LiNbO_3)$ (0.94KNN - 0.06LN) piezoelectric ceramic is a very promising material because of its excellent d_{33} and T_c values. [72] Therefore, the study in this chapter is conducted on the 0.94KNN - 0.06LN ceramic system. Presently, majority of the ceramic preparation process based on solid state reaction involves mechanical ball milling process, typically longer than 24 h, which is costly and time consuming. Most importantly, the probability of introducing contaminations during the long hour milling process is high. Therefore, to reduce long mechanical milling process, alternative processing scheme should be developed in synthesizing lead-free KNN-LN piezoelectric ceramics.

It is reported that employing high power ultrasound in solid state reaction can generate great impact on products quality through modification of the surface morphology. Ultrasound can enhance the reaction rate and reduce the reaction temperatures. [106] To the best of our knowledge, the research on ultrasonic irradiation effects on lead-free KNN-based ceramics have not been investigated and reported before our study.

Chapter 4 focuses on the investigation of the effects of ultrasonic irradiation on the structure-property relationship of lead-free KNN-LN ceramic, as well as to obtain at a low cost dense ceramic without special powder handling process like cold isostatic pressing. The

first observation of ultrasound's ability to selectively accelerate the elementary steps in 0.94KNN-0.06LN formation was reported. As a result, the rate-determining step was found to change as a result of sonication at room temperature. This observation was obtained through the quantitative study of the solid state reaction kinetics of KNN-LN formation as a function of ultrasound irradiation conditions.

4.2 Experimental procedures

The material composition selected for this study is $0.94(K_{0.5}Na_{0.5})NbO_3$ - $0.06LiNbO_3$ (0.94KNN-0.06LN) with 1 mol% of excess K, Na. K_2CO_3 (99.5 %), Na_2CO_3 (99.0 %), Li_2CO_3 (99.999 %), Nb_2O_5 (99.9 %) (Alfa Aesar) were used as the starting raw materials. From our previous unpublished work, 1 mol% excess K, Na to compensate their loss during heat treatment could lead to improved electrical properties as compared to non-excess compositions. As the three carbonate powders are moisture sensitive, they were dried prior to synthesis process to avoid compositional deviations. The dried powders were then stoichiometrically weighed and subsequently dispersed in ethanol in a beaker and treated for 30 min with ultrasonic irradiation using a direct-immersion titanium horn (Sonics VCX500, 20 kHz, 500 W, Sonics & Materials, Inc., Newtown, USA) with different ultrasonic powers. The level of irradiation is varied by choosing different amplitude settings in the Sonics VCX500 instrument, in percentage of the maximum amplitude. The energy expended to sonicate the sample for each amplitude setting is displayed at the end of sonication. From the data, power input, in watts, can be calculated. During the ultrasonic treatment, the temperature increased and controlled by a temperature thermocouple at 60 ^{o}C. To study the reaction kinetics by thermo-gravimetric analysis-differential scanning calorimetry (TGA-DSC, SDT2960, TA Instruments, USA) the sonicated slurry was dried and crushed using

agate mortar and pestle. The TGA-DSC analysis was conducted in air with a heating rate ranging between 10-50 °C. X-ray diffraction (XRD) was performed in parallel, to determine the structural evolution at different temperatures during the thermal analysis process.

To understand the ultrasonic effects on the starting materials, samples of K_2CO_3, Nb_2O_5 and the mixture of the reactants according to 0.94KNN-0.06LN formula comprising of K_2CO_3, Na_2CO_3, Li_2CO_3 and Nb_2O_5 powder were treated with different ultrasonic powers. The slurries were dried after the ultrasonic treatment and the obtained powders were characterized with particle size analyzer. After the ultrasonication process, the slurry was dried and crushed using agate mortar and pestle and calcined at 850 ^{o}C for 5 h in an alumina crucible. Only the calcined powders were ball milled for 4 h using planetary milling. After the powders were ground and mixed with 4 wt% polyvinyl butyral (PVB) as a binder, they were uniaxially pressed into disks with a diameter of 10 mm and a thickness of about 1.8 mm without using cold isostatic pressing (CIP).

The disk samples were sintered at 1050 ^{o}C for 2 h in air. Bulk densities of the sintered disk samples were measured using mass and geometrical dimension. All samples were poled at 120 ^{o}C for 30 min under direct current field of 40 kV/cm for piezoelectric measurement.

4.3 Results and discussions

4.3.1 Crystalline structure of sintered ceramics

Figure 4.1(a) shows the XRD patterns of the 0.94KNN-0.06LN ceramic samples sintered at 1050 ^{o}C for 2hrs. The peaks of orthorhombic and tetragonal structure were indexed in terms of $KNbO_3$ (JCPDS No. 32-0822) and (JCPDS No. 71-0945), respectively. It can be seen from Fig. 4.1(a) that a single-phase perovskite structure was formed with ultrasonic power of 52 watts – (labeled as 52W-US), whereas a small amount of secondary phase of Li_3NbO_4 was detected in the samples with ultrasonic power at 5, 13 and 28 watts (labeled as 5W-US, 13W-US and 28W-US, respectively). The observed secondary phases as the representative of Li_3NbO_4 in our 0.94KNN -0.06LN ceramic can be indexed clearly with the standard JCPDS data file (82-1198) as reference.

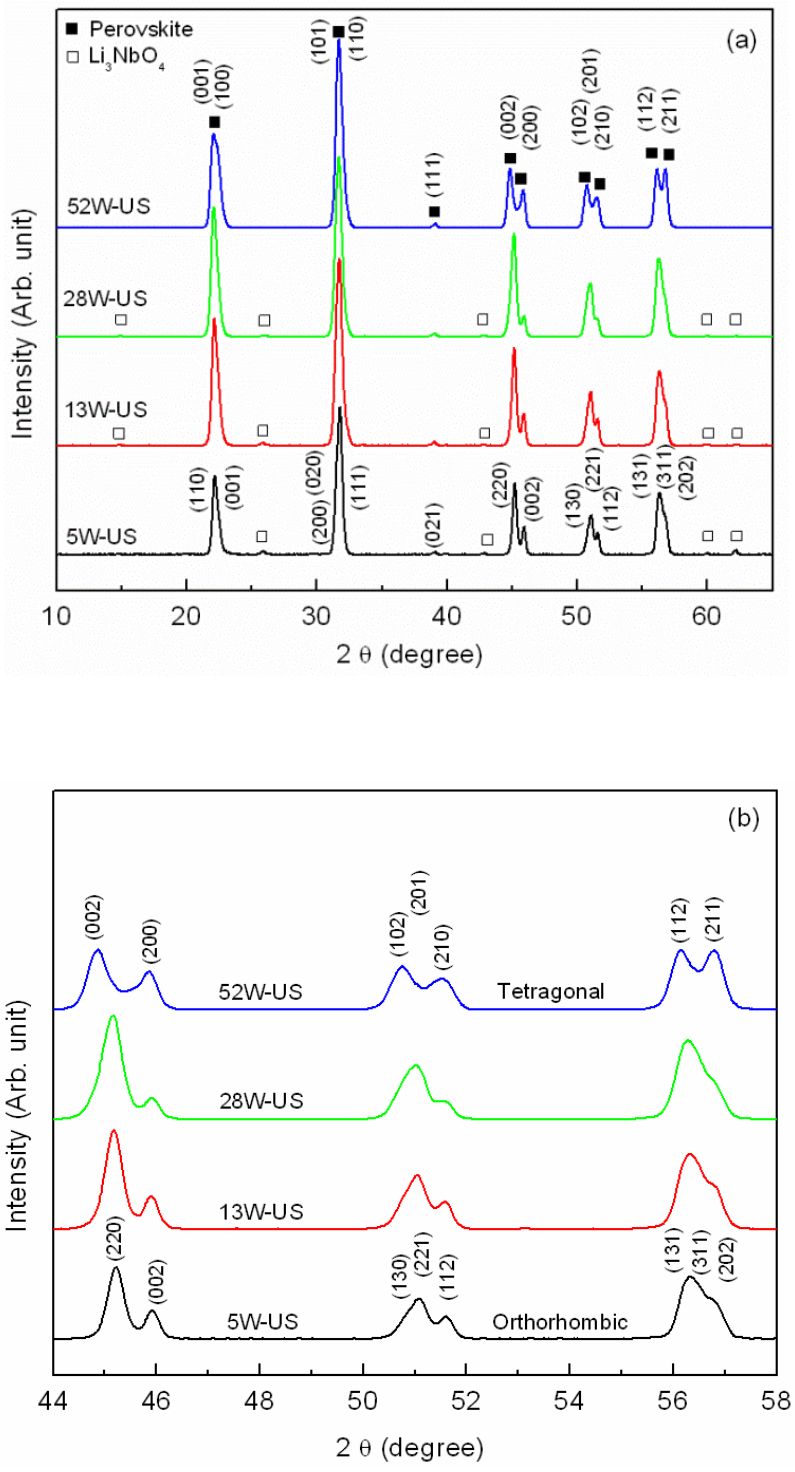

Fig. 4.1. XRD patterns of the 0.94KNN-0.06LN ceramics sintered at 1050 ^{o}C for 2 h, (a) 2θ in the range of 10 - 65°, and (b) 2θ in the range of 44 - 58°.

The zoomed XRD patterns of the ceramics in the range of 2θ from 44^{o} to 58^{o} are shown in Fig. 4.1(b). It can be clearly seen when the ultrasonic power increases from 5 W to 52 W, the orthorhombic peaks of (220), (002), (130), (221), (112), (131), (311) and (202) transforms to tetragonal peaks of (002), (200), (102), (201), (210), (112) and (211), which illustrates the gradual transformation from orthorhombic to tetragonal phase in the ceramics derived from increased ultrasonic power. In the literature study, it is reported that the orthorhombic and tetragonal phase coexisted for 0.94KNN-0.06LN ceramic with Li substitution in the lattice, and the tetragonal phase was characterized by (002)/(200) peak splitting at about 45^{o}. [72] The results here thus indicate that increasing the ultrasonic power caused the structural phase transition due to increased solubility of Li substitution, which will responsible for the improved piezoelectric properties as expected from the solid solution of KNN-LN.

Figure 4.2 shows the XRD patterns of 0.94KNN-0.06LN ceramic samples calcined at 450 ^{o}C for 5 hrs. As the decomposition of carbonates starts at 420 ^{o}C as mentioned in the literature, [229] all the samples were calcined at 450 ^{o}C to examine the phase evolution at the initial reaction stage. The XRD peak at 32^{o} in 2θ range can be referred for perovskite phase detection as the peak at 22^{o} in 2θ could be overlapped with Nb_2O_5 peaks. As shown in Fig. 2, perovskite phase formation was promoted for 28W-US and 52W-US at 450 ^{o}C. Whereas, for 5W-US and 13W-US samples, large amount of intermediate phases of $K_4Nb_6O_{17}$, $Na_2Nb_4O_{11}$, Nb_2O_5, and some residue carbonates are detected. It is important here to take note that ultrasonic irradiation energy increased the reaction rate significantly and promoted the perovskite phase formation.

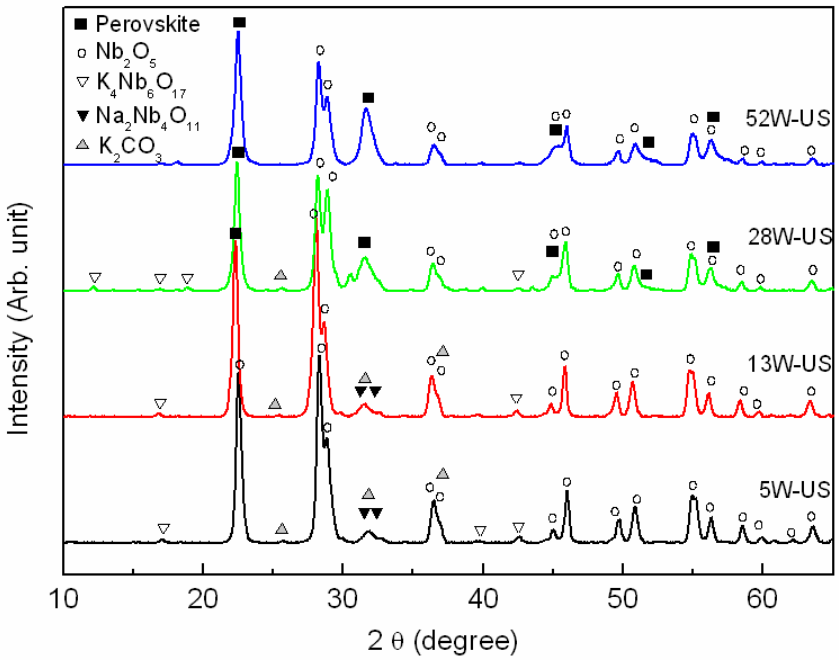

Fig. 4.2. XRD patterns of 0.94KNN-0.06LN ceramic powders treated with ultrasonic irradiation of different powers calcined at 450 ^{o}C for 5 h.in air atmosphere.

4.3.2 XPS analysis

Figure 4.3 shows XPS spectra of K 2*p* for 0.94KNN-0.06LN ceramic powders calcined for 5 h at 450 ^{o}C. The samples calcined at 450 ^{o}C for 5W-US and 13W-US showed two peaks for K 2*p*, labeled as K $2p_{1/2}$' and K $2p_{3/2}$' which were attributed to K ions before crystallized into perovskite phase. It has been reported that the XPS peaks for the $K_4Nb_6O_{17}$ phase as present in the XRD result in Fig. 4.2 have the binding energy (BE) of K $2p_{1/2}$' at 295 eV and K $2p_{3/2}$' at 292 eV. [230] The K in non-crystalline oxide structure also exhibited XPS peaks corresponding to these two binding energies in the literature. [129] In contrast, there were additional two peaks for samples 28W-US and 52W-US, labeled as K $2p_{1/2}$ and K $2p_{3/2}$, which shifted by ~ 1.5-1.6 eV toward lower binding energy (BE) from K $2p_{1/2}$' and K $2p_{3/2}$', respectively. These additional two peaks at lower binding energies are also reported previously to appear accordingly with KNN perovskite phase formation. [129] Therefore, the

additional two peaks detected are an indication of the crystallization of perovskite structure, which can be confirmed by XRD results in Fig. 4.2. However, 5W-US and 13W-US samples did not clearly exhibit peaks of K $2p_{1/2}$ and K $2p_{3/2}$, which indicated that perovskite formation is delayed to higher temperature. Therefore, the results indicated that the perovskite phase formation was promoted at lower temperature with increasing the ultrasonic irradiation power.

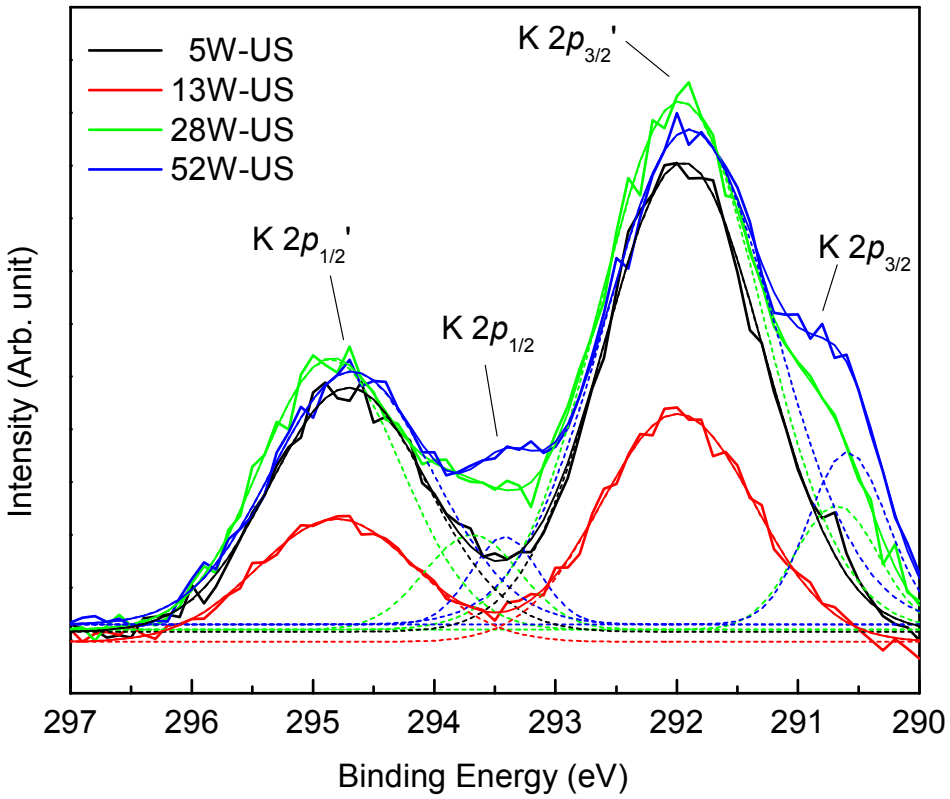

Fig. 4.3. XPS spectra of K 2*p* for 0.94KNN-0.06LN ceramic powders treated with ultrasonic irradiation of different powers calcined at 450 ^{o}C for 5 h.

Figure 4.4(a) shows the XPS spectra of O 1*s* for the 0.94KNN-0.06LN powders calcined for 5 h at 450 ^{o}C. By analyzing the peaks at 531 eV, we can obtain the information about the decomposition of carbonates in the samples. It can be noted by increasing the ultrasonic power from 5 W to 52 W, the peaks were reduced greatly and further reduction was observed

at 550 ^{o}C, as shown in Fig. 4.4(b). Comparing the XPS data peaks at 531 eV for the different samples, clearly that high ultrasonic power led to decomposition of carbonates at lower temperature, and therefore the perovskite phase formation was promoted.

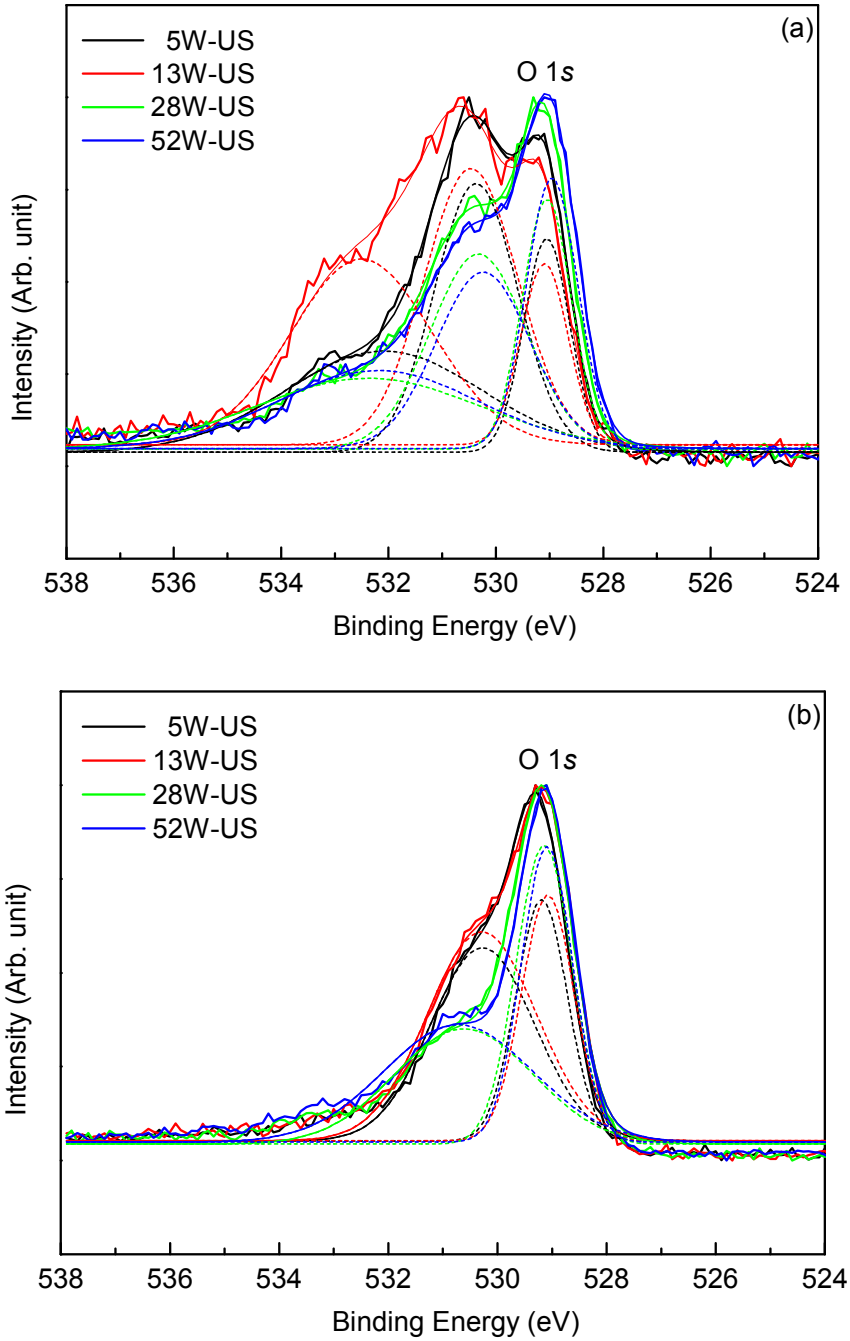

Fig. 4.4. XPS spectra of O 1*s* for the 0.94KNN-0.06LN ceramic powders treated with ultrasonic irradiation of different powers calcined at (a) 450 ^{o}C and (b) 550 ^{o}C for 5 h.

4.3.3 Thermal analysis

Figure 4.5 presents the thermogravimetric (TG) curves of 0.94KNN-0.06LN powders after the ultrasonic irradiation and dried at 120 ^{o}C. According to the literature, the decomposition of the hydrated sodium carbonate to sodium carbonate occurs at a temperature between 100-180 ^{o}C, [231] and the decomposition of hydrated potassium carbonate also occurs below 200 ^{o}C. [232] As observed in Fig. 4.5, for the powders treated with increased ultrasonic power, including 13W-US, 28W-US and 52W-US, weight loss below 223 ^{o}C was below 1.4 %, which was attributed from the elimination of water. However, 5W-US sample had much higher water absorption, which was reflected by the large weight loss of 4.5 % below 223 ^{o}C. It seemed that the high power ultrasonic irradiation could help to suppress the hydration of the carbonates or facilitate the dehydration.

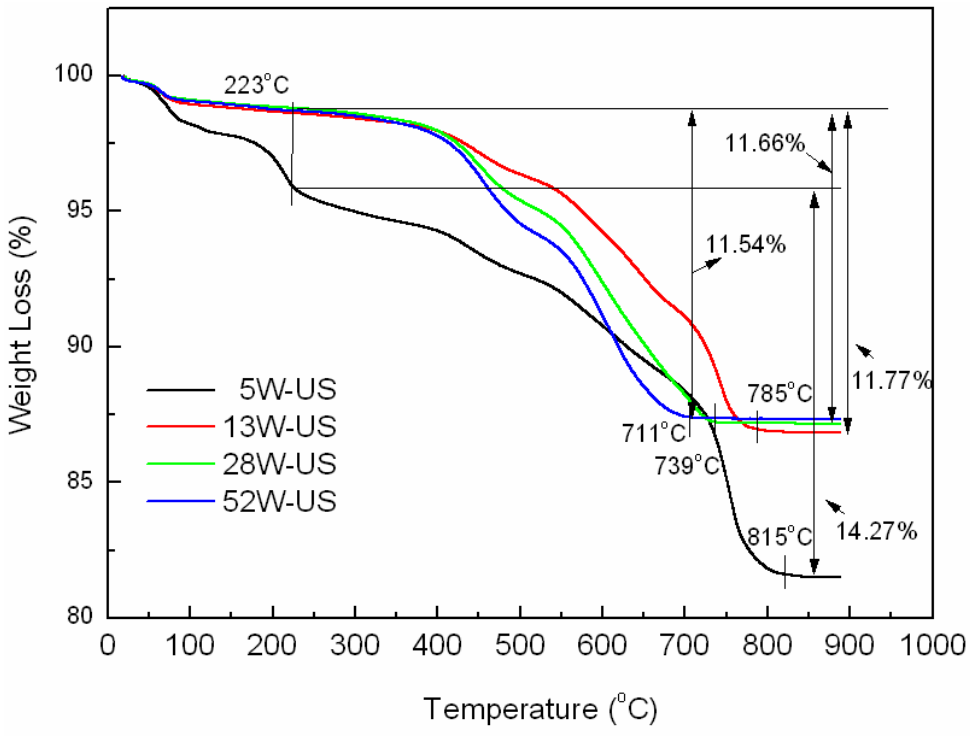

Fig. 4.5. TGA curves of 0.94KNN-0.06LN ceramic powders after the ultrasonic irradiation.

The theoretically calculated weight loss from all the carbonate decomposition is 11.55 %. From the TG curves in Fig. 4.5, the weight loss after the complete dehydration at 223 ^{o}C for 5W-US, 13W-US, 28W-US and 52W-US samples are 14.27 %, 11.77 %, 11.66 % and 11.54 %, respectively. The overall weight loss after dehydration matched well with the calculated one from the carbonate decomposition when the ultrasonic power increased. However, it was noted that there was a significant additional weight loss for 5W-US sample. The larger weight loss with decreasing ultrasonic irradiation power implied that there was a certain amount of alkali composition loss during heat treatment. For the TG curves in Fig. 4.5, the slope becomes steeper in the temperature range of carbonate decomposition from 400 to 700 °C as the ultrasonic power increases; this indicates the faster carbonate decomposition process for the powder treated with ultrasonic irradiation of higher power, which led to earlier perovskite phase formation as confirmed by XRD results in Fig. 4.2. The results indicate that high power ultrasonic irradiation treatment accelerated the decomposition of carbonates and promoted the perovskite phase formation at lower temperature. This is very crucial because the alkali compositions are much more volatile at the moderate temperature before they are crystallized into the perovskite phase than after the crystallization at high temperature, as our group observed before. [129] As shown in Fig. 4.5, higher power of the ultrasonic irradiation consistently resulted in smaller overall weight loss due to the suppressed alkali loss, although faster weight loss due to carbonate decomposition. The weight loss stopped at lowered temperature from 815 ^{o}C to 711 ^{o}C for 5W-US and 52W-US samples, respectively.

4.3.4 Density and weight loss analysis

Figure 4.6 shows the bulk density and weight loss of 0.94KNN-0.06LN ceramic samples sintered at 1050 ^{o}C for 2 h. As shown in Fig. 4.6, the bulk density of 0.94KNN-0.06LN increased with increasing ultrasonic power, reaching the value of 4.24 g/cm^3 at the ultrasonic energy of 52 W. Compared to the theoretical density of $K_{0.5}Na_{0.5}NbO_3$ of 4.51 g/cm^3, the relative density was 94 %. The mechanism of increasing bulk density of 0.94KNN-0.06LN with increasing ultrasonic power will be discussed further in later section 4.3.7. The weight differences in samples were recorded before and after sintering, and the weight loss during the sintering process decreased with increasing the ultrasonic power. This decrease in weight loss during sintering further indicated that low volatility of alkali metal ions can be achieved by using ultrasonic irradiation with high ultrasonic power and dense ceramic can be achieved without using CIP.

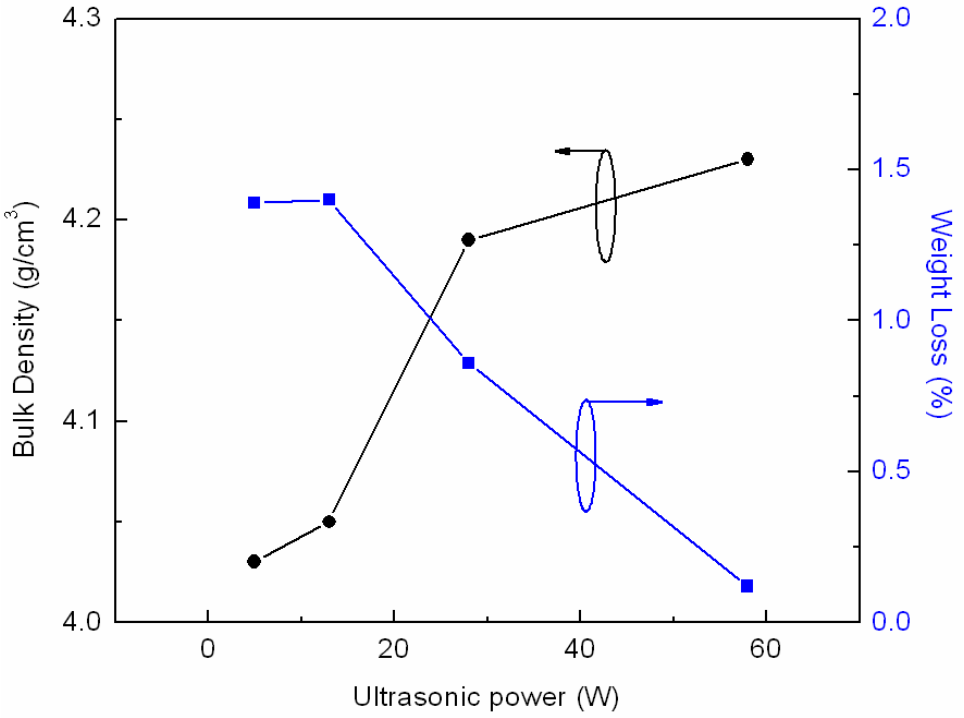

Fig. 4.6. Density and weight loss of 0.94KNN-0.06LN ceramics sintered at 1050 ^{o}C for 2 h in air atmosphere.

4.3.5 Surface morphology

Figure 4.7 shows the surface morphology after polishing and thermal etching for 0.94KNN-0.06LN ceramic samples sintered at 1050 ^{o}C for 2 h. It can be seen that the average grain size for 5W-US and 13W-US as shown in Fig. 4.7 (a) and (b) is about 30 μm , and the average grain size is reduced to 22 μm and 14 μm for 28W-US and 52W-US as shown in Fig. 4.7 (c) and (d). To estimate the average grain size, linear straight lines were drawn across the micrograph and the numbers of grains intercepted with the lines were counted, with the length of the straight line divided by the number of grains intercepted. Large pores exist in 5W-US and 13W-US, but only smaller pores are noted in 28W-US and 52W-US with improved dense morphology. Therefore, it is clear that the ceramic samples derived from ultrasonic irradiation with higher power, 28W-US and 52W-US, exhibited a denser and more homogenous morphology than those processed with lower power irradiations, 5W-US and 13W-US.

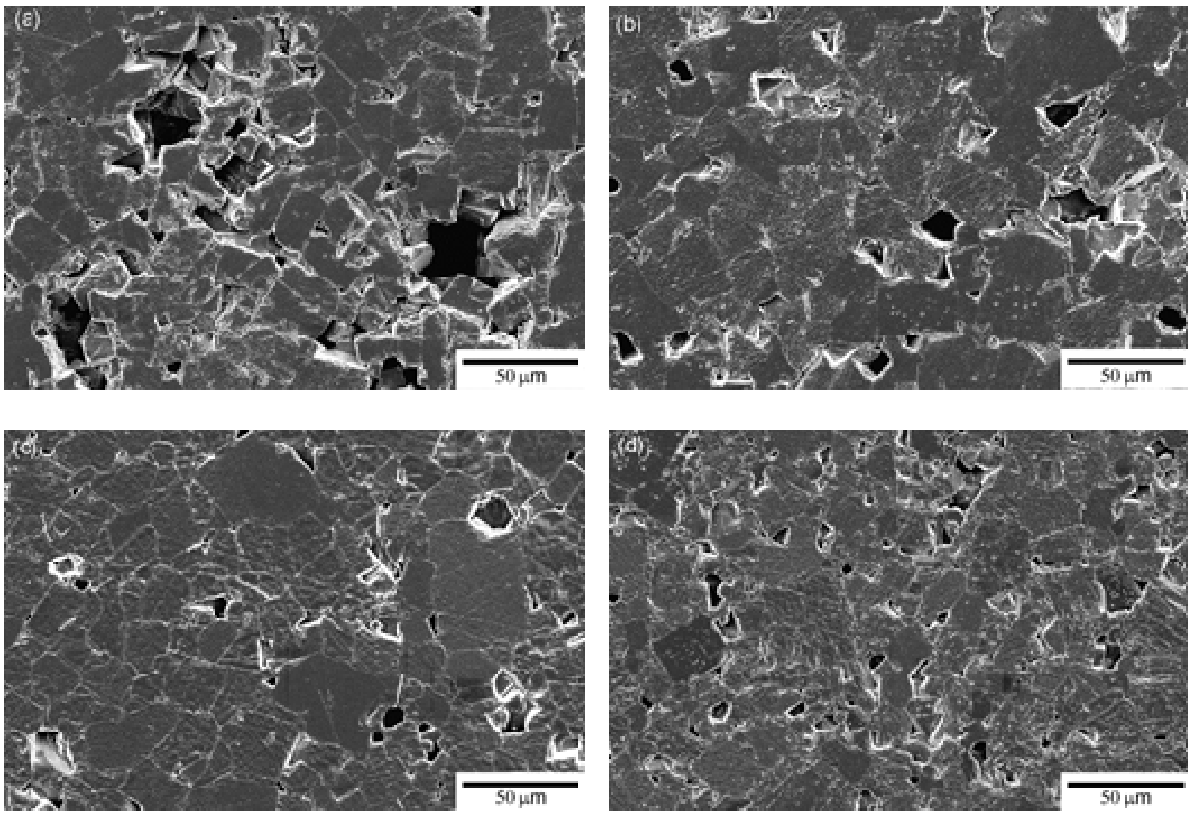

Fig. 4.7. Surface morphology of polished 0.94KNN-0.06LN ceramic samples sintered at 1050 ^{o}C for 2 h, (a) 5 W-US, (b) 13 W-US, (c) 28 W-US, and (d) 52 W-US.

4.3.6 Electrical properties

The density, dielectric and piezoelectric properties of the 0.94KNN-0.06LN ceramic samples sintered at 1050 ^{o}C are summarized in Table 4.1. The relative density of the samples was increased from 89.3 % to 94 % with increasing ultrasonic power to 52 W. For 28W-US and 52W-US, the piezoelectric properties were improved significantly. The d_{33} value for 52W-US ultrasonic samples was 184 pC/N, with dielectric constant and loss of 630 and 0.01, respectively.

Table 4.1. Relative density, weight loss, grain size, dielectric and piezoelectric properties of 0.94KNN-0.06LN ceramics sintered at 1050 ^{o}C for 2 h.

Samples	Density (g/cm^3)	Relative density (%)	Grain size (μm)	Weight loss* (%)	d_{33} (pC/N)	Dielectric constant at 1 kHz	Loss tangent at 1 kHz
Ball milled	4.05	89.8	19	1.44	80	280	0.03
5W-US	4.03	89.3	30	1.39	-	-	4.15
13W-US	4.05	89.8	30	1.4	-	-	0.55
28W-US	4.19	92.9	22	0.86	130	370	0.06
52W-US	4.24	94.0	14	0.12	184	630	0.01

*Note: The weight loss indicates the weight difference in percentage of the pellets before and after sintering.

As reported in the literature for 0.94KNN-0.06LN composition using 24 hrs of ball milling (versus our 30 min ultrasonic irradiation) for the powder mixing, the piezoelectric coefficient d_{33} varied in the range between 130 to 215 pC/N. [179, 233] For a comparison, we cited previous batch of 0.94KNN-0.06LN from the conventional ball milling method using planetary ball milling for 24 hrs for the raw powders and ball milling for another 12 h after calcination without CIP. The sample was also sintered at 1050 ^{o}C for 2 h, and the results are labeled as Ball milled in Table 4.1. Despite the long and tedious ball milling process, the ball milled sample had a low density of 89.8 % and poor piezoelectric properties, which could be due to the absence of CIP to achieve high ceramic density. These results showed that high density and competitive electrical properties could be achieved with fast and effective ultrasonic irradiation method for 0.94KNN-0.06LN ceramic. For 5W-US and 13W-US ultrasonic samples, the piezoelectric properties could not be tested because the ceramics were unable to be poled due to the high conductivity, possibly as a result of incomplete mixing and

the low density. The measured dielectric constant data are not included in Table 4.1 for these two samples in consideration of their high dielectric loss.

The important factor that affects the piezoelectric properties of 0.94KNN-0.06LN is the composition control and coexistence of orthorhombic and tetragonal phase at room temperature. The strong alkali volatility at elevated temperature often makes composition control difficult, and serious alkali loss can lead to the orthorhombic phase with deficient potassium and sodium. [234] The results indicated that high intensity ultrasonic irradiation accelerated the decomposition of carbonates and promoted the perovskite phase formation at substantially lower temperature. Once the alkali compositions were crystallized into the perovskite structure, they were much more stable. That is why the ceramic with improved density, solubility of Li, and electrical properties were obtained with KNN-LN powder treated with the high intensity ultrasonic irradiation.

The duration for the ultrasonic irradiation treatment of the raw materials powder was only 30 min, in contrast to the typical 24 h ball milling. This not only saved processing time, but also eliminated uncontrolled contamination arising during the intensive long time ball milling process.

4.3.7 Reaction kinetics

Having demonstrated the feasibility for the synthesis process assisted by the ultrasonic irradiation, it is necessary to further investigating the effect and the underlying mechanism of ultrasound on the reaction kinetics of 0.94KNN-0.06LN formation.

It is known that ultrasound's impact on solid state systems mostly arises from attrition. Suslick *et al.* reported that ultrasound creates cavitation implosion that causes surface damage increasing the effective surface area in inorganic solids such as ZrS_2, V_2O_5, TaS_2 and

MoO_3, significantly [106]. While some research has been performed to elucidate the kinetics of lead-free KNN-based ceramics formation [235], it is not known how the reactions are impacted by ultrasound. Several other external stimuli or perturbations, such as microwave [236] and high attrition milling [237], are also known to affect the reaction mechanisms. Ultrasound irradiation, in comparison, has strong merits as a non-invasive, easily controllable and applicable technique to material systems. Understanding the effects and the underlying mechanisms of ultrasonic treatments on the reactions for forming KNN-based ceramic is therefore a worthwhile endeavor.

In this work, with particle size analyses and X-ray photoelectron spectroscopy (XPS), we were able to gain an insight to the ultrasonic attrition effect in our KNN-LN ceramics. We further investigated 0.94KNN-0.06LN formation kinetics under ultrasound treatments through thermal analyses. It was further found that introduction of ultrasound at room temperature could selectively accelerate the elementary reaction steps in 0.94KNN-0.06LN formation, and lead to the change in the rate-determining step.

The reactions for forming alkali niobates can be generally denoted by the following reaction mechanism: [238]

$$2Nb_2O_5 + A_2CO_3 \rightarrow A_2Nb_4O_{11} + CO_2(g) \quad (4.1)$$

$$A_2Nb_4O_{11} + A_2CO_3 \rightarrow 4ANbO_3 + CO_2(g) \quad (4.2)$$

where A represents the alkali metal elements K, Na or Li. In equations (4.1) and (4.2), it is understandable that for KNN-based ceramic systems, the rate-limiting step is the decomposition of the carbonate. Ultrasound could interact with the starting solids at a length-scale and energy-scale, and thus was potentially capable of changing the relative rates of the two elementary reactions, due to locally high temperatures and large gradients of mechanical forces generated from acoustic cavitation. For probing the system on microscopic and

atomic levels, two sets of experiments were carried out, on pure and mixed powders of K_2CO_3, Na_2CO_3, Li_2CO_3 and Nb_2O_5 using a particle size analyzer and XPS. These studies were conducted to determine the physical and chemical properties of the starting materials after ultrasonic irradiation.

Table 4.2 lists the particle size distribution of the starting materials treated with different ultrasonic powers. The average size of K_2CO_3 aggregates was effectively decreased after ultrasound treatment. At an ultrasound power of 60 W, the magnitude of reduction in K_2CO_3 particle size was significant, by more than twenty times. The average size of Nb_2O_5 aggregates, which started out to be much smaller at 14.4 μm, was also reduced with increasing ultrasonic power to 8.0 μm at ultrasonic irradiation of 60 W. These observations are not surprising since ultrasound induced cavitation can create mechanical force fields that cause solid aggregates to undergo attrition. Interestingly, the average size of a blend of carbonates and Nb_2O_5 prior to any ultrasound treatment was measured to be closer in value to that of Nb_2O_5, instead of that of the much larger carbonates. This suggests that the carbonate could form loose aggregates which broke up more easily through interactions with Nb_2O_5 particles. Upon sonication at a power intensity of 52 W, a significant further reduction in particle size was observed. The sonicated mixture contains finer particles than either of the neat starting materials, at an average size of 1.9 μm, which are two orders of magnitude smaller than the starting K_2CO_3 particles.

Table 4.2. Particle size distribution of the starting materials treated with different ultrasonic power.

Compound	Ultrasonic power (W)	Average particle size (μm)
K_2CO_3	0	229.4
	7	196.4
	33	92.3
	44	16.4
	60	10.9
Nb_2O_5	0	14.4
	7	10.9
	22	9.4
	42	8.6
	52	8
Mixture	0	15.0
	5	2.5
	52	1.9

XPS spectra of the O 1s peak for the individual starting materials after sonication and the mixture before and after sonication are shown in Fig. 4.8. After sonication, the carbonyl oxygen of individual carbonates gave rise to photoelectrons from 1s orbital with binding energies higher than 530 eV. Nb_2O_5's 1s oxygen peak was at 529.8 eV after sonication. The binding energies of these 1s oxygen peaks of the individual reactants did not change from the values before the sonication. The XPS traces for typical K_2CO_3 and Nb_2O_5 samples before and after the sonication are shown in Fig. 4.9 and 4.10, respectively. It can be surmised that sonication did not substantially change the chemical structures of the alkali carbonates, as well as Nb_2O_5. However, it should be noted that the oxygen peak shifted to lower binding

energy just by simply mixing these reactants at room temperature, indicating interactions existed among the reactants in the mixture even without any heat treatment. By comparing the broaden shape of the oxygen peaks of the mixture before and after the sonication, it could be noted that the oxygen peaks corresponding to the position of the individual alkali carbonates and Nb_2O_5 at the higher binding energies, was substantially reduced after sonication, as shown in Fig. 4.8. This observation indicates that sonication could have enhanced the interactions among the alkali carbonates and Nb_2O_5 in the mixture, although no clear evidence to show sonication alone can induce carbonate decomposition at room temperature.

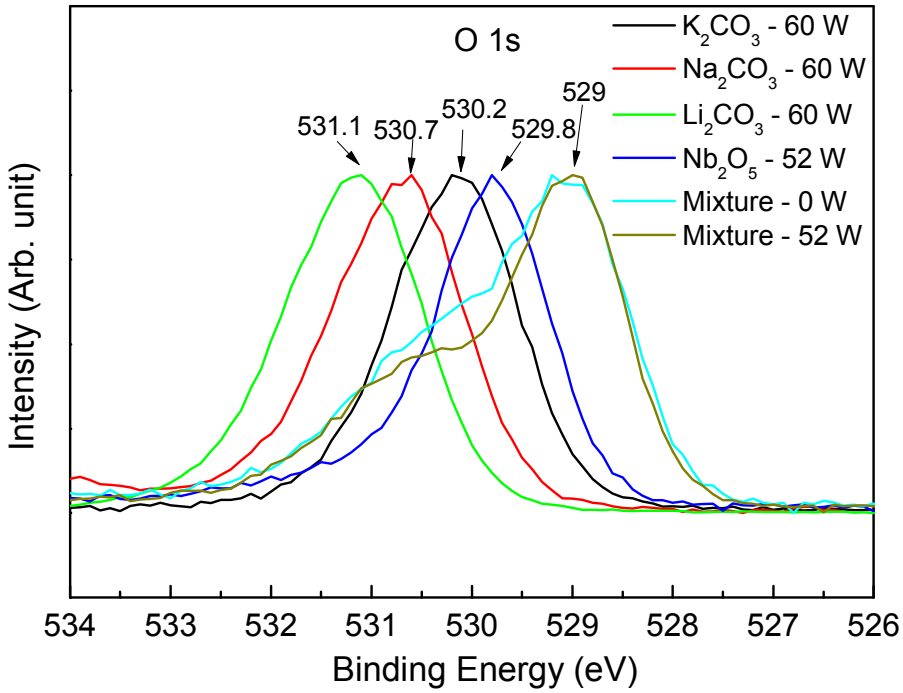

Fig. 4.8. XPS spectra of O 1s for starting materials, pure and in a mixture, treated with ultrasonic irradiation.

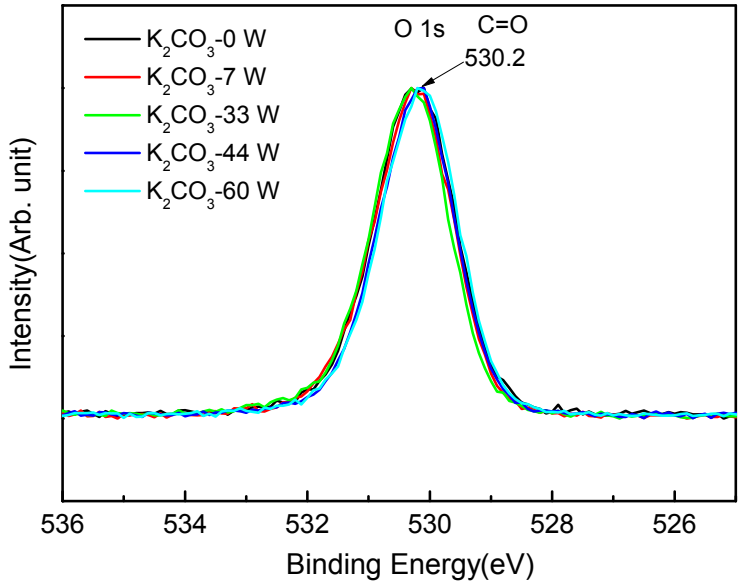

Fig. 4.9. XPS spectra of O 1s of K_2CO_3 starting materials treated with different ultrasonic irradiation power.

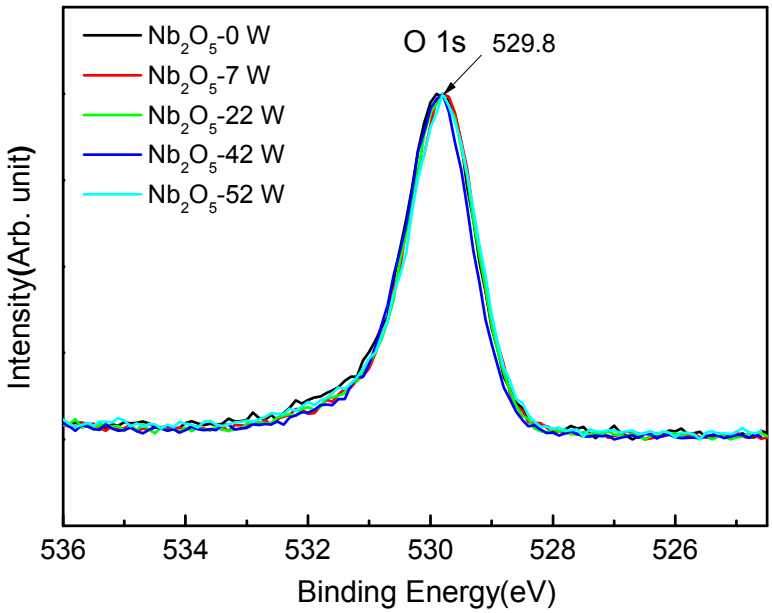

Fig. 4.10. XPS spectra of O 1s of Nb_2O_5 starting materials treated with different ultrasonic irradiation power.

For achieving effective thermal analyses for the system, we need to determine what happened at the different temperatures of interest, by conducting TGA experiments and collecting XRD spectra for samples directly cooled from the various temperatures following the same heating profile with the thermal analyses as performed. Fig. 4.11 shows the XRD patterns of the mixture powders that are pre-treated with ultrasonic irradiation of 52 W at room temperature, and then subjected to heating treatments at different temperatures (at a rate of 10 ^{o}C/min). It is reported that the decomposition of carbonates for KNN based ceramic typically starts from 400 ^{o}C to 800 ^{o}C; [235] XRD here did not detect any perovskite phase until 600 to 650 ^{o}C. Therefore, KNN-LN formation most likely happened from 650^{o}C to 800 ^{o}C range.

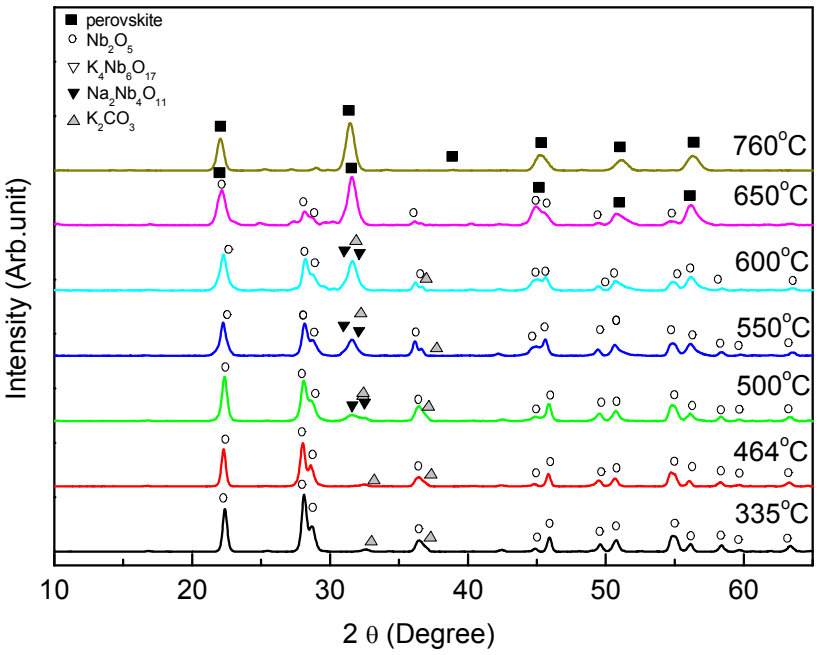

Fig. 4.11. XRD patterns for the mixture comprising of alkali carbonates and niobium oxide treated at 52W ultrasonic power after TGA –DSC at heating rate of 10 ^{o}C/min with different heating temperature.

Figure 4.12 presents the typical TGA-DSC curves of the mixture powders with the composition of 0.94KNN-0.06LN, pre-treated with ultrasonic irradiation, heated at different ramping rates. Different rates of 10, 20, 30, and 50 ^{o}C/min were experimentally performed in this work. The decomposition of various carbonates could happen over a broad temperature range below 800 ^{o}C. Large endothermic peaks are noted at the temperature ranging from 700 ^{o}C to 780 ^{o}C corresponding to different heating rates, which are labeled as the variable T_{1max}. T_{1max} corresponds to the maximum decomposition rate for the most persistent carbonates, of which the high decomposition temperature prevent the formation of the perovskite phase, as suggested by equations (4.1) and (4.2). Thus, these endothermic decompositions are always followed by large exothermic peaks taking place at the peak temperatures labeled as T_{2max}, which are attributed to perovskite phase formation. These peak positions as a function of heating rates can be used to estimate the activation energies of these two processes, according to Kissinger equations (4.3) and (4.4): [239]

$$\ln\left(\frac{{T_{1\max}}^2}{\Phi}\right) = \frac{E}{R{T_{1\max}}^2} + C_1 \qquad (4.3)$$

$$\ln\left(\frac{{T_{2\max}}^2}{\Phi}\right) = \frac{E}{R{T_{2\max}}^2} + C_1 \qquad (4.4)$$

where E is the activation energy of the reaction step in question, R is the gas constant (8.314 J/mol), and Φ is the heating rate.

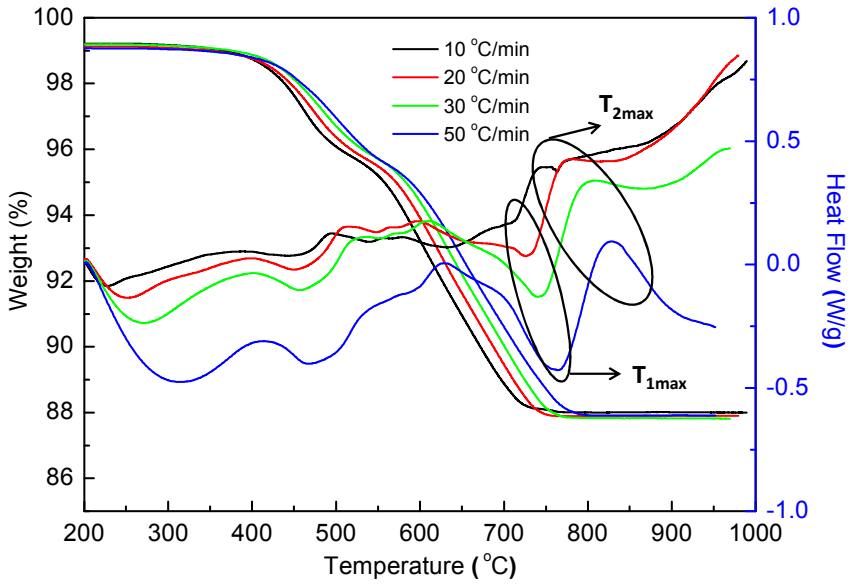

Fig. 4.12. Typical TGA-DSC curves of the mixture powders with the composition of 0.94KNN-0.06LN, pre-treated with ultrasonic irradiation, heated at different ramping rates.

The Kissinger equations are derived from the rate equation (4.5), which is used to describe most solid → solid + gas reactions: [239]

$$\frac{dx}{dt} = A(1-x)^n e^{-\frac{E}{RT}} \qquad (4.5)$$

where x is the fraction of reacted product and dx/dt is the reaction rate. One can carry out an analysis on the reaction order, n, for the elementary step of carbonate decomposition (described by equation 4.3, at $T = T_{1max}$). n can be extracted from the shape of the DSC peaks in Fig. 4.12 using the following relationship: [239]

$$n = 1.26S^{1/2} \qquad (4.6)$$

where S is the shape index determined from the DSC curves (refer to Fig. 4.13 for a typical example of determination of S). The reaction order calculated for the decomposition of carbonate mixtures treated at 5 W, 28 W and 52 W are 1.37, 0.84 and 0.63, respectively (based on a heating rate of 50 °C/min).

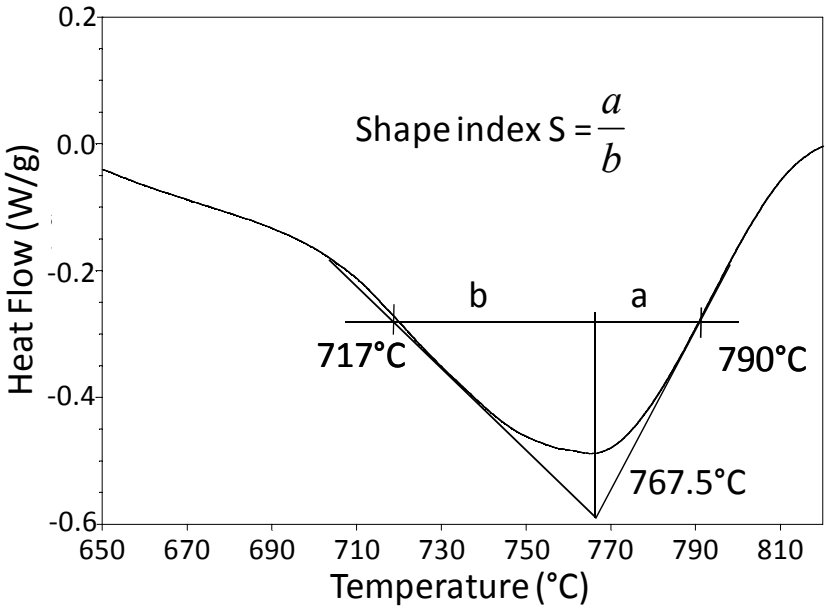

Fig. 4.13. Determination of shape index by measuring amount of asymmetry in an endothermic differential thermal analysis peak. [239]

Kissinger *et al.* [239] reported that the amount of undecomposed reactant at the peak temperature decreases when the reaction order decreases. This indicates that increasing the ultrasound power decreased the amount of undecomposed reactants. Since carbonate decomposition is known to be a diffusion-controlled process, [238] the analysis here suggests that ultrasound could promote the diffusion rate of the reactants, thereby could accelerate carbonate decomposition.

The Kissinger plots of ln (Φ/T_{max}^2) versus ($1000/T_{max}$) can be fitted with straight lines, for both the processes of carbonate decomposition and crystallization of perovskite phase, for all sonication conditions (Fig. 4.14). The activation energies for these two transitions, E_1 and E_2, could then be calculated from the slope. Fig. 4.14(a) clearly shows a reduction in activation energy E_1 with increasing the ultrasonic power, from 344 kJ mol^{-1} to 69.3 kJ mol^{-1}. Fig. 4.14(b) indicates the same trend applies for the crystallization of perovskite phase with

activation energies decreasing from 177 kJ mol^{-1} to 149 kJ mol^{-1}. The significant reduction in particle size and the enhanced interactions at the starting reactant mixture as shown in XPS results can increase the reaction interface and diffusion rates, and thereby can lower the activation energy and accelerate the solid state reaction.

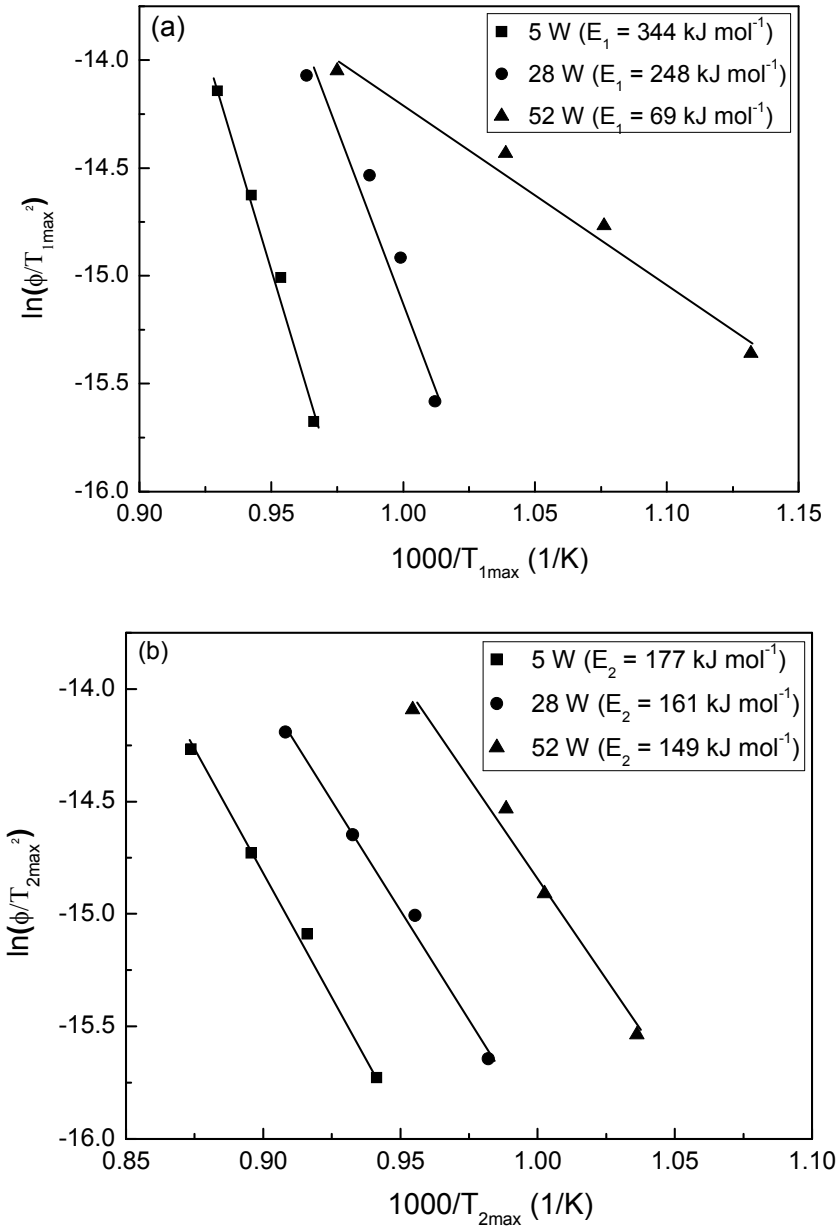

Fig. 4.14. Plot of ln (Φ/T_{max}^2) vs $1000/T_{max}$ according to the Kissinger equation for the mixture comprising of alkali carbonates and niobium oxide treated by ultrasonic irradiation of different powers, (a) ln (Φ/T_{1max}^2 vs $1000/T_{1max}$) and (b) ln (Φ/T_{2max}^2 vs $1000/T_{2max}$).

Interestingly, although both the activation energies for carbonate decomposition (E_1) and crystallization (E_2) decreased, the decrease in the former is one order of magnitude larger than in the latter. As a result, at higher powers of sonication (52 W in this study), the activation energy for carbonate decomposition became smaller than that for perovskite phase crystallization. Thus, the reaction barrier for carbonate decomposition becomes smaller than that for perovskite phase crystallization. While the initially higher magnitude of E_1 confirmed that carbonate decomposition constitutes a rate-limiting elementary step for KNN-LN formation (equation 4.1), the application of sonication significantly altered the reaction kinetics, such that the reaction of forming the perovskite phase was not rate-limited by the decomposition of the carbonates, and therefore the perovskite phase could be obtained at lower temperature. This discovery is especially important for KNN synthesis, where the loss of alkali ions prior to the formation of the perovskite phase is the main cause of the chemical non-stoichiometry and degraded performance properties in the resulting KNN ceramic. The fact that the ultrasonic irradiation at room temperature is able to directly impact reaction kinetics presents a simple and effective tool to control the reaction process and compound stoichiometry.

4.4 Conclusions

Lead-free piezoelectric ceramics of 0.94KNN-0.06LN were prepared by an ultrasonic irradiation method. The experimental results revealed that the ultrasonic irradiation facilitated the decomposition of the starting carbonates, promoted the perovskite phase formation and the desired coexistence of the orthorhombic and tetragonal phases, and improved ceramic density. The 0.94KNN-0.06LN ceramic samples with a relative density of 94 % were obtained after the ultrasonic irradiation processing under normal air sintering, which exhibited a piezoelectric constant of 184 pC/N. This study showed that ultrasonic irradiation was an effective method for producing high quality KNN-based lead-free ceramics with significantly reduced processing time. The effects of ultrasonic irradiation treatment at room temperature on the non-isothermal reaction kinetics for the formation of KNN-LN lead-free piezoelectric ceramics were further investigated. It was observed that sonication dramatically decreased the sizes of the starting material aggregates, and enhanced the interaction among the individual reactants even at room temperature. Through the quantitative analyses on the activation energies of decomposition of the starting alkali carbonates and formation of the resulting perovskite phase, it was found that the activation energies decreased with increasing ultrasonic power. More interestingly, the activation barrier for the decomposition of the carbonates was reduced to below the critical value for the crystallization of the perovskite phase with the high irradiation power, so that the reaction of forming the perovskite phase was not rate-limited by the decomposition of the carbonates. This finding highlights the significance of ultrasound utility in processing KNN-based ceramics with reduced synthesis temperature and improved control of stoichiometry. The strategy could be generally applied for impacting other compound synthesis involving multiple reaction steps by tailoring the kinetics of constituent reaction steps.

Chapter 5

Lead-free KNN-LN ceramic modified by polyvinylpyrrolidone (PVP) polymer

5.1 Introduction

Previously, in the Chapter 4, a novel method has been introduced to synthesize lead-free KNN-LN ceramics using fast and effective ultrasonic irradiation process and provided the in-depth analysis over the impact on the reaction kinetics of the studied ceramic system. However, there are still many other possible approaches that can contribute to compensate or suppress the alkali volatility during the high temperature heating process. In the reported studies, the addition of excess alkali compounds could help to maintain more alkali ions in the final ceramic. However, adding too much excess alkali ion components could cause other issues, which include the difficulty in precisely maintaining the chemical stoichiometry, poor repeatability, and exaggerated grain growth due to liquid phase sintering mechanism. [240] Therefore, it is desired to find alternative way to control the alkali ion volatility issue. Modifying the starting materials with polymeric additives could be potentially effective to suppress the alkali ion volatility issue, but this approach has not been paid adequate attention for lead-free piezoelectric ceramics.

It has been reported that polymers have been introduced to prepare ferroelectric thin films with perovskite structure using chemical solution method. Poly(ethylene glycol) (PEG) and polyvinylpyrrolidone (PVP) were used to produce perovskite $Pb(Zn_{1/3}Nb_{2/3})O_3$-$PbTiO_3$ (PZN-PT) [121] and $Pb(Mg_{1/3}Nb_{2/3})O_3$-$PbTiO_3$ (PMN-PT) [241] thin films by accelerating the perovskite phase crystallization at a lowered temperature while effectively suppressing

pyrochlore phase formation. Similar observations was reported for PEG polymers introduced in $Pb(Ni_{1/3}Nb_{2/3})O_3$-$PbTiO_3$ (PNN-PT) and (PMN-PT) ceramics prepared by solid state reaction. [125, 242] Recently in our group, lead-free KNN ceramic thin films prepared from polyvinylpyrrolidone (PVP)-modified precursor solution showed a significant improved effective d_{33} of 61 pm/V under substrate clamping. [128] Further studies revealed that the introduction of PVP in KNN thin film precursors promoted the crystallization of the KNN perovskite phase at lowered temperature effectively, which has substantially controlled the loss of alkali ions before the crystallization. However, there are limited research efforts at polymer-assisted ceramic processing reported on lead-free piezoelectric KNN-based bulk ceramics derived from solid state reaction.

The objectives in Chapter 5 are to explore the PVP effects on KNN-LN bulk ceramic prepared by solid state reaction method and further to clarify the mechanism for such effects in the ceramic system.

5.2 Experimental procedures

The material compositions studied were $0.94(K_{0.5}Na_{0.5})NbO_3 - 0.06LiNbO_3$ (0.94KNN-0.06LN). K_2CO_3 (99.5%), Na_2CO_3 (99.0%), Li_2CO_3 (99.999%), Nb_2O_5 (99.9%) (Alfa Aesar) were used as the starting raw materials, with 1 mol% of excess K, Na added. As the three carbonate powders were moisture sensitive, they were first dried prior to use to avoid compositional errors. The dried powders were then stoichiometrically weighed and mixed with 5 wt% of PVP of different molecular weights of 55 x 10^3, 360 x 10^3 and 1300 x 10^3 (abbreviated as PVP 55K, PVP 360K and PVP 1300K, respectively). These mixed powders were then ball-milled in ethanol for 24 h. The crushed powders derived from the dried slurry after the ball-milling were then treated for 30 min with ultrasonic irradiation using a direct-

immersion titanium horn. After the ultrasonication process, the slurry was dried and crushed again followed by calcinations at 850 ^{o}C for 5 h in an alumina crucible. After the calcined powders were ball milled for 4 h, and mixed with 4 wt% polyvinyl butyral (PVB) as a binder, they were uniaxially pressed into disks with a diameter of 10 mm and a thickness of about 1.3 mm.

The 0.94KNN-0.06LN disk samples were sintered at 1030 ^{o}C for 2 h in air. For comparison purpose, the 0.94KNN-0.06LN powder and ceramic without PVP addition were also prepared with the same procedures. The disk samples were carefully weighted before sintering (W1) and also after sintering (W2) (without taking into account the organic binder PVB in W1 and W2). The percentage of weight loss was calculated according to the equation below:

$$\% \text{ Weight loss} = [(W1 - W2)/ W1] \times 100 \qquad (5.1)$$

The ceramic samples with different molecular weights of PVP and without PVP are abbreviated as KNN-LN-55K, KNN-LN-360K, KNN-LN-1300K and KNN-LN respectively. All the samples were poled at 120 ^{o}C for 30 min under direct current field of 30 kV/cm for piezoelectric measurement.

5.3 Results and discussions

5.3.1 Crystalline structure of sintered ceramics

Figure 5.1 presents the X-ray diffraction (XRD) patterns of the 0.94KNN-0.06LN ceramic samples sintered at 1030 ^{o}C for 2 h. It can be seen from Fig. 5.1 that all the samples with and without PVP showed single-phase perovskite structure with an orthorhombic symmetry. The XRD peaks of orthorhombic phase are indexed in reference to those of $KNbO_3$ (JCPDS No. 32-0822).

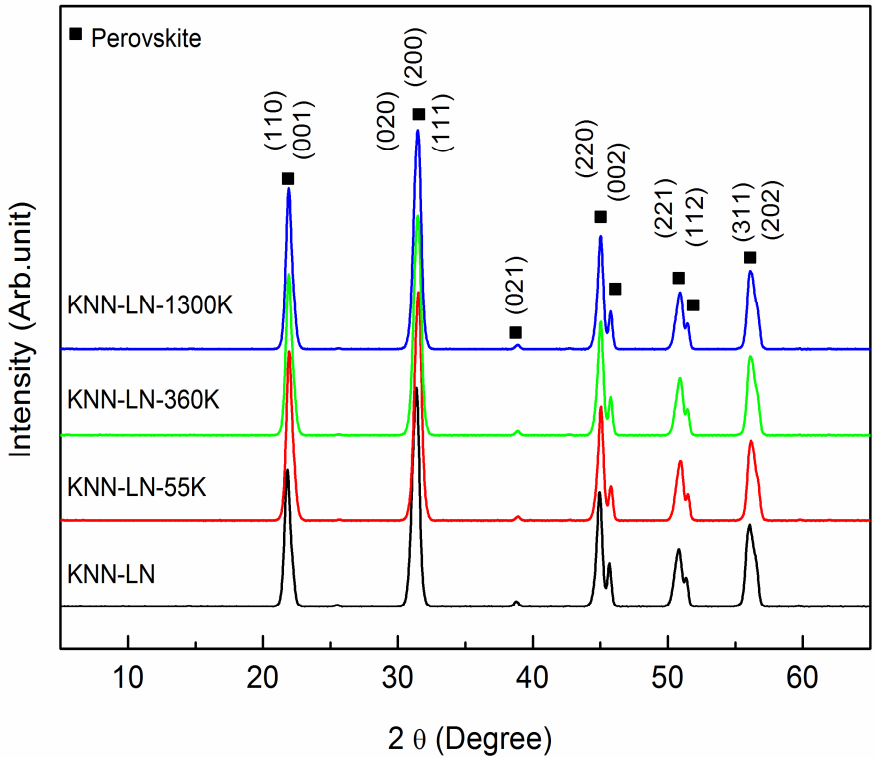

Fig. 5.1. X-Ray diffraction (XRD) patterns of the 0.94KNN-0.06LN ceramic samples with PVP of different molecular weights and without PVP, sintered at 1030 ^{o}C for 2 h.

5.3.2 Compositional analysis

Figure 5.2 shows the mole ratio between measured (K+Na) according to energy dispersive X-ray spectroscopy (EDX) and theoretically calculated (K+Na), together with weight loss according to equation (1) for the 0.94KNN-0.06LN ceramic samples without PVP and with PVP of different molecular weights. The mole ratio in Fig. 5.2 was calculated according to equation (2) below:

$$Mole\ ratio = \frac{(K+Na)(measured)}{(K+Na)(calculated)} \tag{5.2}$$

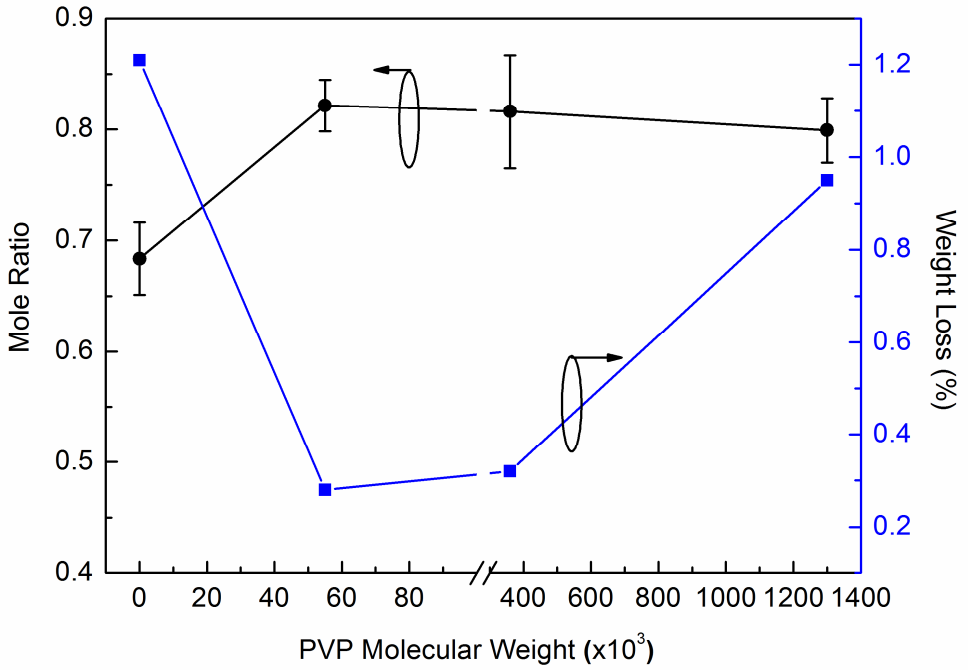

Fig. 5.2. Mole ratio between measured (K+Na) according to energy dispersive X-ray spectroscopy (EDX) and theoretically calculated (K+Na); and weight loss of 0.94KNN-0.06LN ceramic samples with PVP of different molecular weights and without PVP, sintered at 1030 ^{o}C for 2 h.

As shown in Fig. 5.2, there was significant deficiency of (K+Na) in the resulting 0.94KNN-0.06LN ceramic without PVP and the addition of PVP in the ceramic process substantially retained more (K+Na), although it was still below the theoretical amount. It is an established fact that maintaining the composition stoichiometry in KNN-LN system is very difficult due to strong alkali volatility at elevated temperature. Moreover, the formation of orthorhombic phase can lead to deficient potassium and sodium in the KNN-LN system as reported by Liu *et al.* [234] Orthorhombic phase was also observed in KNN-LN system as shown in Fig. 5.1. Although 1 mol% excess alkali components were added in our experiments to compensate the alkali ions losses, alkali deficiency was still there. On the other hand, adding too much excess alkali components could lead to stoichiometric imbalance in the final product and cause excessive grain growth due to liquid phase sintering [240]. In the meantime, it was observed that the weight loss during sintering as determined according to equation (5.1) was suppressed with PVP introduced with the starting reactants. It is *believe* that the effect in suppressing most of (K+Na) evaporation could happen during calcinations as our previous study showed that the major loss of alkaline components happened before the formation of perovskite phase [129]. By introducing PVP in the ceramic process, the starting reactants could form perovskite phase more completely during calcinations as compared to the 0.94KNN-0.06LN ceramic without PVP in which more unreacted reactants remained during the calcination. Thus further (K+Na) evaporation could continue to happen during the sintering. These results clearly indicate that (K+Na) alkali volatility was substantially suppressed by the addition of PVP polymer in the solid state reaction process for preparing the bulk KNN-LN ceramic.

The results in Fig. 5.2 also show that the molecular weight of PVP played an important role on the effect of suppressing alkali volatility. The least weight loss after sintering process

occurred at KNN-LN-55K ceramic, corresponding to PVP with a relatively smaller molecular weight of 55K. With the molecular weight of PVP increased to 360K and 1300K in KNN-LN-360K and KNN-LN-1300K samples, respectively, the weight loss kept increasing. Therefore, appropriate molecular weight of the polymer additives should be considered for effectively suppressing the volatilization of alkali metal ions and weight loss for the preparation of KNN-LN bulk ceramics.

5.3.3 Piezoelectric properties

The piezoelectric coefficient d_{33} and electromechanical coupling factor k_p of 0.94KNN-0.06LN ceramic samples with PVP of different molecular weights are given in Figure. 5.3. As shown in Fig. 5.3, d_{33} and k_p were increased from 109 pC/N and 0.31 in 0.94KNN-0.06LN sample without PVP to 140 pC/N and 0.35 respectively in KNN-LN-55K sample with PVP 55K. With the molecular weight of PVP increased to 360K and 1300K, KNN-LN-360K and KNN-LN-1300K samples still showed superior piezoelectric properties compared to 0.94KNN-0.06LN sample without PVP, but inferior to those of KNN-LN-55K. These results showed that improved piezoelectric properties were achieved in 0.94KNN-0.06LN ceramic with the addition of PVP 55K and with minimized alkali volatilization. However, with the PVP molecular weight further increased to 360K and PVP 1300K, the piezoelectric properties degraded again, which was consistent with the observed result of corresponding alkali loss. In Chapter 4, the piezoelectric coefficient of 184 pC/N was obtained from the 0.94KNN-0.06LN ceramic with an coexistence of orthorhombic and tetragonal phases was prepared using high ultrasonic power of 52 W. However, KNN-LN-55K sample with PVP 55K possessed piezoelectric coefficient of 140 pC/N, but with an orthorhombic phase, which was probably caused by different processing condition (24 h ball milling + ultrasonication).

We believe that, in the later processing scheme (24 hour ball milling followed by ultrasonication) can cause deviation in the resulting compositions, probably due to different volatilization of the alkali ions in intensively milled powder and possible contamination due to long time ball milling, which degrade the property.

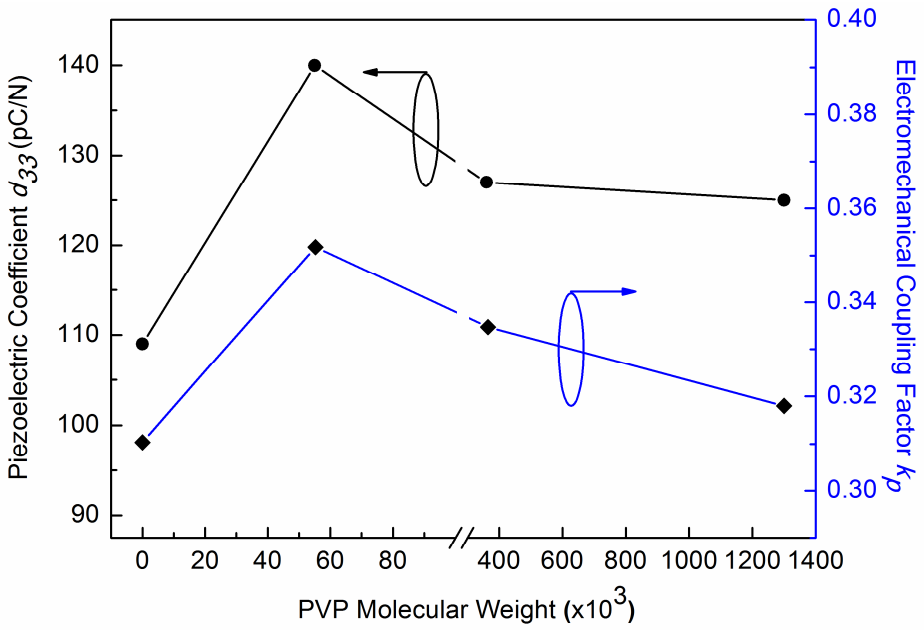

Fig. 5.3. Piezoelectric coefficient d_{33} and planar electromechanical coupling factor k_p of 0.94KNN-0.06LN ceramic samples with PVP of different molecular weights and without PVP, sintered at 1030 ^{o}C for 2 h.

5.3.4 FTIR spectroscopy

It is interesting to study the interaction between PVP and metal cations in the system. Figure 5.4 shows the Fourier transform infrared (FTIR) spectra of uncalcined 0.94KNN-0.06LN powders mixed with PVP of different molecular weights and pure PVP with molecular weight of 55K. The peak at 1658 cm^{-1} in pure PVP 55K is assigned to the C=O stretching band of PVP [243]. When PVP was added in KNN-LN system, regardless of the molecular weight, the C=O peak shifted to a higher wavenumber; 1663 cm^{-1} for KNN-LN-55K and 1661 cm^{-1} for both KNN-LN-360K and KNN-LN-1300K. The shifting of C=O peak

shows that there could be some interactions between metal ions and PVP. According to literature, there are two possible interactions between PVP and metal cations; the donation of electrons lone pair from the carbonyl oxygen to the metal cations or electron transfer from nitrogen in the five-membered nitrogen-containing ring to the metal cations. [244, 245] These two interactions may affect the polarizability of the oxygen in the C=O. It is known from Nakamoto [246] that a positive band shifts (shift to higher wavenumber) of amides' C=O stretching band in FTIR indicates electron transfer from nitrogen to the metal ions while a negative band shift (shift to lower wavenumber) indicates donation of electrons lone pair from the carbonyl oxygen to the metal ions. The shift of C=O peak to higher wavenumber in KNN-LN with different molecular weights of PVP as shown in Fig. 5.4 shows that metal cations are likely interact with nitrogen in PVP.

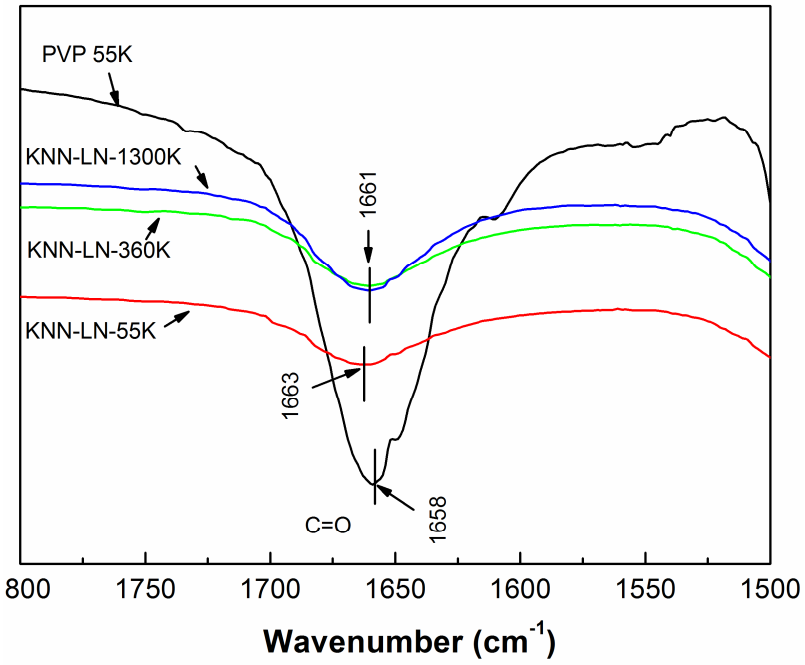

Fig. 5.4. Fourier transform infrared spectroscopy (FTIR) curves of uncalcined KNN-LN powders mixed with PVP of different molecular weights, in comparison with PVP 55K.

Although the shift of C=O stretching band in FTIR in Fig. 5.4 is evident, it is not very significant. XPS study was further conducted to examine the interactions of metal ions with PVP. Figure 5.5 presents the XPS spectra of N 1*s* in pure PVP 55K, uncalcined powders of KNN-LN-55K and KNN-LN. In KNN-LN, no N 1*s* peak is observed in binding energy range between 395 eV to 403 eV. In pure PVP 55K, only one peak is observed at 399 eV, which is corresponding to the nitrogen in the five-membered ring of PVP. [247] When PVP 55K was mixed with uncalcined KNN-LN, two peaks at 399 eV and 400.7 eV were observed. According to the literature, the smaller peak at the higher binding energy of N 1*s* is attributed to the $–N^{+}–$ species [248]. This suggested again that metal cations could have interacted with the nitrogen in PVP. This is reasonable because when positively charged K^{+} or Na^{+} is attracted to the nitrogen in PVP, electrons from the nitrogen could move towards K^{+} or Na^{+}, which could cause the decrease of electron density in nitrogen and hence increase its binding energy. [249] Referring to Fig. 5.2, the interaction between the nitrogen of PVP and the K/Na helped to retain K and Na in the KNN-LN bulk ceramic.

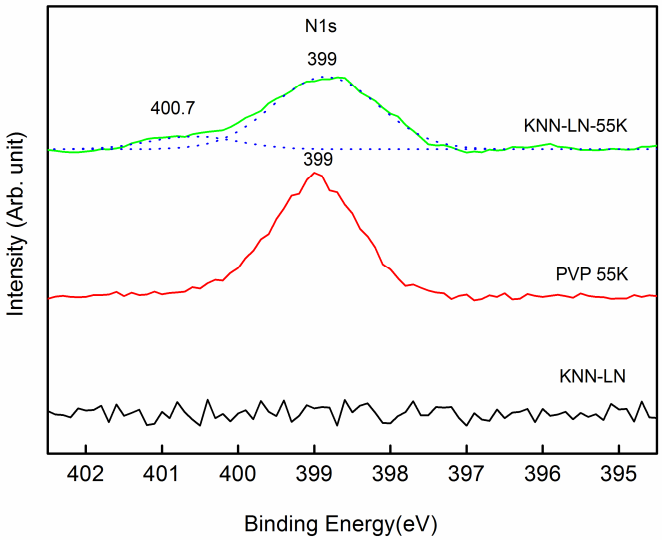

Fig. 5.5. XPS spectra of N 1*s* for uncalcined powders of PVP 55K, KNN-LN-55K and KNN-LN.

5.3.5 Phase structure for ceramic powders at intermediate temperature

Figure 5.6 shows the XRD patterns of 0.94KNN-0.06LN ceramic powders with PVP of different molecular weights calcined at 500 ^{o}C for 5 h. The decomposition of these carbonates started around 420 ^{o}C [229] and therefore all the samples were calcined at 500 ^{o}C to examine the formation of perovskite phase at the initial reaction stage. The formation of perovskite phase could depend on the decomposition of the starting alkali carbonates to oxides and their reaction with Nb_2O_5 oxides. By examining the XRD peaks of Nb_2O_5 in Fig. 5.6, it can be noted that the formation of perovskite phase was promoted most effectively with PVP 55K in KNN-LN-55K with the least residual Nb_2O_5, and the increase in the molecular weight from 55K to 1300K limited the effect of PVP on promoting the formation of the perovskite phase with at 500 ^{o}C. In order to understand high molecular weight 1300K has more unreacted Nb_2O_5, the thermal decompositions of PVP powders with different molecular weights were characterized and discussed in later section 5.3.7.

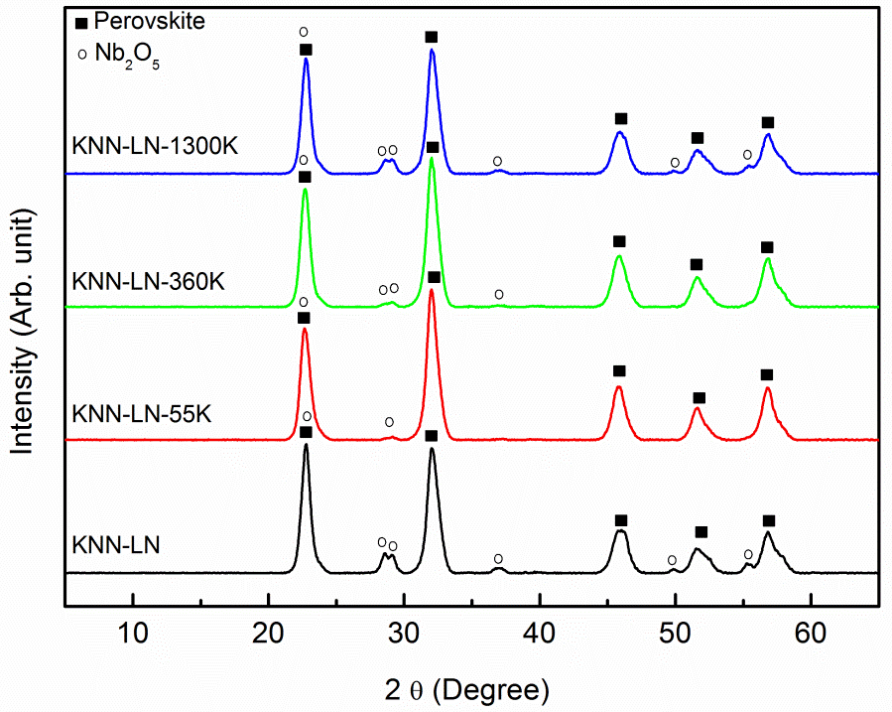

Fig. 5.6. X-ray diffraction (XRD) patterns of 0.94KNN-0.06LN powders with PVP of different molecular weights and without PVP, calcined at 500 ^{o}C for 5 h.

5.3.6 XPS analysis for ceramic powders at intermediate temperature

Figure 5.7 presents the XPS spectra of K 2*p* for 0.94KNN-0.06LN ceramic powders with PVP of different molecular weights calcined at 500 ^{o}C for 5 h. The samples calcined at 500 ^{o}C for all samples with and without PVP showed two peaks for K 2*p* with binding energies (BE) at 295 eV and 292 eV labeled as K $2p_{1/2}$' and K $2p_{3/2}$', respectively, which were attributed to K ions before crystallized into perovskite phase. Another two peaks for all the samples, labeled as K $2p_{1/2}$ and K $2p_{3/2}$, which shifted by ~ 1.5-1.6 eV toward lower binding energy (BE) from K $2p_{1/2}$' and K $2p_{3/2}$', respectively, were attributed to the ions in KNN perovskite phase. [129]

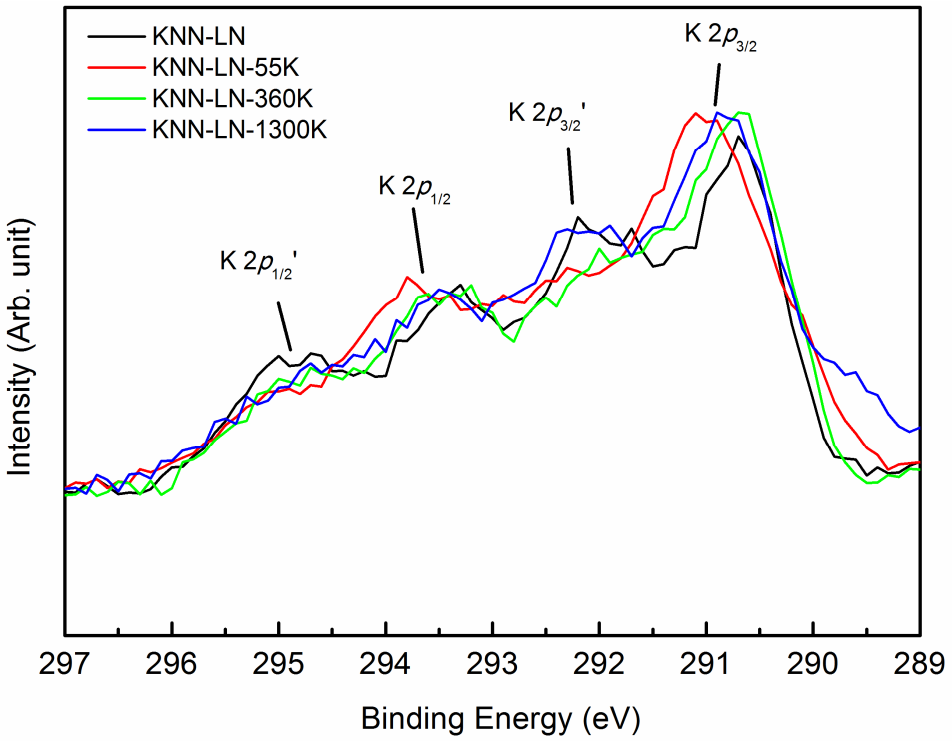

Fig. 5.7. XPS spectra of K 2*p* for 0.94KNN-0.06LN ceramic powders with PVP of different molecular weights and without PVP, calcined at 500 ^{o}C for 5 h.

As evident in Fig. 5.7, the peaks of K 2$p_{1/2}$' and K 2$p_{3/2}$', which were very intensive in KNN-LN samples, were almost eliminated in KNN-LN-55K. This XPS analysis result also strongly indicated the effect of PVP 55K for promoting the formation of perovskite structure in the solid state reaction for preparing the KNN-LN bulk ceramic. However, with the increase of molecular weight of PVP as in KNN-LN-360K and KNN-LN-1300K samples, more K ions could not form the perovskite structure at 500 ^{o}C. The XPS analyses on the amount of residual unreacted K ions are consistent with the XRD results on the residual unreacted Nb_2O_5 in all the samples without PVP and with PVP of different molecular weights.

Figure 5.8 shows the XPS spectra of O 1*s* for 0.94KNN-0.06LN ceramic powders with PVP of different molecular weights calcined at 500 ^{o}C for 5 h. Earlier (Chapter 4), we understood that the C=O of carbonates corresponds to 531 eV. By analyzing the peaks at 500 ^{o}C, it was noted that the carbonates decomposed faster for KNN-LN-55K samples as compared to KNN-LN-360K, KNN-LN-1300K and KNN-LN samples, as shown in Fig. 5.8.

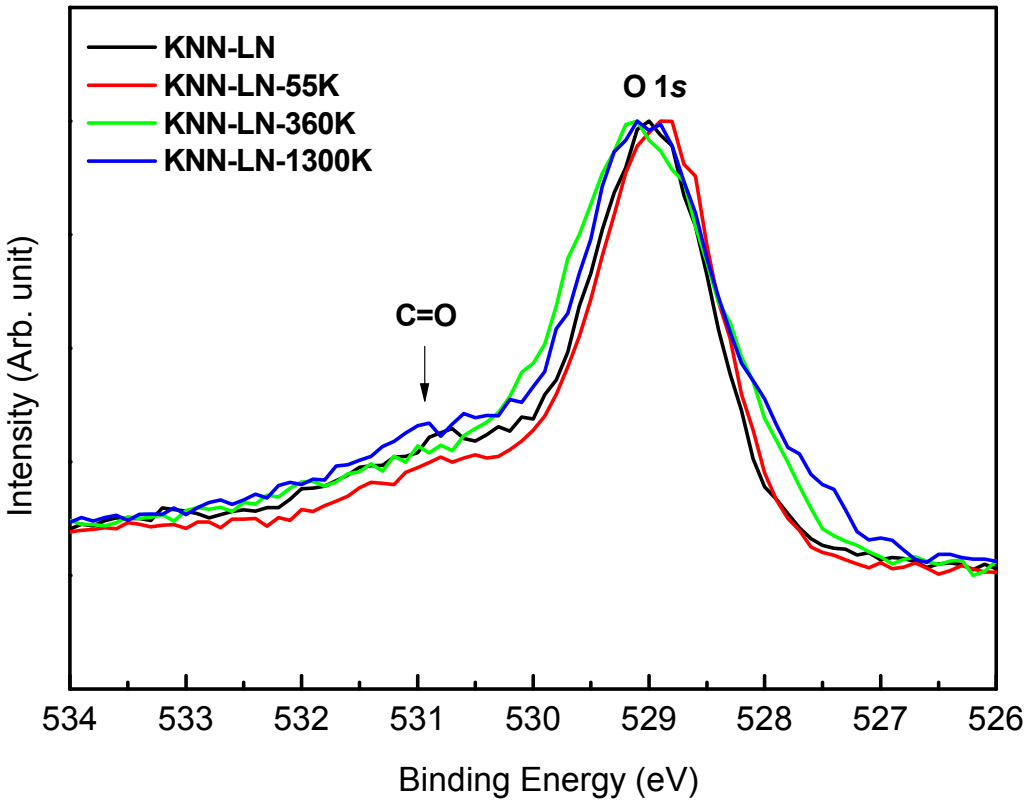

Fig. 5.8. XPS spectra of O 1*s* for 0.94KNN-0.06LN ceramic powders with PVP of different molecular weights and without PVP, calcined at 500 ^{o}C for 5 h.

Previously, our group observed that the alkali ions in KNN material were much more volatile during the preparation at the moderate temperature before the formation of the perovskite phase than after the formation at high temperature. Once the alkali ions entered the lattice of the perovskite structure, they would be much more stable. Therefore, we believe

retaining the alkali ions at the moderate temperature is critical to obtaining high quality KNN-LN ceramic. The results here showed the interactions between PVP and alkali ions, and further exhibited the role of introducing PVP for retaining the alkali composition in KNN-LN ceramic. Thus introducing PVP in the starting raw materials may be an effective method for obtaining stoichiometric KNN-LN and other ceramics with volatile alkali ions.

5.3.7 Thermal analysis

In order to understand other effects of the different molecular weight, the thermal decompositions of PVP powders with different molecular weights were characterized using TGA-DSC, as shown in Fig. 5.9.

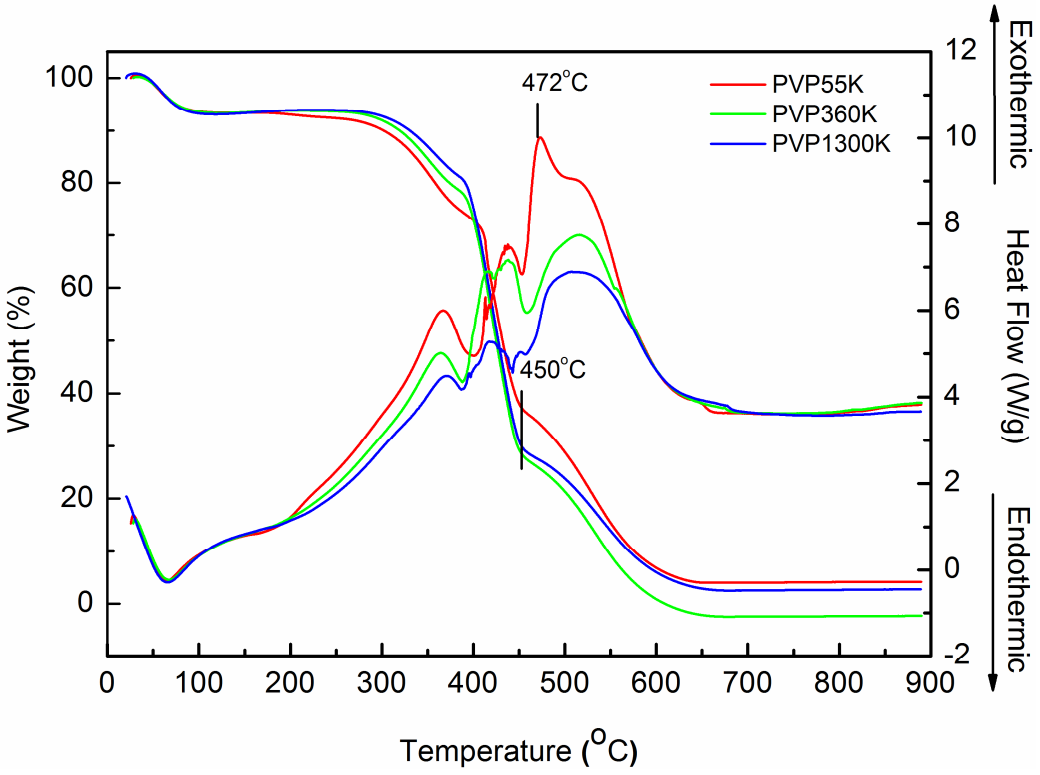

Fig. 5.9. Thermogravimetry-differential scanning calorimetry (TGA-DSC) curves for PVP powders of different molecular weights.

The TGA showed the decomposition of PVP 55K, PVP 360K, and PVP 1300K mainly happened between 300 to 550 ^{o}C. By observing the exothermic peaks, PVP 55K had more intense exothermic peak at 472 ^{o}C with much higher heat flow generated as compared to PVP 360K and PVP 1300K. According to literature, [250] thermal degradation of PVP is the depolymerization of polymeric main chain into monomer beginning from both ends of the linear polymer chain. For a given mass, PVP 55K has more chain ends than PVP with higher molecular weight. Therefore, PVP 55K could break more quickly than PVP 360K and PVP 1300K to facilitate the exothermic pyrolysis process. The short polymer chain means less endothermic decomposition and more heat generated. This intense heat generated between around 450 to 472 ^{o}C for PVP could act as in-situ heat source to promote the perovskite phase formation. It is believe that the more in-situ heat generated from PVP 55K would more significantly promote the decomposition of carbonates and enhance the perovskite phase formation as confirmed by the XRD and XPS results shown in Figs. 5.6, 5.7 and 5.8.

5.4 Conclusions

0.94KNN-0.06LN ceramics were prepared by solid state reaction process modified by introducing PVP in the starting raw materials. Experimental results revealed that the addition of PVP suppressed the loss of alkali ions and promoted the perovskite phase formation. Further characterization and analyses showed the chemical interaction between the metal cations and the PVP, particularly through the N in PVP. The heat generated by the decomposition of PVP could act as an in-situ heat source to promote the decomposition of the raw carbonates and the formation of the perovskite phase formation. With molecular weight ranging from 55K to 1300K, PVP with lower molecular weight exhibited more significant effect. Ceramic samples obtained with PVP 55K addition under normal air

sintering exhibited an improved piezoelectric constant d_{33} of 140 pC/N and a planar electromechanical coupling factor k_p of 0.35. This study showed that introducing PVP in the starting raw materials may be an effective method for obtaining stoichiometric KNN-LN and other ceramics with volatile alkali ions.

Chapter 6

Lead-free BCZT ceramics doped with LiF

6.1 Introduction

Having demonstrated the processing method for preparing the KNN-LN ceramics by means of using ultrasonic irradiation and PVP polymer as binding agent as described in Chapter 4 and 5, respectively it is of interest to further explore another promising lead-free BZT-BCT system with increased piezoelectric coefficient as mentioned earlier in the Chapter 1 through engineering the chemical composition. It is reported that 0.5BZT-0.5BCT ceramics system exhibits excellent piezoelectric properties of d_{33} (300-600 pC/N). However, the preparation of BZT-BCT system as reported is not so simple because it is necessary to ensure that single perovskite phase of BZT and BCT are achieved first prior to stoichiometric mixing for the composition of 50 mol% of BZT to 50 mol% of BCT. Long and tedious ceramic processing time is not cost effective to produce this ceramic in large scale. Moreover, BZT-BCT ceramics need high sintering temperatures of about 1450 ^{o}C-1540 ^{o}C [209, 216, 218, 251] which is not suitable for device integration because most metal electrodes cannot sustain such a high temperature in air. Therefore, based on Chapter 4 we would like to introduce ultrasonic irradiation approach to synthesize this promising lead-free piezoelectric material in a more effective route.

Also our previous studies in Chapter 4 for Li doped KNN system, the polymorphic phase transition (PPT) plays an crucial role in determining the piezoelectric and dielectric properties of the lead-free ceramics, and a PPT near room temperature would be beneficial to achieve enhanced electrical properties for the applications at room temperature. [72, 73] Therefore, it is interesting to develop a method to impact the PPT temperature.

Having considered that LiF is effective to lower the sintering temperature of some ceramics with perovskite structure, [252-254] in this Chapter 6, it is expected that $Ba_{0.85}Ca_{0.15}Zr_{0.1}Ti_{0.9}O_3$ (BCZT) lead-free ceramics with LiF can be prepared at low temperature. In this Chapter, BCZT lead-free ceramics with different amount of LiF doping are prepared by ultrasonic irradiation method. The polymorphic rhombohedral-tetragonal phase transition temperature is found shifted with the Li content. Lead-free BCZT piezoelectric ceramics with polymorphic phase transition near room temperature are obtained with processing temperature at 1350 ^{o}C.

6.2 Experimental procedures

The ceramic compositions studied were $Ba_{0.85}Ca_{0.15}Zr_{0.1}Ti_{0.9}O_3$ (BCZT) mixed with x mol of LiF (x = 0.00, 0.02, 0.04, 0.06, 0.10 and 0.15). $BaCO_3$ (99.95%), $BaZrO_3$ (99.0%), $CaCO_3$ (99.95%), TiO_2 (99.9%), and LiF (99.99%) were used as the starting raw materials. The raw material powders were stoichiometrically weighed and subsequently dispersed in ethanol in a beaker and treated for 30 min with ultrasonic irradiation using a direct-immersion titanium horn. After the ultrasonications were finished, the slurry was dried and crushed using agate mortar and pestle before it was calcined at 1350 ^{o}C for 5 h in an alumina crucible. The calcined powders were ball milled for 4 h by planetary milling. After the powders were ground and mixed with 4 wt% polyvinyl butyral (PVB) as a binder, they were uniaxially pressed into disks with a diameter of 10 mm and a thickness of about 1.4 mm.

The disk samples were sintered at 1350 ^{o}C and 1450 ^{o}C for 3 h in air. Bulk densities of the sintered disk samples were calculated from mass and geometrical dimension.

All samples were poled at 40 ^{o}C for 20 min under direct current field of 16 kV/cm for piezoelectric measurement.

6.3 Results and discussions

6.3.1 Crystalline structure of sintered ceramics

Figure 6.1(a) presents the X-ray diffraction (XRD) patterns of the BCZT ceramics with LiF sintered at 1450 ^{o}C for 3 h. All samples exhibited a single perovskite phase with no trace of any second phase detected, indicating that Ca^{2+}, Zr^{4+} and Li^{+} may diffuse completely into $BaTiO_3$ (BTO) lattices to form solid solutions in the studied composition range. The BCZT ceramics with LiF at room temperature were identified with diffraction patterns of a pseudocubic symmetry (PDF card #31-0174), which is a rhombohedral phase.

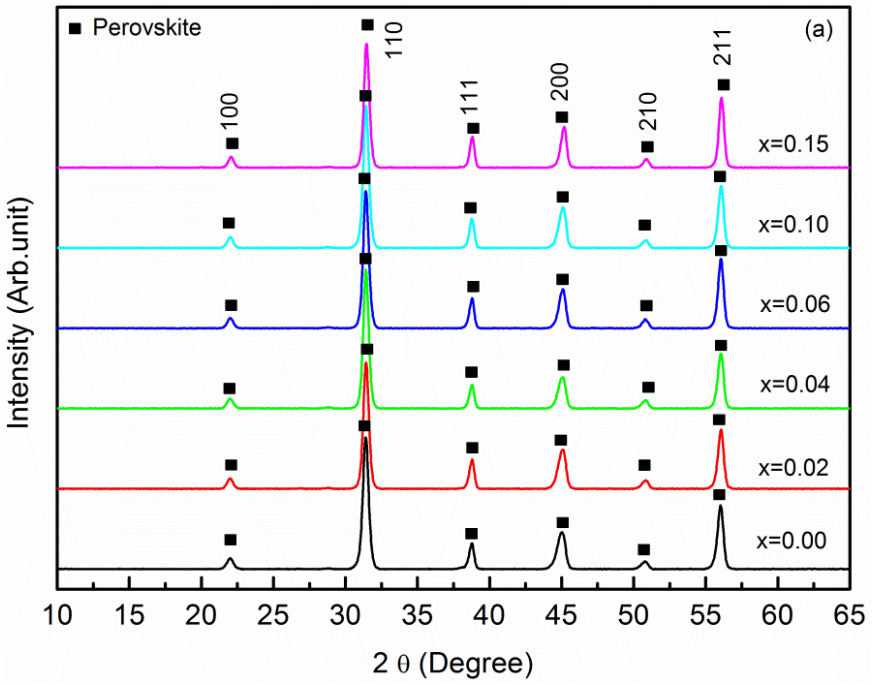

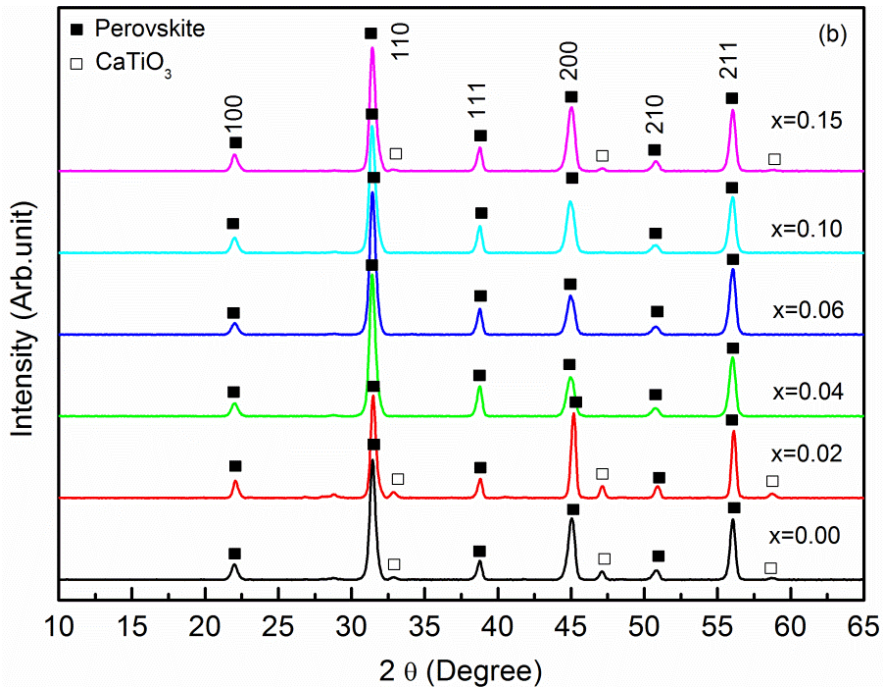

Fig. 6.1. X-ray diffraction (XRD) patterns of the BCZT-xLiF ceramics sintered at (a) 1450 ^{o}C and (b) 1350 ^{o}C for 3 h.

At lower temperature of 1350 ^{o}C, some traces of $CaTiO_3$ secondary phase was detected with Li content at $x \leq 0.02$ and $x \geq 0.15$, as shown in Figure 1(b) due to solubility limit of Ca into BTO. Henning *et al.* [255] also reported that the maximum solubility limit of Ca into BTO was about 18 mol% at 1400 ^{o}C and lower solubility of Ca into BTO at lower sintering temperature. However, with the LiF content in the range of $0.02 < x < 0.15$, the secondary phase of $CaTiO_3$ was suppressed and single perovskite phase could be achieved at lower sintering temperature of 1350 ^{o}C. This implies that there is an optimum amount of LiF in order to suppress the $CaTiO_3$ secondary phase at the relatively low temperature. Adding low amount of LiF at $x \leq 0.02$ is not sufficient to suppress the secondary phase of $CaTiO_3$.

6.3.2 Relative density and weight loss of sintered ceramics

Figure 6.2 shows the variation of the relative density and weight loss of BCZT ceramics with LiF sintered at different temperatures for 3 h. The relative density was calculated based on theoretical density of BCZT-xLiF, which was determined from the theoretical density of BCZT (5.687 g/cm^3) [209] and that of LiF (2.635 g/cm^3). From Fig. 6.2, it is observed that the BCZT ceramic had a higher density value at the lower sintering temperature of 1350 °C regardless of LiF doping, in comparison with that at higher temperature of 1450 °C. From our previous studies in Chapter 4, ceramic density can be improved by using ultrasonic processing method as used here. Therefore, it is believe that the ultrasonic processing method reduced the sintering temperature to 1350 ^{o}C from 1450 ^{o}C compared to other reported BCZT ceramics of similar compositions. [216] However, at the same sintering temperature, either 1350 °C or 1450 °C, the relative density of the resulting BCZT ceramic decreased with increasing the amount of LiF.

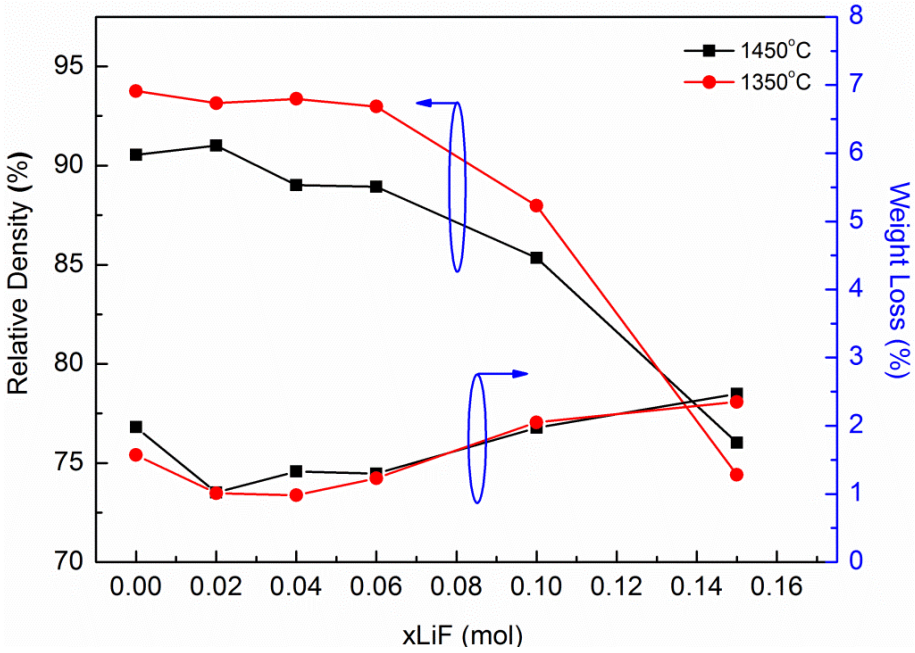

Fig. 6.2. Relative density and weight loss of the BCZT-xLiF ceramics sintered at different temperatures for 3 h.

The disk samples were carefully weighed before sintering (W1) and after sintering (W2) (not counting the organic binder PVB in W1 and W2), and the percentage of weight loss was calculated according to the equation below:

$$\% \text{ Weight loss} = [(W1 - W2)/ W1] \times 100 \qquad (6.1)$$

As shown in Fig. 6.2, the ceramic samples experienced weight loss due to composition volatility. From our energy dispersive X-ray spectroscopy (EDX) results, the stoichiometry of combined Ba and Ca was found to be around 0.94. This deviates from the ideal stoichiometry of 1. P. Babilo *et al.* [256] have also reported that Ba volatility exists in $BaZr_{0.8}Y_{0.2}O_{3-x}$ during sintering. The weight loss during sintering at 1350 ^{o}C decreased with increasing the amount of LiF up to x = 0.04, but the weight loss increased with further increasing LiF. Low weight loss was achieved with small amount of LiF (x = 0.02 to 0.04) doping at the lowered sintering temperature of 1350 ^{o}C. Our results showed that low doping

of LiF content could help to suppress the A-site volatility of Ba by forming solid state solution in BCZT system. However, the volatilization of Ba and LiF could possibly happen together during sintering at high doping level of LiF. Therefore there is an optimum amount of LiF addition with the minimized weight loss.

6.3.3 Electrical properties

Figure 6.3 presents the dielectric constant and loss tangent for the BCZT ceramics with LiF sintered at 1350 ^{o}C and 1450 ^{o}C at 1 kHz. High dielectric constants between 2775 to 3060 and low dielectric losses below 0.02 were observed with $x \leq 0.06$ for all the samples. However, dielectric constant decreased and dielectric loss increased with further increasing LiF content. The decrease in dielectric constant may be attributed from the decreased bulk density as shown in Fig. 6.2 with more LiF added into the ceramics.

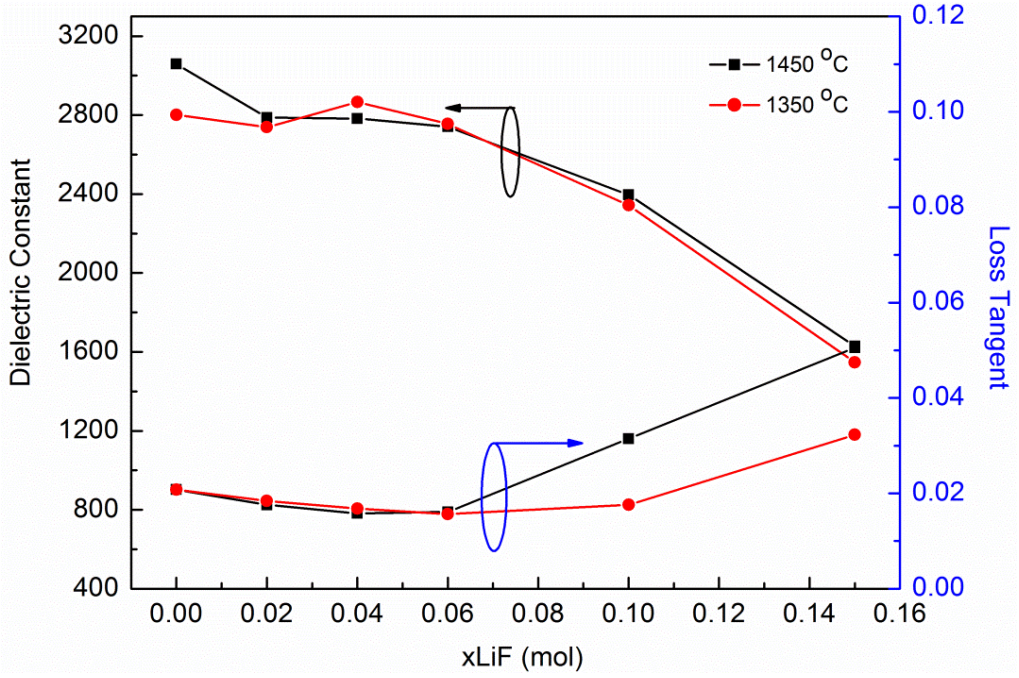

Fig. 6.3. Dielectric constant and loss tangent the BCZT-xLiF ceramics sintered at different temperatures for 3 h at 1 kHz.

Figure 6.4 shows the temperature dependences of dielectric constant for the BCZT ceramics with different LiF contents sintered at 1350 ^{o}C for 3 h at 1 kHz. For BCZT without LiF doping, the dielectric maxima occurred around 93 °C, corresponding to the Curie temperature (at $T_{(T-C)}$, T_c), while another dielectric anomaly observed at 55 °C which was associated with the rhombohedral-tetragonal polymorphic phase transition ($T_{(R-T)}$). It was observed that the phase transition $T_{(R-T)}$ peak shifted toward room temperature below 40 °C with increasing Li content, whereas T_c had no obvious change up to x = 0.10. However, further increase of Li content to x = 0.15 resulted in the large increase of T_c to 107 ^{o}C. These results indicate that the phase transitions of $T_{(R-T)}$ can be shifted nearer to room temperature while a relatively high Curie temperature can be maintained or even further elevated with the doping of Li content in BCZT system. The phase transition peak shift also implies that at least certain amount of Li^{+} entered the lattice of the perovskite structure.

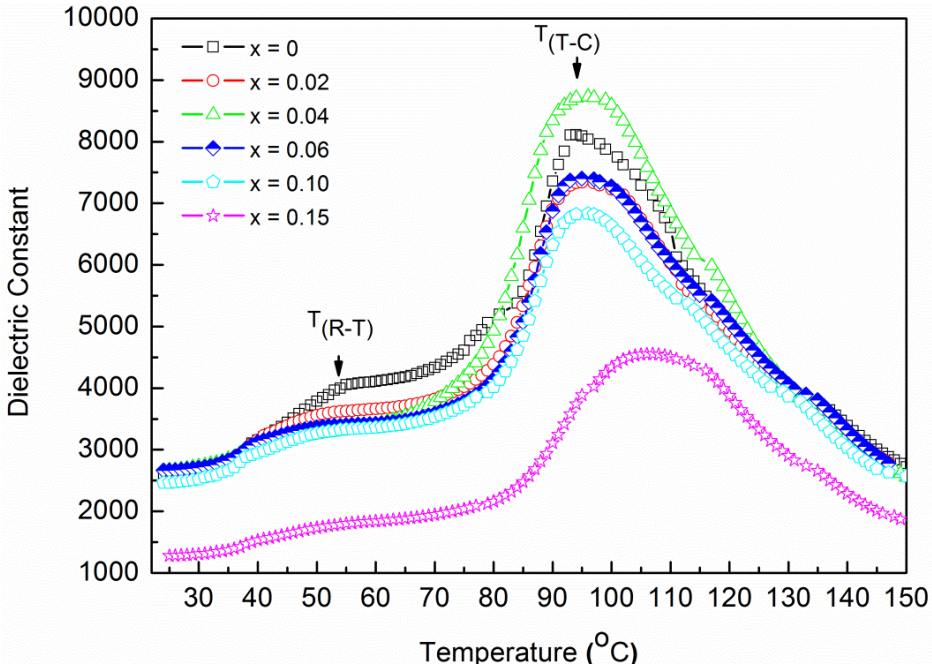

Fig. 6.4. Temperature dependence of dielectric constant for the BCZT-xLiF ceramics sintered at 1350 ^{o}C for 3 h at 1 kHz.

Figure 6.5 shows the piezoelectric coefficient d_{33} and planar electromechanical factor k_p for the BCZT ceramics with different LiF contents sintered at 1350 ^{o}C and 1450 ^{o}C, respectively. As shown in Fig. 6.5, although for the samples without LiF doping, d_{33} and k_p were slightly larger when sintered at 1450 ^{o}C than 1350 ^{o}C, the samples with small amount of LiF doping (x = 0.02 to 0.1) showed larger d_{33} and k_p when sintered at the lower temperature of 1350 ^{o}C than 1450 ^{o}C. The maximum values of piezoelectric d_{33} of 380 pC/N and k_p of 39.5 % were obtained at x = 0.06, at the lower sintering temperature of 1350 ^{o}C. The LiF-doped BCZT ceramics sintered at 1350 ^{o}C exhibited improved piezoelectric properties than some other reported BCZT ceramics of similar compositions and derived from similar oxide mixing route but sintered at 1450 ^{o}C, in which the d_{33} was 328 pC/N and k_p was 37.6 % after the optimization. [216]

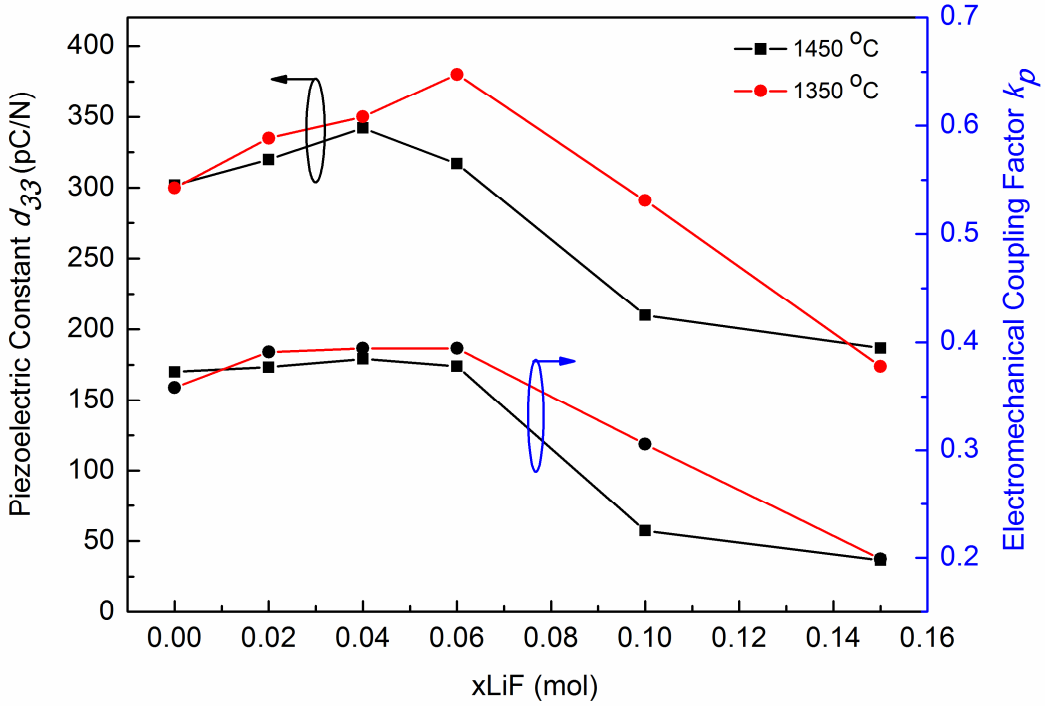

Fig. 6.5. Piezoelectric coefficient d_{33} and planar electromechanical factor k_p for the BCZT-xLiF ceramics sintered at different temperatures for 3 h.

The improved piezoelectric properties as observed in the LiF-doped BCZT ceramics may be ascribed to the shift of the polymorphic phase transition temperature (PPT, $T_{(R-T)}$) from 55 °C for the pure BCZT to near room temperature below 40 ^{o}C, as shown in Fig. 6.4. Improved piezoelectric properties were also obtained in KNN system as a result of shifting the phase transition temperature towards room temperature. It should also be noted that the ultrasonic processing method as used here not only significantly reduced the processing time in contrast to the conventional long and tedious ball milling process, but also prevented uncontrolled contamination arising during the intensive long-time ball-milling process.

Figure 6.6 shows the hysteresis loops of polarization versus electric field for the BCZT ceramics with different LiF doping amounts sintered at 1350 ^{o}C for 3 h. Well saturated hysteresis loops were clearly observed in all the samples. The remnant polarization P_r and coercive field E_c of the BCZT sample without LiF were found to be 7.9 μC/cm^2 and 3.1 kV/cm, respectively. A small amount of LiF doping up to x = 0.10 had a very minor effect on the polarization and coercive field, but the P_r values decreased from 7.9 μC/cm^2 to 5.6 μC/cm^2 if x = 0.15. The decrease in P_r and increase in E_c with large amount of LiF (x = 0.15) are attributed to the decrease in ceramic density as shown in Fig. 6.2. Therefore, although more LiF doping could shift the phase transition point closer to the room temperature, optimal doping of LiF has to be determined after considering many other factors that strongly affect the material performance properties, including the ceramic density.

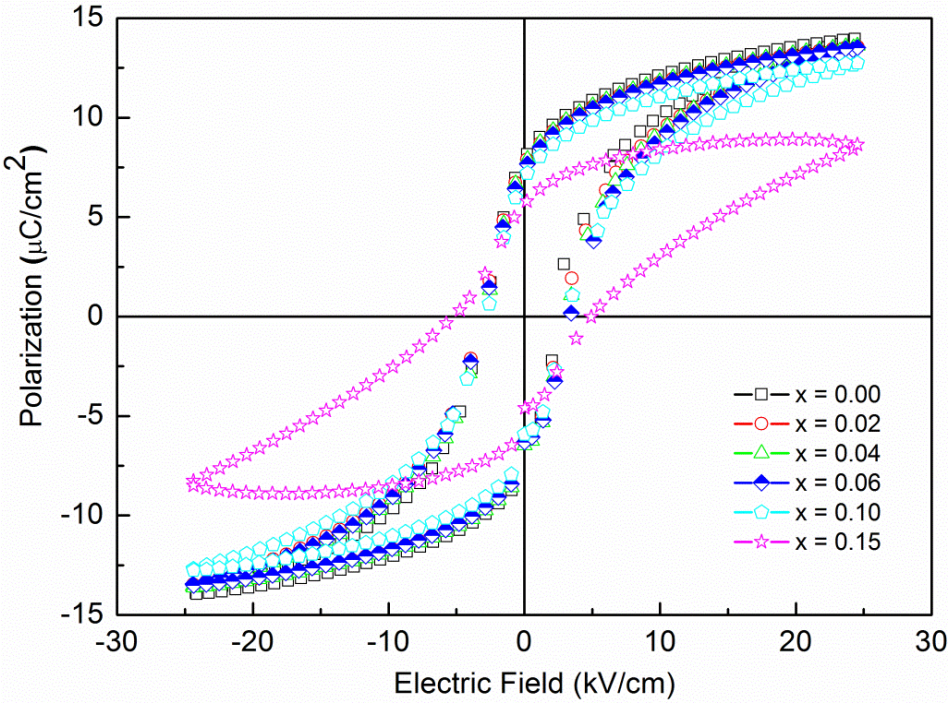

Fig. 6.6. Polarization versus electric field for the BCZT-xLiF ceramics sintered at 1350 ^{o}C for 3 h.

6.4 Conclusions

In summary, $Ba_{0.85}Ca_{0.15}Zr_{0.1}Ti_{0.9}O_3$ (BCZT) lead-free piezoelectric ceramics with different amounts of LiF (BCZT-xLiF) were prepared, and the effects of the LiF doping on the polymorphic phase transition behavior and the electrical properties of the resulting ceramic were investigated. The experimental results showed that the polymorphic rhombohedral-tetragonal phase transition temperature was found shifted towards room temperature with the Li doping. An enhanced piezoelectric coefficient of d_{33} = 380 pC/N and a planar electromechanical factor of k_p = 39.5% were obtained at room temperature in the BCZT-xLiF sample with x = 0.06. The study showed that BCZT piezoelectric ceramic with improved performance properties at room temperature can be achieved by shifting the polymorphic phase transition point nearer room temperature through the addition of LiF.

Chapter 7

Lead-free KNN-LN ceramics doped with BCZT

7.1 Introduction

In our previous studies in Chapter 6 in BCZT-xLiF system, the polymorphic phase transition plays an important role in determining the dielectric and piezoelectric performance properties of the lead-free piezoelectric ceramics, and a polymorphic phase transition near room temperature would be beneficial to achieve enhanced electrical properties for applications at room temperature. We have successfully produced BCZT-xLiF at lower sintering temperature of 1350 ^{o}C using mixed oxide route prepared by fast and cost effective ultrasonic irradiation method with large piezoelectric coefficient d_{33} of 300-380 pC/N and T_c of 93-107 ^{o}C. Although the Curie temperature is improved by doping LiF into the BCZT system, it is still not sufficient for many device applications at high temperature region. Therefore, the material with both high T_c and d_{33} are desired for those applications.

Chapter 7 is focused on $0.96(K_{0.5}Na_{0.5})NbO_3$-$0.04LiNbO_3$ (0.96KNN-0.04LN) ceramics, which possess high T_c ~ 456 ^{o}C. However, 0.96KNN-0.04LN ceramics typically suffer from smaller d_{33} value ~ 100 - 140 pC/N, and it is difficult to obtain stable larger piezoelectric coefficient with normal ceramic processing condition. To enhance the d_{33} values of the KNN-LN based system, BCZT as prepared previously in Chapter 6 are used here as the dopant to explore the potential MPB region. So far conventional techniques that require excessive long hours of ball milling (~ 24 h) are mostly adopted for preparing lead-free piezoelectric ceramic powder. Our efforts as mentioned in the previous chapters show that preparing lead-free 0.94KNN-0.06LN and BCZT-xLiF piezoelectric ceramic using ultrasonic irradiation is a

very effective method for producing high quality lead-free piezoelectric ceramics with improved density at a significantly reduced processing time.

In this Chapter, we have synthesized (1-x)(0.96KNN-0.04LN)-xBCZT ceramics by employing ultrasonic irradiation method, and studied their structure, dielectric, ferroelectric, and piezoelectric properties systematically.

7.2 Experimental procedures

Lead-free ceramics of 1-x[0.96($K_{0.5}Na_{0.5}$)NbO_3-0.04$LiNbO_3$]-x($Ba_{0.85}Ca_{0.15}$)($Zr_{0.1}Ti_{0.9}$)O_3: (1-x)(0.96KNN-0.04LN)-xBCZT with x = 0, 0.001, 0.002, 0.004, 0.008, 0.010, 0.013, and 0.015, were prepared using $BaCO_3$ (99.95%), $BaZrO_3$ (99%), $CaCO_3$ (99.95%), TiO_2 (99.9%), (K_2CO_3 (99.5%), Na_2CO_3 (99.0%), Li_2CO_3 (99.999%), Nb_2O_5 (99.9%) as the starting raw materials. The raw starting materials of BCZT ceramics were first stoichiometrically weighed and ultrasonicated for 30 min with ultrasonic irradiation using a direct-immersion titanium horn (Sonics VCX500, 20 kHz, 500 W, Sonics & Materials Inc., Newtown, CT) followed by drying and calcination at 1350 ^oC in air ambient for 5 h. The calcined powders were further ball-milled in ethanol medium for 4 h. The wet-slurry was further dried and the dried powders were sieved into micron size uniform powder. As the K_2CO_3, Na_2CO_3 and Li_2CO_3 powders were moisture sensitive, they were first dried prior to use to avoid compositional errors. The dried carbonate powders, Nb_2O_5 and BCZT calcined powders were then stoichiometrically weighed and subsequently dispersed in ethanol and treated for 30 min with ultrasonic irradiation. After the ultrasonication process the slurry was dried and crushed again followed by calcination at 850 ^oC for 5 h using an alumina crucible. The calcined powders were ball milled for 4 h. Polyvinyl butyral (PVB) of 4 wt% was mixed as the binder with the calcined powders, and the powders were then pressed into disk form

with a diameter of 10 mm and a thickness of ~1.8 mm by applying an uniaxial pressure of 200 MPa.

The green body disk samples were sintered at 1050 ^{o}C for 2 h in air. The bulk density of the sintered ceramic disks was determined by weighing and measuring regular geometrical dimensions. All the reflection peaks were indexed and the lattice parameters were determined and refined (using least squares method) using software program 'PowdMult'. [257]

For electrical characterization, a thin layer of silver paste was coated on both sides of the polished specimens. All the samples were poled at 120 ^{o}C for 30 min under direct current field of 32 kV/cm and were left over at room temperature for 24 h before measuring their piezoelectric constant, d_{33} The dielectric properties were measured at 100 kHz in the temperature range from 25 °C to 500 °C with an impedance analyzer. The ferroelectric properties were studied in the temperature range from 25 °C to 140 °C at a frequency of 10 Hz.

7.3 Results and discussions

7.3.1 Crystalline structure of sintered ceramics

Figure 7.1(a) presents the XRD patterns of the (1-x)(0.96KNN-0.04LN)-xBCZT ($0 \leq x \leq 0.015$) ceramics sintered at 1050 ^{o}C for 2 h. Single-phase perovskite structure was observed in all the studied samples.

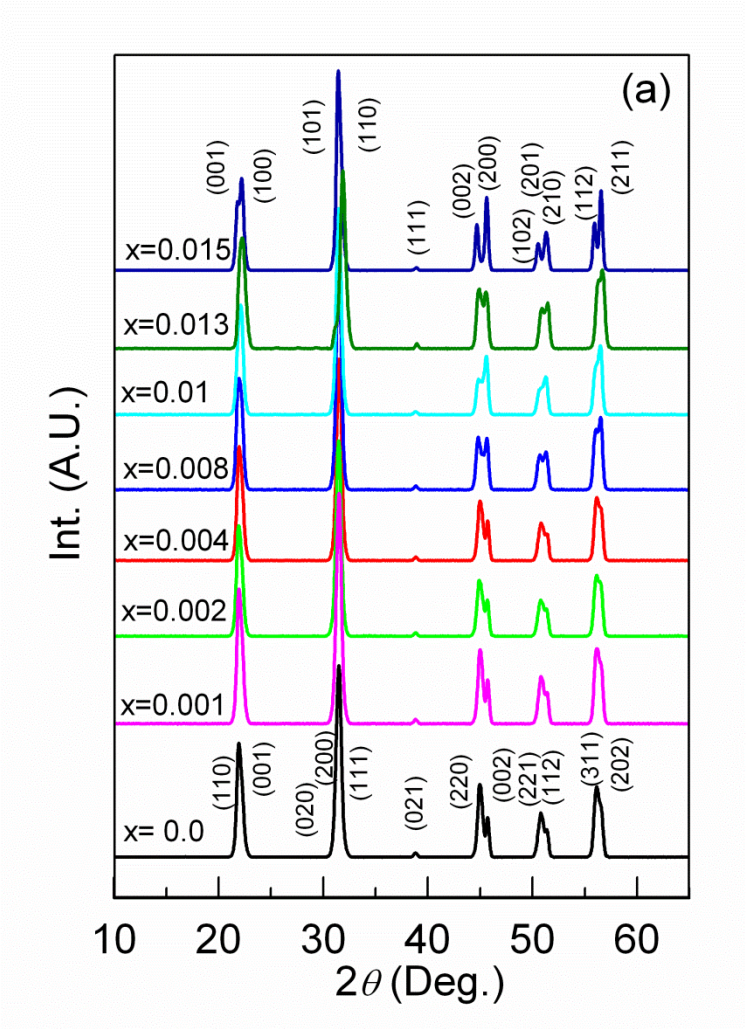

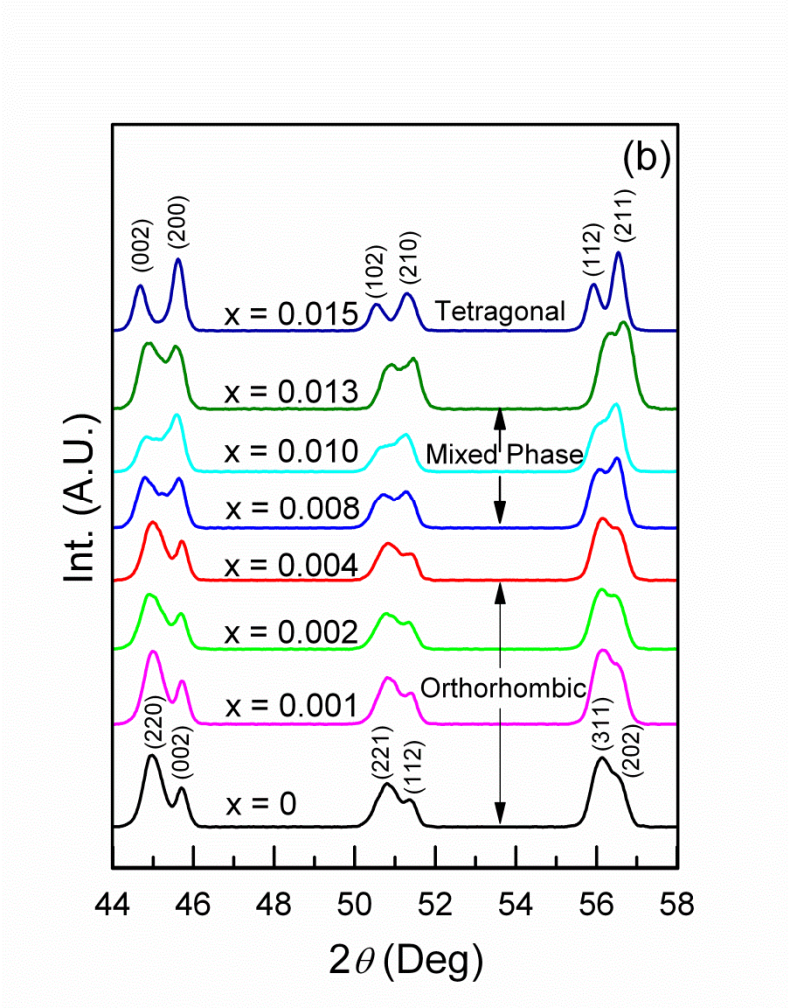

Fig. 7.1. XRD patterns of the (1-x)(0.96KNN-0.04LN)-xBCZT ceramics with different BCZT contents and sintered at 1050 ^{o}C for 2 h, (a) 2θ in the range of 10^{o} - 65^{o}, and (b) 2θ in the range of 44^{o} - 58^{o}.

The XRD peaks of orthorhombic and tetragonal phase are indexed in reference to $KNbO_3$ (JCPDS No. 32-0822) and (JCPDS No. 71-0945), respectively. The zoomed XRD patterns of the ceramics in the range of 2θ from 44^{o} to 58^{o} are shown in Fig. 7.1(b). Interestingly, with the increase of BCZT content from x = 0.001 to 0.015, the orthorhombic peaks of (220), (002), (221), (112), (311), and (202) transform to tetragonal peaks of (002), (200), (102), (201), (210), (112), and (211), which illustrates the gradual transformation from

orthorhombic to tetragonal phase. Therefore, it can be concluded that the orthorhombic phase symmetry exists in the (1-x)(0.96KNN-0.04LN)-xBCZT ceramics for x ≤0.008 and it turns into a tetragonal symmetry for x ≥ 0.013. The MPB of orthorhombic and tetragonal phases coexist in the ceramics system for (0.008 ≤ x ≤ 0.013). Using the software program 'PowdMult' [257] the lattice parameters of the (1-x)(0.96KNN-0.04LN)-xBCZT ceramics as a function of the BCZT contents were analyzed, with the results as shown in Fig. 7.2. The mixed phase of orthorhombic and tetragonal structures is identified for the (1-x)(0.96KNN-0.04LN)-xBCZT (0.008 ≤ x ≤ 0.013) ceramics.

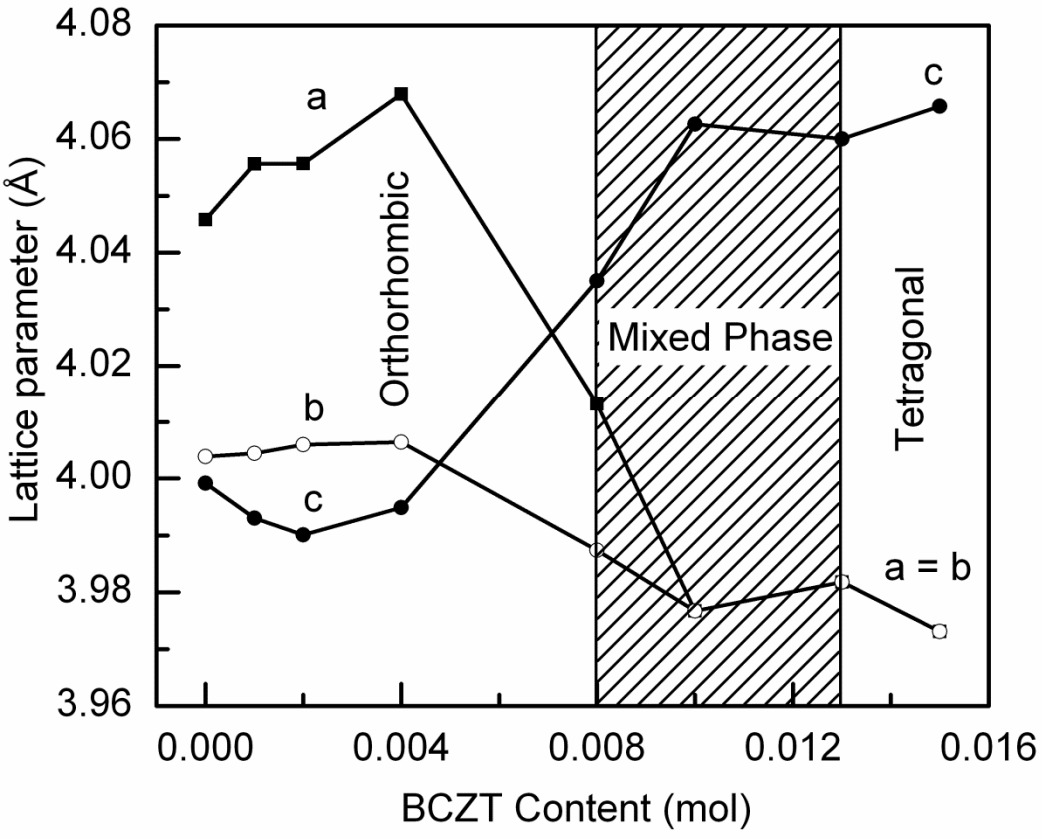

Fig. 7.2. Lattice parameters of the (1-x)(0.96KNN-0.04LN)-xBCZT ceramic samples with different BCZT contents sintered at 1050 ^{o}C for 2 h.

7.3.2 Relative density of sintered ceramics

Figure 7.3 shows the variation of the relative density of (1-x)(0.96KNN-0.04LN)-xBCZT ceramics with different BCZT contents and sintered at 1050 ^{o}C for 2 h. As shown, the relative density of the studied ceramics increases with increasing BCZT content and reaches the maximum value of 94% for the value of x = 0.010. This is attributed to the grain size modification in the solid solutions with the coexistence of the two phases. Among the studied ceramic compositions, the lowest porosity and the least average grain size corresponding to the phase co-existence are observed for x = 0.010, as shown in the micrographs (inset in Fig. 7.3).

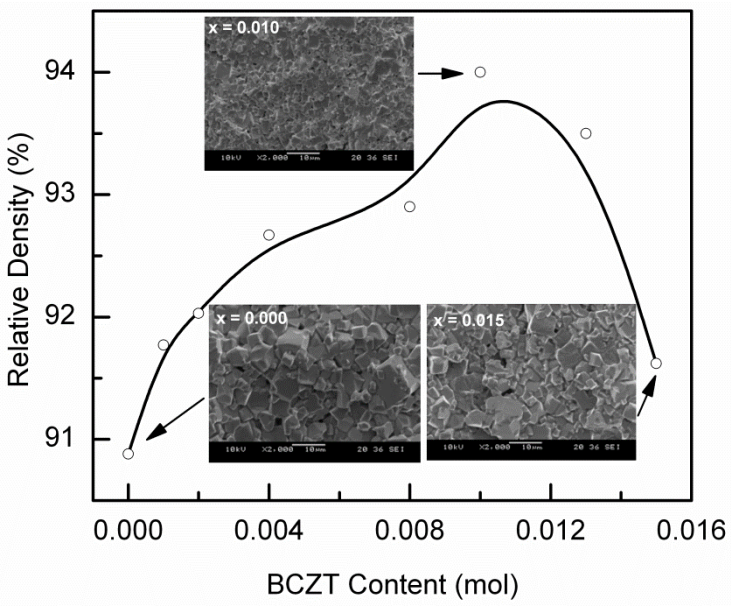

Fig. 7.3. Relative density of (1-x)(0.96KNN-0.04LN)-xBCZT ceramic samples with different BCZT contents sintered at 1050 ^{o}C for 2 h. Inset shows the surface morphology of the ceramics with x = 0.0, 0.010 and 0.015.

7.3.3 Electrical properties

Temperature dependent dielectric spectroscopy was performed to investigate the polymorphic phase transition temperature in our (1-x)(0.96KNN-0.04LN)-xBCZT ceramics.

Figure 7.4 depicts dielectric constant of the (1-x)(0.96KNN-0.04LN)-xBCZT ceramics measured at 100 kHz in the temperature range from 25 °C to 500 °C. The (1-x)(0.96KNN-0.04LN)-xBCZT ceramics with ($x \leq 0.013$) show two prominent dielectric peaks, which correspond to the PPT temperature of orthorhombic-tetragonal ($T_{(O-T)}$) and the tetragonal-cubic ($T_{(T-C)}$) (i.e. T_c) structures. In pure KNLN ceramic, the dielectric maxima corresponding to T_c occurs at 456 °C and the dielectric peak corresponding to the polymorphic phase transition ($T_{(O-T)}$) appears at 116 °C. The insets (a) and (b) of Fig. 7.4 depict that the T_c value decreases linearly and the phase transition $T_{(O-T)}$ peaks shifts towards room temperature with the increase of the BCZT content in the studied system. With increasing the BCZT content, both of these phase transition temperatures shift to lower temperatures. When $x \geq 0.015$, the orthorhombic–tetragonal phase transition disappears and the material becomes a solely tetragonal structure with a Curie temperature of ~ 420 ^{o}C. These results are consistent with the XRD analysis.

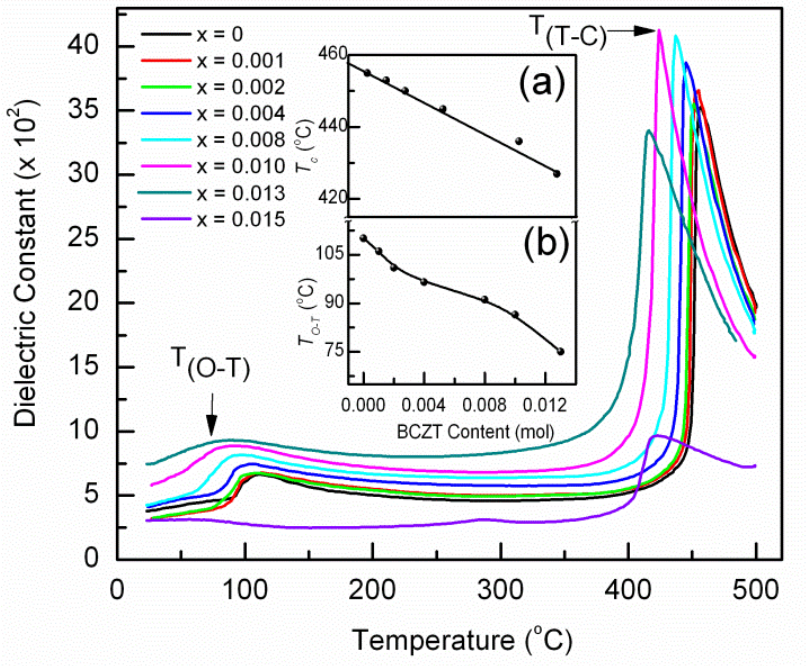

Fig. 7.4. Temperature dependence of the dielectric constant of (1-x)(0.96KNN-0.04LN)-xBCZT ceramics measured at 100 kHz. The insets (a) and (b) of Fig 7.4 show the relationship between the Curie temperature (T_c) and the orthorhombic-tetragonal ($T_{(O-T)}$) transition temperature respectively with the content of BCZT (x) for (1-x)(0.96KNN-0.04LN)-xBCZT ceramics.

Figure 7.5 presents the electric polarization versus electric field (P-E) hysteresis loops at room temperature for (1-x)(0.96KNN-0.04LN)-xBCZT ceramics with x = 0, 0.010, 0.013, 0.015. The P-E hysteresis loops obtained when x= 0.010 and 0.013 show the highly saturated ferroelectric polarization in nature. However, the P-E loops for ceramics with x = 0 and 0.015, exhibit leaky nature, with smaller remnant polarization. The leakage may attribute to the low ceramic density in those samples as shown in Fig. 7.3, although the role of the composition variation cannot be completely ruled out. The values of remnant polarization $2P_r$ and coercive field $2E_c$ of the 0.99(0.96KNN-0.04LN)-0.01BCZT ceramic sample are found to be 21.8 μC/cm^2 and 35 kV/cm respectively. The inset in Fig. 7.5 depicts the P_r versus temperature for the (1-x)(0.96KNN-0.04LN)-xBCZT ceramics with x = 0, 0.010, 0.013, and 0.015. The observed anomalies in the temperature dependant polarization due to $T_{(O-T)}$ phase transition are generally consistent with the previously observed dielectric anomalies (Fig. 7.4). With the appropriate addition of BCZT, enhanced polarization near room temperature is obtained in the (1-x)(0.96KNN-0.04LN)-xBCZT system by shifting the polymorphic phase transition ($T_{(O-T)}$) towards room temperature.

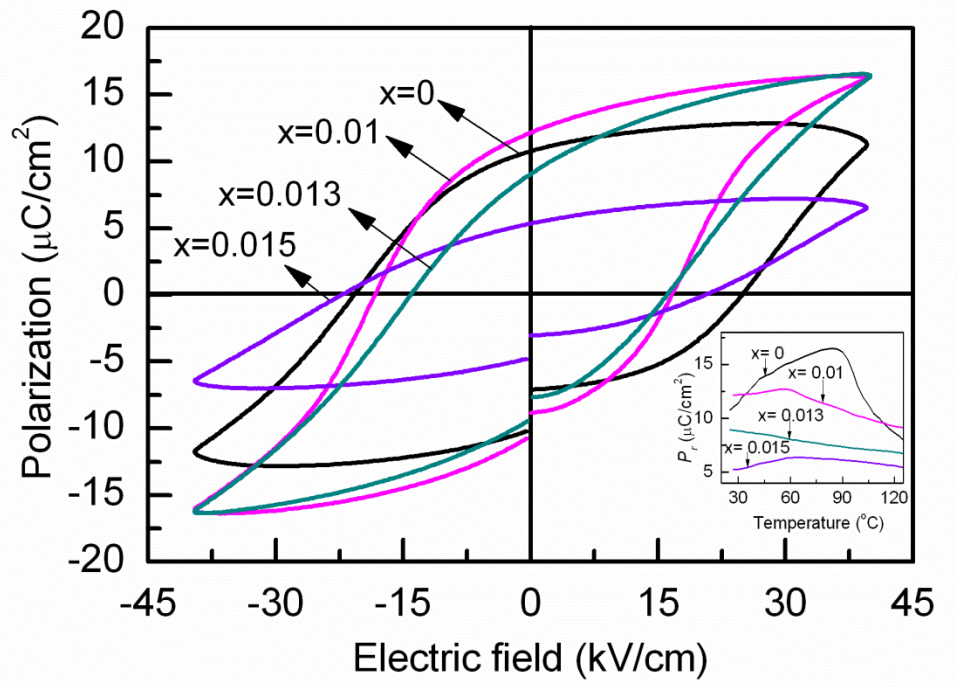

Fig. 7.5. Polarization vs. electric field hysteresis loops measured at different temperatures for (1-x)(0.96KNN-0.04LN)-xBCZT ceramics with different BCZT contents. Inset depicts the temperature dependant P_r.

Figure 7.6 gives the piezoelectric coefficient d_{33} and planar electromechanical coupling factor (k_p) of the (1-x)(0.96KNN-0.04LN)-xBCZT ceramics with different BCZT contents. The maximum values of d_{33} is 180 pC/N and of k_p is 34 % for the ceramic sample with x = 0.01. The values of d_{33} and k_p start to decrease with further increase of the BCZT contents. The improved piezoelectric properties at room temperature as observed in the (0.96KNN-0.04LN)-BCZT ceramics may be attributed to the coexistence of the orthorhombic and tetragonal phases. It is well known for lead-based perovskite ceramics, such as PZT, enhanced piezoelectric properties can be found near MPB region. [4]

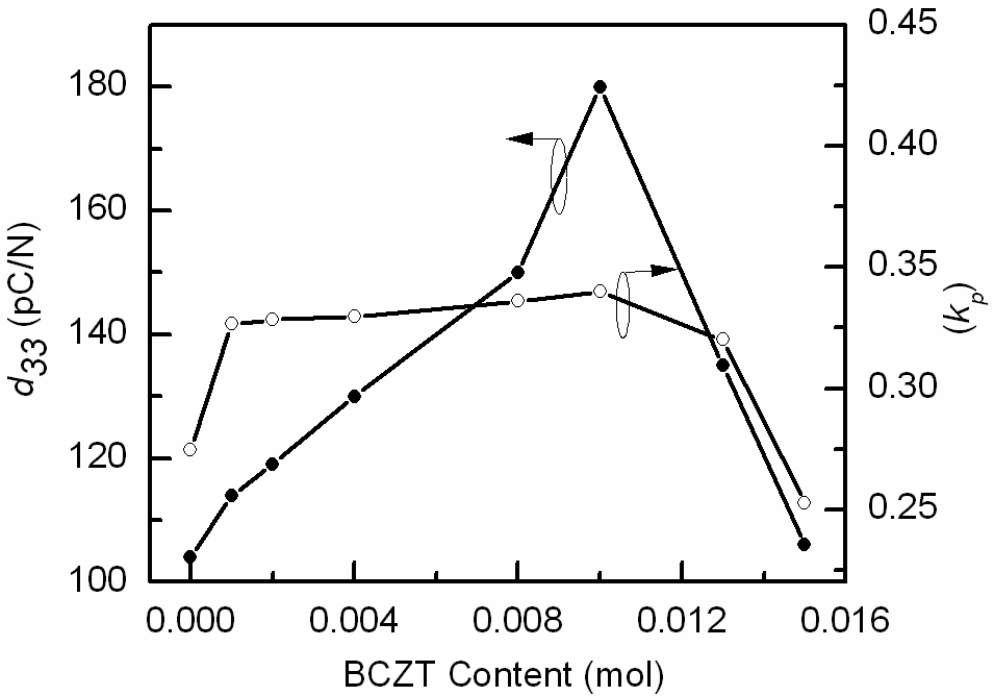

Fig. 7.6. Variation of piezoelectric properties of (1-x)(0.96KNN-0.04LN)-xBCZT ceramic with different BCZT contents.

The PZT ceramics near the MPB contain both the rhombohedral and tetragonal phases and thus have more possible polarization states, which consequently lead to the significant enhancement in the piezoelectric properties. Similarly, the improved piezoelectric properties as observed in the (1-x)(0.96KNN-0.04LN)-xBCZT ceramics with x = 0.010 could result from the more possible polarization states due to the coexistence of the orthorhombic and tetragonal phases.

Although (1-x)(0.96KNN-0.04LN)-xBCZT ceramics with x = 0.010 has slightly lower value of d_{33} as compared to 0.94KNN-0.06LN (another MPB composition) mentioned in Chapter 4, this is the first reported value of this new MPB system of KNN-LN-BCZT, and required further process optimization.

7.4 Conclusions

Lead free piezoelectric ceramics (1-x)(0.96KNN-0.04LN)-xBCZT ($0 \leq x \leq 0.015$) are prepared by a solid state reaction process, assisted by ultrasonic irradiation. The coexistence of orthorhombic and tetragonal phases is identified in the range of $0.008 \leq x \leq 0.013$. The polymorphic orthorhombic-tetragonal phase transition temperature shifts towards room temperature with the increase of the BCZT concentration. For the 0.99(0.96KNN-0.04LN)-0.01BCZT (x = 0.01) ceramic with T_c = 425 °C, improved polarization and enhanced piezoelectric properties, with d_{33} = 180 pC/N and k_p = 0.34, are obtained at room temperature due to the shift of the orthorhombic-tetragonal phase transition towards room temperature. These results indicate that (1-x)(0.96KNN-0.04LN)-xBCZT (x = 0.01) ceramic is a promising lead-free piezoelectric material.

Chapter 8

Conclusions and future work

8.1 Conclusions

This thesis has systematically investigated the synthesis, structure and properties of lead-free piezoelectric bulk ceramics, aiming at developing environment-friendly materials to replace the currently market-dominant lead-based piezoelectric ceramics which are generating increasingly aggravated health and environmental concerns. Major achievements and conclusions are summarized as below:

i. Lead-free 0.94KNN-0.06LN piezoelectric ceramics were successfully prepared by ultrasonic irradiation method. Experimental results showed that ultrasonication dramatically decreased the sizes of the starting material aggregates, and enhanced the interaction among the individual reactants even at room temperature. Through the quantitative reaction kinetics study on the activation energies of decomposition of the starting alkali carbonates and formation of the resulting perovskite phase, it was found that the activation energies decreased with increasing ultrasonic power. In addition, it was found that the activation energy barrier for the decomposition of the carbonates was reduced to below the critical value for the crystallization of the perovskite phase with the high ultrasonic irradiation power, so that the rate of the reaction of forming the perovskite phase was not any more limited by the decomposition of the carbonates. The 0.94KNN-0.06LN ceramic samples with a relative density of 94 % were obtained after the

ultrasonic irradiation processing under normal air sintering, which exhibited a piezoelectric coefficient of 184 pC/N. The results showed that ultrasonic irradiation was an effective method in processing KNN-based lead-free piezoelectric ceramics.

ii. Lead-free 0.94KNN-0.06LN piezoelectric ceramics were modified by introducing polymeric agent PVP in the starting raw materials. The addition of PVP suppressed the loss of alkali ions and promoted the perovskite phase formation. Further studies and analyses revealed that the chemical interaction between metal cations and the PVP involves particularly the N in PVP. The decomposition of PVP also generated in-situ heat to promote the decomposition of the raw carbonates and the early perovskite phase formation. It was further observed that PVP with lower molecular weight exhibited more significant effect. The results showed that introducing PVP in the starting raw materials was an effective method for obtaining stoichiometric KNN-LN and other ceramics with volatile alkali ions.

iii. Lead-free $Ba_{0.85}Ca_{0.15}Zr_{0.1}Ti_{0.9}O_3$ (BCZT) piezoelectric ceramics were modified by LiF prepared by ultrasonic irradiation method. The polymorphic rhombohedral-tetragonal phase transition (PPT) temperature was found to shift towards room temperature with the Li doping. An enhanced piezoelectric coefficient of d_{33} = 380 pC/N and a planar electromechanical factor of k_p = 39.5% were obtained at room temperature in the BCZT-xLiF sample with x = 0.06.

iv. Lead-free (1-x)(0.96KNN-0.04LN)-xBCZT piezoelectric ceramics were prepared by ultrasonic irradiation method. The coexistence of orthorhombic and tetragonal phases was identified in the range of $0.008 \leq x \leq 0.013$. The polymorphic orthorhombic-tetragonal phase transition temperature shifted towards room temperature with the increase of the BCZT concentration. For the 0.99(0.96KNN-0.04LN)-0.01BCZT (x = 0.01) ceramic with T_c = 425 °C, improved polarization and enhanced piezoelectric properties, with d_{33} = 180 pC/N and k_p = 0.34, were obtained at room temperature due to the shift of the orthorhombic-tetragonal phase transition towards room temperature. The results showed that (1-x)(0.96KNN-0.04LN)-xBCZT (x = 0.01) ceramic is a promising lead-free piezoelectric material

8.2 Future work

Based on the work done in this thesis, the following recommendations are made for future lead-free piezoelectric ceramics.

i. As discussed and demonstrated in this study, ultrasonic irradiation was an effective method in processing KNN-based and BCZT ceramics. It is interesting to apply this method to explore other lead-free systems such as bismuth layer structure, tungsten bronze structure and bismuth-based perovskite structure, and investigate the ultrasonic irradiation effects in these systems.

ii. From the work done in PVP modified KNN-LN ceramics, PVP has effectively stabilized the alkali volatility problem and improved the electrical properties. From the work done in BCZT ceramics, BaO is also a volatile component.

Therefore, it is interesting to systematically study the PVP effect in the BCZT system.

iii. The lead-free KNN-based piezoelectric ceramics after investigation in this thesis are explored to be used for developing two batteryless remote controller prototypes at IMRE as shown in Fig. 8.1 and Fig. 8.2 respectively. Further study is needed to use lead-free piezoelectric ceramics for other energy harvesting applications.

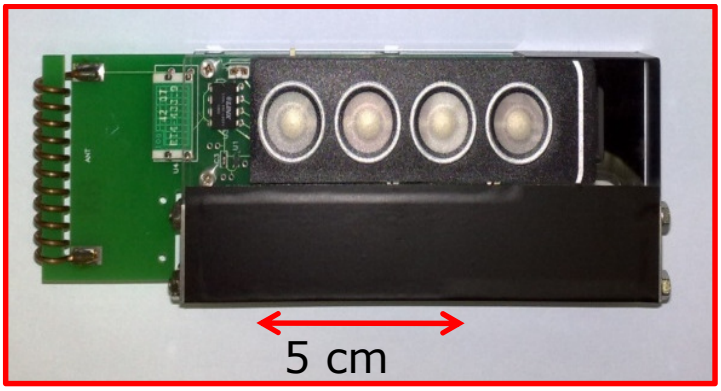

Fig. 8.1. Hand shaking wireless remote controller powered by lead-free KNN-LN piezoelectric ceramic.

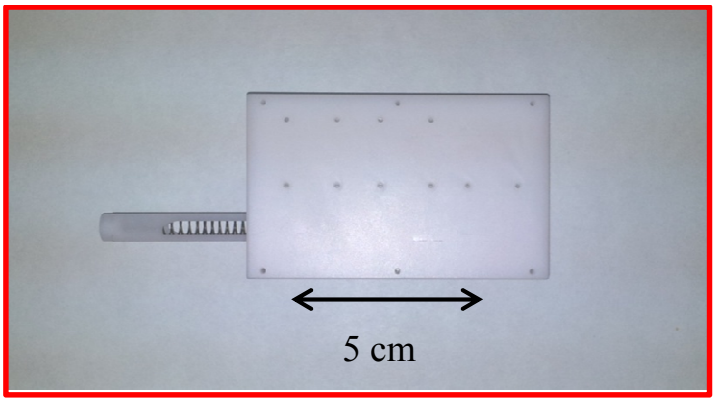

Fig. 8.2. Pressing wireless remote control powered by lead-free KNN-LN piezoelectric ceramic.

References

1. Uchino, K. (2000). *Ferroelectric devices*: Taylor & Francis.
2. Waanders, J. W., & Philips (1991). *Piezoelectric ceramics: Properties and applications*: N. V. Philips' Gloeilampenfabrieken.
3. Haertling, G. H. (1999). Ferroelectric ceramics: history and technology. *Journal of the American Ceramic Society,* 82, 797-818.
4. Jaffe, B., Cook, W. R. & Jaffe, H. (1971). *Piezoelectric ceramics*. London: Academic Press
5. Wang, L., Ren, W., Yao, K., Shi, P., Wu, X. & Yao, X. (2012). Effects of thickness on structures and electrical properties of $K_{0.5}Na_{0.5}NbO_3$ thick films derived from polyvinylpyrrolidone-modified chemical solution. *Ceramics International,* 38, S291-S294.
6. Li, Y., Moon, K.-s. & Wong, C. P. (2005). Electronics without lead. *Science,* 308, 1419-1420.
7. Yao, K., Yu, S. & Tay, F. E. H. (2006). Preparation of perovskite $Pb(Zn_{1/3}Nb_{2/3})O_3$-based thin films from polymer-modified solution precursors. *Applied Physics Letters,* 88, 052904-3.
8. *Directive 2011/65/EC of the European Parliament and of the Council of 8 June 2011 on the restriction of the use of certain hazardous substances in electrical and electronic equipment.,* Union, O. J. E. L174, 2011.
9. Pecht, M., Fukuda, Y. & Rajagopal, S. (2004). The impact of lead-free legislation exemptions on the electronics industry. *Electronics Packaging Manufacturing, IEEE Transactions on,* 27, 221-232.

10. Tressler, J. F., Alkoy, S. & Newnham, R. E. (1998). Piezoelectric sensors and sensor materials. *Journal of Electroceramics,* 2, 257-272.

11. Uchino, K. (1998). Materials issues in design and performance of piezoelectric actuators: an overview. *Acta Materialia,* 46, 3745-3753.

12. Van Uitert, L. G., Levinstein, H. J., Rubin, J. J., Capio, C. D., Dearborn, E. F. & Bonner, W. A. (1968). Some characteristics of niobates having "filled" tetragonal tungsten bronze-like structures. *Materials Research Bulletin,* 3, 47-57.

13. Guo, F. Q., Zhang, B. H., Wang, W. & Chen, H. M. (2012). Effect of different sintering processing on the microstructure of $K_{0.5}Na_{0.5}NbO_3$ ceramics. *Wuji Cailiao Xuebao/Journal of Inorganic Materials,* 27, 277-280.

14. Xie, R. J., & Akimune, Y. (2002). Lead-free piezoelectric ceramics in the (1-x)$Sr_2NaNb_5O_{15}$-x$Ca_2NaNb_5O_{15}$ ($0.05 \leqslant x \leqslant 0.35$) system. *Journal of Materials Chemistry,* 12, 3156-3161.

15. Cummins, S. E., & Cross, L. E. (1968). Electrical and optical properties of ferroelectric $Bi_4Ti_3O_{12}$ single crystals. *Journal of Applied Physics,* 39, 2268-2274.

16. Ikegami, S., & Ueda, I. (1974). Piezoelectricity in ceramics of ferroelectric bismuth compound with layer structure. *Japanese Journal of Applied Physics,* 13, 1572.

17. Irie, H., Miyayama, M. & Kudo, T. (2001). Structure dependence of ferroelectric properties of bismuth layer-structured ferroelectric single crystals. *Journal of Applied Physics,* 90, 4089-4094.

18. Shulman, H. S., Testorf, M., Damjanovic, D. & Setter, N. (1996). Microstructure, electrical conductivity, and piezoelectric properties of bismuth titanate. *Journal of the American Ceramic Society,* 79, 3124-3128.

19. Takenaka, T., & Sakata, K. (1980). Grain orientation and electrical properties of hot-forged $Bi_4Ti_3O_{12}$ ceramics. *Japanese Journal of Applied Physics,* 19, 31-39.

20. Chu, R. Q., Xu, Z. J., Li, G. R., Zeng, H. R., Yu, H. F., Shao, X., Luo, H. S. & Yin, Q. R. (2005). Ultrahigh piezoelectric response along some special cleavage plane in $BaTiO_3$ single-crystals. *Acta Physica Sinica,* 54, 935-938.

21. Dang, F., Kato, K., Imai, H., Wada, S., Haneda, H. & Kuwabara, M. (2009). A new effect of ultrasonication on the formation of $BaTiO_3$ nanoparticles. *Ultrasonics Sonochemistry,* 17, 310-314.

22. Karaki, T., Yan, K. & Adachi, M. (2007). Barium titanate piezoelectric ceramics manufactured by two-step sintering. *Japanese Journal of Applied Physics,* 46, 7035-7038.

23. Karaki, T., Yan, K. & Adachi, M. (2009). High-performance lead-free barium titanate piezoelectric ceramics. *Smart Materials & Micro/Nanosystems,* 54, 7-12.

24. Picht, G., Kungl, H., Baurer, M. & Hoffmann, M. J. (2010). High electric field induced strain in solid-state route processed barium titanate ceramics. *Functional Materials Letters,* 3, 59-64.

25. Takahashi, H., Numamoto, Y., Tani, J., Matsuta, K., Qiu, J. H. & Tsurekawa, S. (2006). Lead-free barium titanate ceramics with large piezoelectric constant fabricated by microwave sintering. *Japanese Journal of Applied Physics Part 2-Letters & Express Letters,* 45, L30-L32.

26. Takahashi, H., Numamoto, Y., Tani, J. & Tsurekawa, S. (2007). Domain properties of high-performance barium titanate ceramics. *Japanese Journal of Applied Physics,* 46, 7044-7047.

27. Chou, C. S., Yang, R. Y., Chen, J. H. & Chou, S. W. (2010). The optimum conditions for preparing the lead-free piezoelectric ceramic of $Bi_{0.5}Na_{0.5}TiO_3$ using the Taguchi method. *Powder Technology,* 199, 264-271.

28. Lin, D. M., Zheng, Q. J., Xu, C. G. & Kwok, K. W. (2008). Structure, electrical properties and temperature characteristics of $Bi_{0.5}Na_{0.5}TiO_3$-$Bi_{0.5}K_{0.5}TiO_3$-$Bi_{0.5}Li_{0.5}TiO_3$ lead-free piezoelectric ceramics. *Applied Physics a-Materials Science & Processing,* 93, 549-558.

29. Maurya, D., Murayama, M. & Priya, S. (2011). Synthesis and characterization of $Na_2Ti_6O_{13}$ whiskers and their transformation to (1-x)$Na_{0.5}Bi_{0.5}TiO_3$-x$BaTiO_3$ ceramics. *Journal of the American Ceramic Society,* 94, 2857-2871.

30. Tian, H. Y., Wang, D. Y., Lin, D. M., Zeng, J. T., Kwok, K. W. & Chan, H. L. W. (2007). Diffusion phase transition and dielectric characteristics of $Bi_{0.5}Na_{0.5}TiO_3$-$Ba(Hf,Ti)O_3$ lead-free ceramics. *Solid State Communications,* 142, 10-14.

31. Overview of smart materials technology. [On-line]. Available: http://resources.edb.gov.hk/physics/articleIE/smartmaterials/SmartMaterials_e.htm.

32. Yoshimura, S., Noguchi, Y. & Miyayama, M. (2006). Crystal growth and electric-field-induced strain in $Bi_{0.5}Na_{0.5}TiO_3$ single crystals. *Transactions of the Materials Research Society of Japan,* 31, 47-50.

33. Nagata, H., & Takenaka, T. (2001). Additive effects on electrical properties of $(Bi_{1/2}Na_{1/2})TiO_3$ ferroelectric ceramics. *Journal of the European Ceramic Society,* 21, 1299-1302.

34. Egerton, L., & Dillon, D. M. (1959). Piezoelectric and dielectric properties of ceramics in the system potassium—sodium niobate. *Journal of the American Ceramic Society,* 42, 438-442.

35. Jaeger, R. E., & Egerton, L. (1962). Hot pressing of potassium-sodium niobates. *Journal of the American Ceramic Society,* 45, 209-213.

36. Jenko, D., Bencan, A., Malic, B., Holc, J. & Kosec, M. (2005). Electron microscopy studies of potassium sodium niobate ceramics. *Microscopy and Microanalysis,* 11, 572-580.

37. Kizaki, Y., Noguchi, Y. & Miyayama, M. (2006). Defect control for low leakage current in $K_{0.5}Na_{0.5}NbO_3$ single crystals. *Applied Physics Letters,* 89.

38. Lin, D. M., Kwok, K. W. & Chan, H. L. W. (2007). Double hysteresis loop in Cu-doped $K_{0.5}Na_{0.5}NbO_3$ lead-free piezoelectric ceramics. *Applied Physics Letters,* 90.

39. Yang, H., Lin, Y., Wang, F. & Luo, H. (2008). Chemical synthesis of $K_{0.5}Na_{0.5}NbO_3$ ceramics and their electrical properties *Materials and Manufacturing Processes,* 23, 489 - 493.

40. Zhang, B. P., Zhang, L. M., Li, J. F., Zhang, J. L. & Jin, S. Z. (2005). SPS sintering of $NaNbO_3$-$KNbO_3$ piezoelectric ceramics. *The Fifth Pacific Rim International Conference on Advanced Materials and Processing,* 475-479, 1165-1168.

41. Saito, Y., Takao, H., Tani, T., Nonoyama, T., Takatori, K., Homma, T., Nagaya, T. & Nakamura, M. (2004). Lead-free piezoceramics. *Nature,* 432, 84-87.

42. Abazari, M., Akdogan, E. K. & Safari, A. (2008). Dielectric and ferroelectric properties of strain-relieved epitaxial lead-free KNN-LT-LS ferroelectric thin films on $SrTiO_3$ substrates. *Journal of Applied Physics,* 103.

43. Byenon, S., & Yoo, J. (2011). Dielectric and piezoelectric properties of $[Li_{0.04}(Na_{0.54}K_{0.46})_{0.96}](Nb_{0.84}Ta_{0.10}Sb_{0.06})O_3$ lead-free ceramics as a function of $(Bi,Na)TiO_3$ substitution. *Ferroelectrics,* 425, 98-105.

44. Chang, Y. F., Yang, Z. P., Hou, Y. T., Liu, Z. H. & Wang, Z. L. (2007). Effects of Li content on the phase structure and electrical properties of lead-free $(K_{0.46-x/2}Na_{0.54-x/2}Li_x)(Nb_{0.76}Ta_{0.20}Sb_{0.04})O_3$ ceramics. *Applied Physics Letters,* 90.

45. Chang, Y. F., Yang, Z. P. & Wei, L. L. (2007). Microstructure, density, and dielectric properties of lead-free $(K_{0.44}Na_{0.52}Li_{0.04})(Nb_{0.96-x}Ta_xSb_{0.04})O_3$ piezoelectric ceramics. *Journal of the American Ceramic Society,* 90, 1656-1658.

46. Chang, Y. F., Yang, Z. P., Xiong, L. R., Liu, Z. H. & Wang, Z. L. (2008). Phase structure, microstructure, and electrical properties of Sb-modified $(K,Na,Li)(Nb,Ta)O_3$ piezoelectric ceramics. *Journal of the American Ceramic Society,* 91, 2211-2216.

47. Chen, Z. W., & Hu, J. Q. (2008). Piezoelectric and dielectric properties of $Li_x(K_{0.46}Na_{0.54})(1-x)(Nb_{0.86}Ta_{0.1}Sb_{0.04})O_3$ lead-free ceramics. *Transactions of Nonferrous Metals Society of China,* 18, 623-626.

48. Fang, J., Wang, X. H. & Li, L. T. (2012). Li, Sb and Ta-modified $(K,Na)NbO_3$ nanopowder prepared via a water-based sol-gel method. *Physica Status Solidi-Rapid Research Letters,* 6, 132-134.

49. Fu, J., Zuo, R. Z., Wu, Y. P., Xu, Z. K. & Li, L. T. (2008). Phase transition and electrical properties of Li-and Ta-substituted $(Na_{0.52}K_{0.48})(Nb_{0.96}Sb_{0.04})O_3$ piezoelectric ceramics. *Journal of the American Ceramic Society,* 91, 3771-3773.

50. Fukada, M., Yamazoe, S. & Wada, T. (2009). Fabrication of lead-free $(Na_{0.52}K_{0.44}Li_{0.04})(Nb_{0.84}Ta_{0.10}Sb_{0.06})O_3$ piezoelectric ceramics by a modified solid-state reaction method. *Japanese Journal of Applied Physics,* 48, 091402.

51. Gao, Y., Zhang, J. L., Qing, Y. L., Tan, Y. Q., Zhang, Z. & Hao, X. P. (2011). Remarkably strong piezoelectricity of lead-free

$(K_{0.45}Na_{0.55})_{0.98}Li_{0.02}(Nb_{0.77}Ta_{0.18}Sb_{0.05})O_3$ ceramic. *Journal of the American Ceramic Society,* 94, 2968-2973.

52. Hong, J., Yoo, J., Lee, K., Lee, S. & Song, H. (2008). Characteristics of acoustic emission sensor using lead-free (LiNaK)(NaTaSb)O_3 ceramics for fluid leak detection at power plant valves. *Japanese Journal of Applied Physics,* 47, 2192-2194.

53. Juan, D., Wang, J. F., Zang, G. Z., Qi, P., Zhang, S. J. & Shrout, T. R. (2008). $(Na_{0.52}K_{0.44}Li_{0.04})(Nb_{0.9-x}Sb_xTa_{0.1})O_3$ lead-free piezoelectric ceramics with high performance and high Curie temperature. *Chinese Physics Letters,* 25, 1446-1448.

54. Lee, S. H., Lee, S. G., Kim, H. J. & Lee, Y. H. (2012). Effect of sintering temperature on piezoelectric and dielectric properties of $0.98(Na_{0.5}K_{0.5})NbO_3$-$0.02Li(Sb_{0.17}Ta_{0.83})O_3$+0.01wt%ZnO ceramics. *Journal of Electroceramics*, 1-4.

55. Lee, S. H., & Lee, Y. H. (2011). Piezoelectric and dielectric properties of $(Na_{0.44}K_{0.52})Nb_{0.84}O_3$-$Li_{0.04}(Sb_{0.06}Ta_{0.1})O_3$ ceramics with sintering temperature. *Electronic Materials Letters,* 7, 205-208.

56. Lee, T., Kwok, K. W. & Chan, H. L. W. (2008). Preparation and piezoelectric properties of CeO_2-added $(Na_{0.475}K_{0.475}Li_{0.05})(Nb_{0.92}Ta_{0.05}Sb_{0.03})O_3$ lead-free ceramics. *Journal of Physics D-Applied Physics,* 41.

57. Lin, D. M., Kwok, K. W. & Chan, H. L. W. (2009). Effect of alkali elements content on the structure and electrical properties of $(K_{0.48}Na_{0.48}Li_{0.04})(Nb_{0.90}Ta_{0.04}Sb_{0.06})O_3$ lead-free piezoelectric ceramics. *Journal of the American Ceramic Society,* 92, 2765-2767.

58. Pang, X. M., Qiu, J. H., Zhu, K. J. & Shao, B. (2011). Influence of sintering temperature on piezoelectric properties of

$(K_{0.4425}Na_{0.52}Li_{0.0375})(Nb_{0.8925}Sb_{0.07}Ta_{0.0375})O_3$ lead-free piezoelectric ceramics. *Journal of Materials Science-Materials in Electronics,* 22, 1783-1787.

59. Rubio-Marcos, F., Marchet, P., Vendrell, X., Romero, J. J., Remondiere, F., Mestres, L. & Fernandez, J. F. (2011). Effect of MnO doping on the structure, microstructure and electrical properties of the (K,Na,Li)(Nb,Ta,Sb)O_3 lead-free piezoceramics. *Journal of Alloys and Compounds,* 509, 8804-8811.

60. Safari, A., Abazari, M., Kerman, K., Marandian-Hagh, N. & Akdogan, E. K. (2009). $(K_{0.44}Na_{0.52}Li_{0.04})$ $(Nb_{0.84}Ta_{0.10}Sb_{0.06})O_3$ ferroelectric ceramics. *IEEE Transactions on Ultrasonics Ferroelectrics and Frequency Control,* 56, 1586-1594.

61. Wu, J. G., Peng, T., Wang, Y. Y., Xiao, D. Q., Zhu, J. M., Jin, Y., Zhu, J., Yu, P., Wu, L. & Jiang, Y. H. (2008). Phase structure and electrical properties of $(K_{0.48}Na_{0.52})(Nb_{0.95}Ta_{0.05})O_3$-$LiSbO_3$ lead-free piezoelectric ceramics. *Journal of the American Ceramic Society,* 91, 319-321.

62. Wu, J. G., Wang, Y. Y., Xiao, D. Q., Zhu, J. G. & Pu, Z. H. (2007). Effects of Ag content on the phase structure and piezoelectric properties of $(K_{0.44-x}Na_{0.52}Li_{0.04}Ag_x)(Nb_{0.91}Ta_{0.05}Sb_{0.04})O_3$ lead-free ceramics. *Applied Physics Letters,* 91.

63. Wu, J. G., Xiao, D. Q., Wang, Y. Y., Wu, W. J., Zhang, B., Zhu, J. G., Pu, Z. H. & Li, Q. S. (2008). Microstructure and electrical properties of (Li,Ag,Ta,Sb)-modified $(K_{0.50}Na_{0.50})NbO_3$ lead-free ceramics with good temperature stability. *Journal of Physics D-Applied Physics,* 41, 125405.

64. Wu, J. G., Xiao, D. Q., Wang, Y. Y., Zhu, J. G., Wu, L. & Jiang, Y. H. (2007). Effects of K/Na ratio on the phase structure and electrical properties of $(K_xNa_{0.96-x}Li_{0.04})(Nb_{0.91}Ta_{0.05}Sb_{0.04})O_3$ lead-free ceramics. *Applied Physics Letters,* 91.

65. Yang, Z. P., Chang, Y. F. & Wei, L. L. (2007). Phase transitional behavior and electrical properties of lead-free $(K_{0.44}Na_{0.52}Li_{0.04})(Nb_{0.96-x}Ta_xSb_{0.04})O_3$ piezoelectric ceramics. *Applied Physics Letters,* 90.

66. Yoo, J., Lee, K., Chung, K., Lee, S., Kim, K., Hong, J., Ryu, S. & Lhee, C. (2006). Piezoelectric and dielectric properties of $(LiNaK)(NbTaSb)O_3$ ceramics with variation in poling temperature. *Japanese Journal of Applied Physics,* 45, 7444-7448.

67. Zhang, B., Xiao, D. Q., Wu, W. J., Li, J., Huang, X. L., Pei, Y., Wu, L., Zhu, J. G. & He, Z. J. (2009). Effect of the sintering temperature on the properties of $0.96(K_{0.5}Na_{0.5})(Nb_{0.96}Sb_{0.04})$-$0.04LiTaO_3$ ceramics. *ISAF: 2009 18th IEEE International Symposium on the Applications of Ferroelectrics*, 149-152.

68. Zuo, R. Z., Fu, J. & Lv, D. Y. (2009). Phase transformation and tunable piezoelectric properties of lead-free $(Na_{0.52}K_{0.48-x}Li_x)(Nb_{1-x-y}Sb_yTa_x)O_3$ system. *Journal of the American Ceramic Society,* 92, 283-285.

69. Zuo, R. Z., Xu, Z. K. & Li, L. T. (2008). Dielectric and piezoelectric properties of Fe_2O_3-doped $(Na_{0.5}K_{0.5})0.96Li_{0.04}Nb_{0.86}Ta_{0.1}Sb_{0.04}O_3$ lead-free ceramics. *Journal of Physics and Chemistry of Solids,* 69, 1728-1732.

70. Pang, X., Qiu, J., Zhu, K. & Cao, Y. (2012). Effects of Sb content on electrical properties of lead-free piezoelectric $(K_{0.4425}Na_{0.52}Li_{0.0375})(Nb_{0.9625-x}Sb_xTa_{0.0375})O_3$ ceramics. *Ceramics International,* 38, 1249-1254.

71. Piezoelectric Effect. [On-line]. Available: https://www.pc-control.co.uk/piezoelectric_effect.htm.

72. Guo, Y. P., Kakimoto, K. & Ohsato, H. (2004). Phase transitional behavior and piezoelectric properties of $(Na_{0.5}K_{0.5})NbO_3$-$LiNbO_3$ ceramics. *Applied Physics Letters,* 85, 4121-4123.

73. Liu, W., & Ren, X. (2009). Large piezoelectric effect in Pb-free ceramics. *Physical Review Letters,* 103, 257602.

74. Xu, Y. (1991). *Ferroelectric materials and their applications*: North-Holland: Elsevier Science and Technology.

75. Nye, J. F. (1985). *Physical properties of crystals: their representation by tensors and matrices*: Oxford University Press, USA.

76. Babooram, K., "New soft chemical routes to ferroelectric materials," Thesis, Simon Fraser University, 2005.

77. Curie, P., & Curie, J. (1880). Development by pressure of polar electricity in hemihedral crystals with inclined faces. *Bulletin de la societe mineralique de france,* 3, 90-93.

78. Akimune, Y., Sugiyama, T., Matsuo, K. & Xie, R. J. (2005). Piezoelectric properties of $Sr_{2-x}Ca_xNaNb_5O_{15}$ (SCNN) ceramics ($0.05 < x < 0.35$) for a smart patch. *Smart Materials III,* 5648, 79-88.

79. Eriksson, M., Yan, H. X., Nygren, M., Reece, M. J. & Shen, Z. J. (2010). Low temperature consolidated lead-free ferroelectric niobate ceramics with improved electrical properties. *Journal of Materials Research,* 25, 240-247.

80. Lopez-Juarez, R., Gonzalez-Garcia, F., Zarate-Medina, J., Escalona-Gonzalez, R., de la Torre, S. D. & Villafuerte-Castrejon, M. E. (2011). Piezoelectric properties of Li-Ta co-doped potassium-sodium niobate ceramics prepared by spark plasma and conventional sintering. *Journal of Alloys and Compounds,* 509, 3837-3842.

81. Sen, C., Alkan, B., Akin, I., Yucel, O., Sahin, F. C. & Goller, G. (2011). Microstructure and ferroelectric properties of spark plasma sintered Li substituted $K_{0.5}Na_{0.5}NbO_3$ ceramics. *Journal of the Ceramic Society of Japan,* 119, 355-361.

82. Shen, Z. Y., & Li, J. F. (2010). Enhancement of piezoelectric constant d_{33} in $BaTiO_3$ ceramics due to nano-domain structure. *Journal of the Ceramic Society of Japan,* 118, 940-943.

83. Shen, Z. Y., Li, J. F., Wang, K., Xu, S. Y., Jiang, W. & Deng, Q. H. (2010). Electrical and mechanical properties of fine-grained Li/Ta-modified $(Na,K)NbO_3$-based piezoceramics prepared by spark plasma sintering. *Journal of the American Ceramic Society,* 93, 1378-1383.

84. Wada, T., Tsuji, K., Saito, T. & Matsuo, Y. (2003). Ferroelectric $NaNbO_3$ ceramics fabricated by spark plasma sintering. *Japanese Journal of Applied Physics,* 42, 6110-6114.

85. Wang, K., Zhang, B. P., Li, J. F. & Liu, H. J. (2007). $Na_{1-x}K_xNbO_3$ (x=0.2 similar to 0.8) lead-free piezoelectric ceramics prepared by spark plasma sintering. *High-Performance Ceramics IV, Pts 1-3,* 336-338, 224-227.

86. Wang, K., Zhang, B. P., Li, J. F. & Zhang, L. M. (2008). Lead-free $Na_{0.5}K_{0.5}NbO_3$ piezoelectric ceramics fabricated by spark plasma sintering: Annealing effect on electrical properties. *Journal of Electroceramics,* 21, 251-254.

87. Yan, H. X., Zhang, H. T., Ubic, R., Reece, M. J., Liu, J., Shen, Z. J. & Zhang, Z. (2005). A lead-free high-Curie-point ferroelectric ceramic, $CaBi_2Nb_2O_9$. *Advanced Materials,* 17, 1261-+.

88. Zhao, P., Zhang, B. P., Wang, K., Zhang, L. M. & Zhang, H. L. (2008). Effect of Li content on the microstructure and properties of lead-free piezoelectric $(K_{0.5}Na_{0.5})$(1-

x)Li_xNbO_3 ceramics prepared by SPS. *Journal of University of Science and Technology Beijing,* 15, 314-319.

89. Zhen, Y. H., Li, J. F., Wang, K., Yan, Y. G. & Yu, L. Q. (2011). Spark plasma sintering of Li/Ta-modified (K,Na)NbO_3 lead-free piezoelectric ceramics: Post-annealing temperature effect on phase structure, electrical properties and grain growth behavior. *Materials Science and Engineering B-Advanced Functional Solid-State Materials,* 176, 1110-1114.

90. Munir, Z., Anselmi-Tamburini, U. & Ohyanagi, M. (2006). The effect of electric field and pressure on the synthesis and consolidation of materials: A review of the spark plasma sintering method. *Journal of Materials Science,* 41, 763-777.

91. Castro, A., Jimenez, B., Hungria, T., Moure, A. & Pardo, L. (2004). Sodium niobate ceramics prepared by mechanical activation assisted methods. *Journal of the European Ceramic Society,* 24, 941-945.

92. Fisher, J. G., Bencan, A., Kosec, M., Vernay, S. & Rytz, D. (2008). Growth of dense single crystals of potassium sodium niobate by a combination of solid-state crystal growth and hot pressing. *Journal of the American Ceramic Society,* 91, 1503-1507.

93. Haertling, G. H. (1967). Properties of hot-pressed ferroelectric alkali niobate ceramics. *Journal of the American Ceramic Society,* 50, 329-330.

94. Hao, H., Liu, H. X. & Ouyang, S. X. (2008). Processing and property of textured lead-free $SrTi_4Bi_4O_{15}$ piezoelectric ceramics. *Journal of Electroceramics,* 21, 255-257.

95. Hiruma, Y., Aoyagi, R., Nagata, H. & Takenaka, T. (2005). Ferroelectric and piezoelectric properties of $(Bi_{1/2}K_{1/2})TiO_3$ ceramics. *Japanese Journal of Applied Physics,* 44, 5040-5044.

96. Lee, D. S., Jeong, S. J., Park, E. C. & Song, J. S. (2006). Characteristic of grain oriented $(Bi_{0.5}Na_{0.5})TiO_3$-$BaTiO_3$ ceramics. *Journal of Electroceramics,* 17, 505-508.

97. Song, J. S., Jeong, S. J., Kim, I. S., Lee, D. S. & Park, E. C. (2006). Piezoelectric and dielectric properties in grain oriented $(Bi_{0.5}Na_{0.5})TiO_3$-$BaTiO_3$ ceramics. *Ferroelectrics,* 338, 1419-1424.

98. Zhang, S., Ru, X., Thomas, S., Zang, R., Guozhong & Wang, J. (2007). Characterization of lead free $(K_{0.5}Na_{0.5})NbO_3$–$LiSbO_3$ piezoceramic *Solid State Communications,* 141, 675-679.

99. Zhang, S. J., Lee, H. J., Ma, C. & Tan, X. L. (2011). Sintering effect on microstructure and properties of $(K,Na)NbO_3$ ceramics. *Journal of the American Ceramic Society,* 94, 3659-3665.

100. Hot pressing. [On-line]. Available: http://www.dynacer.com/hot_pressing.htm.

101. Webster, E. (1963). Cavitation. *Ultrasonics,* 1, 39-48.

102. Bang, J. H., & Suslick, K. S. (2010). Applications of ultrasound to the synthesis of nanostructured materials. *Advanced Materials,* 22, 1039-1059.

103. Suslick, K. S. (1990). Sonochemistry. *Science,* 247, 1439-1445.

104. Suslick, K. S., & Casadonte, D. J. (1987). Heterogeneous sonocatalysis with nickel powder. *Journal of the American Chemical Society,* 109, 3459-3461.

105. Suslick, K. S., Casadonte, D. J. & Doktycz, S. J. (1989). The effects of ultrasound on nickel and copper powders. *Solid State Ionics,* 32-33, 444-452.

106. Suslick, K. S., Casadonte, D. J., Green, M. L. H. & Thompson, M. E. (1987). Effects of high intensity ultrasound on inorganic solids. *Ultrasonics,* 25, 56-59.

107. Suslick, K. S., Choe, S.-B., Cichowlas, A. A. & Grinstaff, M. W. (1991). Sonochemical synthesis of amorphous iron. *Nature,* 353, 414-416.

108. Suslick, K. S., Fang, M. & Hyeon, T. (1996). Sonochemical synthesis of iron colloids. *Journal of the American Chemical Society,* 118, 11960-11961.

109. Suslick, K. S., Goodale, J. W., Schubert, P. F. & Wang, H. H. (1983). Sonochemistry and sonocatalysis of metal carbonyls. *Journal of the American Chemical Society,* 105, 5781-5785.

110. Suslick, K. S., & Johnson, R. E. (1984). Sonochemical activation of transition metals. *Journal of the American Chemical Society,* 106, 6856-6858.

111. Ultrasonic probe. [On-line]. Available: http://www.scs.illinois.edu/~suslick/sonochembrittanica.html.

112. Baranchikov, A. E., Ivanov, V. K., Murav'eva, G. P., Oleinikov, N. N. & Tret'yakov, Y. D. (2004). Kinetics of the formation of zinc ferrite in an ultrasonic field. *Doklady Chemistry,* 397, 146-148.

113. Baranchikov, A. Y., Ivanov, V. K. & Tretyakov, Y. D. (2007). Kinetics and mechanism of nickel ferrite formation under high temperature ultrasonic treatment. *Ultrasonics Sonochemistry,* 14, 131-134.

114. Barantchikov, A. Y., Baranov, A. N., Ivanov, V. K., Oleynikov, N. N. & Tretyakov, Y. D. (2001). Processes in oxide systems under ultrasonic treatment at high temperatures. *Solid State Ionics,* 141-142, 689-694.

115. Prozorov, T., Prozorov, R. & Suslick, K. S. (2004). High velocity interparticle collisions driven by ultrasound. *Journal of the American Chemical Society,* 126, 13890-13891.

116. Xu, M., Lu, Y.-n., Liu, Y.-f., Shi, S.-z., Qian, T.-s. & Lu, D.-y. (2006). Sonochemical synthesis of monosized spherical $BaTiO_3$ particles. *Powder Technology,* 161, 185-189.

117. Kozuka, H., & Kajimura, M. (2000). Single-step dip coating of crack-free $BaTiO_3$ films >1 μm thick: effect of poly(vinylpyrrolidone) on critical thickness. *Journal of the American Ceramic Society,* 83, 1056-1062.

118. Takenaka, S., & Kozuka, H. (2001). Sol-gel preparation of single-layer, 0.75 μm thick lead zirconate titanate films from lead nitrate-titanium and zirconium alkoxide solutions containing polyvinylpyrrolidone. *Applied Physics Letters,* 79, 3485-3487.

119. Yao, K., Yu, S. & Tay, F. E.-H. (2003). Residual stress analysis in ferroelectric $Pb(Zr_{0.52}Ti_{0.48})O_3$ thin films fabricated by a sol-gel process. *Applied Physics Letters,* 82, 4540-4542.

120. Jia, Q. X., McCleskey, T. M., Burrell, A. K., Lin, Y., Collis, G. E., Wang, H., Li, A. D. Q. & Foltyn, S. R. (2004). Polymer-assisted deposition of metal-oxide films. *Nature Materials,* 3, 529-532.

121. Yu, S., Yao, K. & Tay, F. E. H. (2006). Structure and properties of (1−x)PZN−xPT thin films with perovskite phase promoted by polyethylene glycol. *Chemistry of Materials,* 18, 5343-5350.

122. Yu, S., Yao, K. & Tay, F. (2007). Structure and properties of $(1-x)(0.6Pb(Zn_{1/3}Nb_{2/3})O_3\text{-}0.4Pb(Mg_{1/3}Nb_{2/3})O_3)\text{-}PbTiO_3$ thin films with perovskite phase promoted by polyethylene glycol. *Journal of Sol-Gel Science and Technology,* 42, 357-364.

123. Yu, S., Yao, K. & Tay, F. E. H. (2007). Observations and analyses on the thermal stability of $(1-x)Pb(Zn_{1/3}Nb_{2/3})O_3-xPbTiO_3$ thin films. *Chemistry of Materials,* 19, 4373-4377.

124. Swartz, S. L., & Shrout, T. R. (1982). Fabrication of perovskite lead magnesium niobate. *Materials Research Bulletin,* 17, 1245-1250.

125. Yu, S., Huang, H. & Zhou, L. (2007). Novel solid-state reaction route to synthesize $Pb(Mg_{1/3}Nb_{2/3})O_3$−$PbTiO_3$ ceramics with a pure perovskite phase. *Chemistry of Materials,* 19, 2718-2720.

126. Yu, S., Huang, H., Zhou, L. & Ye, Y. (2008). A polyethylene glycol-modified solid-state reaction route to synthesize relaxor ferroelectric $Pb(Mg_{1/3}Nb_{2/3})O_3$–$PbTiO_3$ (PMN–PT). *Journal of the American Ceramic Society,* 91, 1057-1064.

127. Nakashima, Y., Sakamoto, W., Maiwa, H., Shimura, T. & Yogo, T. (2007). Lead-free piezoelectric $(K,Na)NbO_3$ thin Films derived from metal alkoxide precursors. *Japanese Journal of Applied Physics,* 46, L311-L313.

128. Wang, L. Y., Yao, K. & Ren, W. (2008). Piezoelectric $K_{0.5}Na_{0.5}NbO_3$ thick films derived from polyvinylpyrrolidone-modified chemical solution deposition. *Applied Physics Letters,* 93, 092903-92913.

129. Wang, L., Yao, K., Goh, P. C. & Ren, W. (2009). Volatilization of alkali Ions and effects of molecular weight of polyvinylpyrrolidone introduced in solution-derived $K_{0.5}Na_{0.5}NbO_3$ films. *Journal of Materials Research,* 24, 3516-3522.

130. Wang, L. Y., Ren, W., Yao, K., Goh, P. C., Shi, P., Wu, X. Q. & Yao, X. (2010). Effect of pyrolysis temperature on $K_{0.5}Na_{0.5}NbO_3$ thick films derived from polyvinylpyrrolidone-modified chemical solution. *Journal of the American Ceramic Society,* 93, 3686-3690.

131. Wang, L. Y., Yao, K. & Ren, W. (2010). Effect of amount of polyvinylpyrrolidone introduced in solution-derived ferroelectric $K_{0.5}Na_{0.5}NbO_3$ thick films. *Ferroelectrics,* 404, 192-199.

132. Goh, P. C., Yao, K. & Chen, Z. (2010). Lead-free piezoelectric $(K_{0.5}Na_{0.5})NbO_3$ thin films derived from chemical solution modified with stabilizing agents. *Applied Physics Letters,* 97.

133. Goh, P. C., Yao, K. & Chen, Z. (2012). Reaction mechanisms of ethylenediaminetetraacetic acid and diethanolamine in the precursor solution for producing $(K,Na)NbO_3$ thin films with outstanding piezoelectric properties. *The Journal of Physical Chemistry C,* 116, 15550-15556.

134. Lee, Y.-h., Cho, J.-h., Kim, B.-i. & Choi, D.-k. (2008). Piezoelectric properties and densification based on control of volatile mass of potassium and sodium in $(K_{0.5}Na_{0.5})NbO_3$ ceramics. *Japanese Journal of Applied Physics,* 47, 4620.

135. Nagata, H., Matsuzawa, S., Hiruma, Y. & Takenaka, T. (2006). Piezoelectric properties of Nd and V co-substituted $Bi_4Ti_3O_{12}$ Ceramics for resonator applications. *2006 IEEE Ultrasonics Symposium, Vols 1-5, Proceedings*, 355-358.

136. Takenaka, T., & Nagata, H. (2006). Grain orientation and electrical properties of some bismuth layer-structured ferroelectrics for lead-free piezoelectric applications. *Ferroelectrics,* 336, 119-136.

137. Takenaka, T., Nagata, H., Tokutsu, T., Miyabayashi, K. & Hiruma, Y. (2009). High temperature piezoelectric properties of some bismuth layer-structured ferroelectric ceramics. *Advances in Electroceramic Materials,* 204, 167-175.

138. Xie, L. J., Xu, G. J. & Li, Z. X. (2008). Preparation and characterization of high textured $KSr_2Nb_5O_{15}$ lead-free piezoelectric ceramics. *High-Performance Ceramics V, Pts 1 and 2,* 368-372, 1905-1907.

139. Kwei, G. H., Lawson, A. C., Billinge, S. J. L. & Cheong, S. W. (1993). Structures of the ferroelectric phases of barium titanate. *The Journal of Physical Chemistry,* 97, 2368-2377.

140. Takenaka, T., Maruyama, K.-i. & Sakata, K. (1991). $(Bi_{1/2}Na_{1/2})TiO_3$-$BaTiO_3$ system for lead-free piezoelectric ceramics. *Japanese Journal of Applied Physics,* 30, 2236.

141. Sakata, K., & Masuda, Y. (1974). Ferroelectric and antiferroelectric properties of $(Na_{0.5}Bi_{0.5})TiO_3$-$SrTiO_3$ solid solution ceramics *Ferroelectrics,* 7, 347 - 349.

142. Zhao, S., & *et al.* (2006). Ferroelectric and piezoelectric properties of $(Na,K)_{0.5}Bi_{0.5}TiO_3$ lead free ceramics. *Journal of Physics D: Applied Physics,* 39, 2277.

143. Wang, X. X., Tang, X. G. & Chan, H. L. W. (2004). Electromechanical and ferroelectric properties of $(Bi_{1/2}Na_{1/2})TiO_3$-$(Bi_{1/2}K_{1/2})TiO_3$-$BaTiO_3$ lead-free piezoelectric ceramics. *Applied Physics Letters,* 85, 91-93.

144. Matthias, B. T. (1949). New ferroelectric crystals. *Physical Review,* 75, 1771.

145. Matthias, B. T., & Remeika, J. P. (1951). Dielectric properties of sodium and potassium niobates. *Physical Review,* 82, 727.

146. Shirane, G., Danner, H., Pavlovic, A. & Pepinsky, R. (1954). Phase transitions in ferroelectric $KNbO_3$. *Physical Review,* 93, 672.

147. Egerton, L., & Dillon, D. M. (1959). Piezoelectric and dielectric properties of ceramics in the system potassium-sodium niobate. *Journal of the American Ceramic Society,* 42, 438-442.

148. Park, S.-H., Ahn, C.-W., Nahm, S. & Song, J.-S. (2004). Microstructure and piezoelectric properties of ZnO-added $(Na_{0.5}K_{0.5})NbO_3$ ceramics. *Japanese Journal of Applied Physics,* 43, L1072.

149. Matsubara, M., Yamaguchi, T., Kikuta, K. & Hirano, S.-i. (2004). Sinterability and piezoelectric properties of (K,Na)NbO_3 ceramics with novel sintering aid. *Japanese Journal of Applied Physics,* 43, 7159.

150. Matsubara, M., Yamaguchi, T., Kikuta, K. & Hirano, S.-i. (2005). Sintering and piezoelectric properties of potassium sodium niobate ceramics with newly developed sintering aid. *Japanese Journal of Applied Physics,* 44, 258.

151. Chang, Y., Yang, Z., Wei, L. & Liu, B. (2006). Effects of $AETiO_3$ additions on phase structure, microstructure and electrical properties of $(K_{0.5}Na_{0.5})NbO_3$ ceramics. *Materials Science and Engineering A,* 437, 301-305.

152. Lin, D., Kwok, K. W. & Chan, H. L. W. (2008). Piezoelectric and ferroelectric properties of Cu-doped $K_{0.5}Na_{0.5}NbO_3$ lead-free ceramics. *Journal of Physics D: Applied Physics,* 41, 045401.

153. Lin, D., Kwok, K. W. & Chan, H. L. W. (2008). Piezoelectric and ferroelectric properties of $K_xNa_{1-x}NbO_3$ lead-free ceramics with MnO_2 and CuO doping *Journal of Alloys and Compounds,* 461, 273-278.

154. Fisher, J. G., & Kang, S.-J. L. (2009). Microstructural changes in $(K_{0.5}Na_{0.5})NbO_3$ ceramics sintered in various atmospheres *Journal of the European Ceramic Society,* 29, 2581-2588.

155. Li, J.-F., Wang, K., Zhang, B.-P. & Zhang, L.-M. (2006). Ferroelectric and piezoelectric properties of fine-grained $Na_{0.5}K_{0.5}NbO_3$ lead-free piezoelectric ceramics prepared by spark plasma sintering. *Journal of the American Ceramic Society,* 89, 706-709.

156. Malic, B., Bernard, J., Bencan, A. & Kosec, M. (2008). Influence of zirconia addition on the microstructure of $K_{0.5}Na_{0.5}NbO_3$ ceramics *Journal of the European Ceramic Society,* 28, 1191-1196.

157. Liu, T., Ding, A. L., He, X. Y., Zheng, X. S., Qiu, P. S. & Cheng, W. X. (2006). Dielectric and piezoelectric properties of Mn-doped $(K,Na)_{0.96}Sr_{0.02}NbO_3$ ceramics. *Physica Status Solidi A,* 203, 3861-3867.

158. Cross, E. (2004). Materials science: lead-free at last. *Nature,* 432, 24-25.

159. Lin, D., Kwok, K. W. & Chan, H. L. W. (2007). Structure, dielectric, and piezoelectric properties of CuO-doped $K_{0.5}Na_{0.5}NbO_3$-$BaTiO_3$ lead-free ceramics. *Journal of Applied Physics,* 102.

160. Zuo, R., Ye, C. & Fang, X. (2008). $Na_{0.5}K_{0.5}NbO_3$-$BiFeO_3$ lead-free piezoelectric ceramics *Journal of Physics and Chemistry of Solids,* 69, 230-235.

161. Zuo, R. Z., Ye, C. & Fang, X. S. (2007). Dielectric and piezoelectric properties of lead free $Na_{0.5}K_{0.5}NbO_3$-$BiScO_3$ ceramics. *Japanese Journal of Applied Physics Part 1-Regular Papers Brief Communications & Review Papers,* 46, 6733-6736.

162. Guo, Y. P., Kakimoto, K. & Ohsato, H. (2005). $(Na_{0.5}K_{0.5})NbO_3$-$LiTaO_3$ lead-free piezoelectric ceramics. *Materials Letters,* 59, 241-244.

163. Dai, Y. J., Zhang, X. W. & Zhou, G. Y. (2007). Phase transitional behavior in $K_{0.5}Na_{0.5}NbO_3$-$LiTaO_3$ ceramics. *Applied Physics Letters,* 90.

164. Kim, M. S., Jeong, S. J. & Song, J. S. (2007). Effect of A-site ions additions on abnormal grain growth and piezoelectric properties in NKN-5LT systems. *Recrystallization and Grain Growth III, Pts 1 and 2,* 558-559, 763-766.

165. Skidmore, T. A., & Milne, S. J. (2007). Phase development during mixed-oxide processing of a $[Na_{0.5}K_{0.5}NbO_3](1-x)[LiTaO_3]_x$ powder. *Journal of Materials Research,* 22, 2265-2272.

166. Meng, H. Q., Yang, Y., Wang, Y. P., Wan, D. D., Li, Q. A. & Cheng, Y. (2010). Alkaline earth elements modified lead-free $0.96(K_{0.5}Na_{0.5})NbO_3$-$0.04LiTaO_3$ ceramics. *Ferroelectrics,* 404, 105-111.

167. Wang, H. Q., Ruan, D. S., Dai, Y. J. & Zhang, X. W. (2012). Relationship between phase structure and electrical properties of $(K_{0.5}Na_{0.5})NbO_3$-$LiTaO_3$ lead-free ceramics. *Current Applied Physics,* 12, 504-508.

168. Yang, Z., Chang, Y. F., Liu, B. & Wei, L. L. (2006). Effects of composition on phase structure, microstructure and electrical properties of $(K_{0.5}Na_{0.5})NbO_3$-$LiSbO_3$ ceramics. *Materials Science and Engineering a-Structural Materials Properties Microstructure and Processing,* 432, 292-298.

169. Lin, D. M., Kwok, K. W., Lam, K. H. & Chan, H. L. W. (2007). Structure and electrical properties of $K_{0.5}Na_{0.5}NbO_3$-$LiSbO_3$ lead-free piezoelectric ceramics. *Journal of Applied Physics,* 101.

170. Wu, J., Xiao, D., Wang, Y., Zhu, J. & Yu, P. (2008). Effects of K content on the dielectric, piezoelectric, and ferroelectric properties of $0.95(K_xNa_{1-x})NbO_3$-$0.05LiSbO_3$ lead-free ceramics. *Journal of Applied Physics,* 103, 024102.

171. Yoo, J., Kim, D., Lee, Y., Lee, I., Lee, S., Kim, I. & Song, J. (2009). Effect of Nb substitution on the piezoelectric and dielectric properties of $0.95(K_{0.5}Na_{0.5})NbO_3$-$0.05Li(Sb_{1-x}Nb_x)O_3$ ceramics. *Integrated Ferroelectrics,* 105, 18-26.

172. Jiang, M. H., Liu, X. Y., Cheng, J., Zhou, X. J. & Deng, M. J. (2010). Effects of sintering temperature on the microstructure and electrical properties of $BiMnO_3$-

doped $0.95Na_{0.5}K_{0.5}NbO_3$-$0.05LiSbO_3$ ceramics. *Materials and Manufacturing Processes,* 25, 730-734.

173. Palei, P. K., & Kumar, P. (2012). Role of sintering temperature on the phase stability and electrical properties of $0.94(K_{0.5}Na_{0.5})NbO_3$-$0.06LiSbO_3$ ceramics. *Japanese Journal of Applied Physics,* 51, 011503.

174. Azough, F., Wegrzyn, M., Freer, R., Sharma, S. & Hall, D. (2011). Microstructure and piezoelectric properties of CuO added (K, Na, Li)NbO_3 lead-free piezoelectric ceramics. *Journal of the European Ceramic Society,* 31, 569-576.

175. Chao, W., Yudong, H., Ningning, W., Mankang, Z., Hao, W. & Hui, Y. (2009). Preparation and phase transformation of $(Li_{0.06}Na_{0.47}K_{0.47})NbO_3$ nano-powders derived from sol-gel process. *Acta Chimica Sinica,* 67, 203-207.

176. Chen, Q., Lan, D. J., Chen, Y., Lin, D. M., Yue, X., Xiao, D. Q. & Zhu, J. G. (2007). Influence MnO_2 on the properties of $(Li_xNa_yK_{1-x-y})NbO_3$ ceramics. *High-Performance Ceramics IV, Pts 1-3,* 336-338, 199-202.

177. Du, H. L., Tang, F. S., Liu, D. J., Zhu, D. M., Zhou, W. C. & Qu, S. B. (2007). The microstructure and ferroelectric properties of $(K_{0.5}Na_{0.5})NbO_3$-$LiNbO_3$ lead-free piezoelectric ceramics. *Materials Science and Engineering B-Solid State Materials for Advanced Technology,* 136, 165-169.

178. Du, H. L., Tang, F. S., Luo, F., Zhou, W. C., Qu, S. B. & Pei, Z. B. (2007). Effect of poling condition on piezoelectric properties of $(K_{0.5}Na_{0.5})NbO_3$-$LiNbO_3$ lead-free piezoelectric ceramics. *Materials Science and Engineering B-Solid State Materials for Advanced Technology,* 137, 175-179.

179. Du, H. L., Tang, F. S., Luo, F., Zhu, D. M., Qu, S. B., Pei, Z. B. & Zhou, W. C. (2007). Influence of sintering temperature on piezoelectric properties of

$(K_{0.5}Na_{0.5})NbO_3$-$LiNbO_3$ lead-free piezoelectric ceramics. *Materials Research Bulletin,* 42, 1594-1601.

180. Hagh, N. M., Jadidian, B. & Safari, A. (2007). Property-processing relationship in lead-free (K,Na,Li)NbO_3-solid solution system. *Journal of Electroceramics,* 18, 339-346.

181. Higashide, K., Kakimoto, K. I. & Ohsato, H. (2007). Temperature dependence on the piezoelectric property of (1-x)$(Na_{0.5}K_{0.5})NbO_3$-x$LiNbO_3$ ceramics. *Journal of the European Ceramic Society,* 27, 4107-4110.

182. Hollenstein, E., Damjanovic, D. & Setter, N. (2007). Temperature stability of the piezoelectric properties of Li-modified KNN ceramics. *Journal of the European Ceramic Society,* 27, 4093-4097.

183. Hollenstein, E., Davis, M., Damjanovic, D. & Setter, N. (2005). Piezoelectric properties of Li- and Ta-modified $(K_{0.5}Na_{0.5})NbO_3$ ceramics. *Applied Physics Letters,* 87.

184. Huang, R. X., Zhao, Y. Z., Zhang, X. W., Zhao, Y. J., Liu, R. Z. & Zhou, H. P. (2010). Low-temperature sintering of CuO-doped 0.94$(K_{0.48}Na_{0.535})NbO_3-0.06LiNbO_3$ lead-free piezoelectric ceramics. *Journal of the American Ceramic Society,* 93, 4018-4021.

185. Kakimoto, K., Akao, K., Guo, Y. P. & Ohsato, H. (2005). Raman scattering study of piezoelectric $(Na_{0.5}K_{0.5})NbO_3$-$LiNbO_3$ ceramics. *Japanese Journal of Applied Physics,* 44, 7064-7067.

186. Kakimoto, K., Ando, K. & Ohsato, H. (2010). Grain size control of lead-free Li0.06$(Na_{0.5}K_{0.5})$0.94NbO_3 piezoelectric ceramics by Ba and Ti doping. *Journal of the European Ceramic Society,* 30, 295-299.

187. Kakimoto, K., Sumi, T. & Kagomiya, I. (2010). Pressure-dependent raman scattering spectrum of piezoelectric (Li,Na,K)NbO_3 lead-free ceramics. *Japanese Journal of Applied Physics,* 49.

188. Kakimoto, K. I., Hotta, T. & Ohsato, H. (2010). Phase transition and structural analysis of (Li,Na,K)NbO_3 lead-free piezoelectric ceramics. *Asian Ceramic Science for Electronics III and Electroceramics in Japan XII,* 421-422, 3-8.

189. Kumar, P., & Palei, P. (2010). Effect of sintering temperature on ferroelectric properties of 0.94($K_{0.5}Na_{0.5}$)NbO_3-0.06$LNbO_3$ system. *Ceramics International,* 36, 1725-1729.

190. Lee, S. C., Wang, L., Yeo, H. G., Cho, J. H., Sung, Y. S., Kim, M. H., Song, T. K., Kim, S. S. & Choi, B. C. (2009). Effects of A-site ionic contents on piezoelectric and ferroelectric properties of lead-free ($K_{0.5}Na_{0.5}$)NbO_3-$LiNbO_3$ ceramics. *Ferroelectrics,* 381, 176-182.

191. Li, H. T., Zhang, B. P., Cui, M., Yang, W. G., Ma, N. & Li, J. F. (2011). Microstructure, crystalline phase, and electrical properties of ZnO-added $Li_{0.06}(Na_{0.535}K_{0.48})_{0.94}NbO_3$ ceramics. *Current Applied Physics,* 11, S184-S188.

192. Li, Q. S., Chen, L., Chen, Q., Yue, X., Xiao, D. Q. & Zhu, J. G. (2009). Effects of Na content on the phase structure and electrical properties of 0.94(Na_xK_{1-x})NbO_3-0.06$LiNbO_3$ ceramics. *Ferroelectrics,* 380, 190-195.

193. Lin, D. M., & Kwok, K. W. (2011). Piezoelectric properties of $K_{0.47}Na_{0.47}Li_{0.06}NbO_3$-$NaSbO_3$ lead-free ceramics for ultrasonic transducer applications. *International Journal of Applied Ceramic Technology,* 8, 684-690.

194. Niu, X. K., Zhang, J. L., Wu, L., Zheng, P., Zhao, M. L. & Wang, C. L. (2008). Crystalline structural phase boundaries in (K,Na,Li)NbO_3 ceramics. *Solid State Communications,* 146, 395-398.

195. Song, H. C., Cho, K. H., Park, H. Y., Ahn, C. W., Nahm, S., Uchino, K. & Park, S. H. (2007). Microstructure and piezoelectric properties of (1-x)($Na_{0.5}K_{0.5}$)NbO_3-x$LiNbO_3$ ceramics. *Journal of the American Ceramic Society,* 90, 1812-1816.

196. Sun, X. Y., Deng, J. X., Chen, J., Sun, C. & Xing, X. R. (2009). Effects of Li substitution on the structure and ferroelectricity of (Na,K)NbO_3. *Journal of the American Ceramic Society,* 92, 3033-3036.

197. Tachi, S., Kakimoto, K. & Kagomiya, I. (2012). Temperature dependence of elastic and piezoelectric properties of lead-free (Li,Na,K)NbO_3 ceramics. *Ceramics International,* 38, S311-S314.

198. Tang, F. S., Du, H. L., Li, Z. M., Zhou, W. C., Qu, S. B. & Pei, Z. B. (2006). Preparation and properties of ($K_{0.5}Na_{0.5}$)NbO_3-$LiNbO_3$ ceramics. *Transactions of Nonferrous Metals Society of China,* 16, S466-S469.

199. Tang, F. S., Du, H. L., Liu, D. J., Luo, F. & Zhou, W. C. (2007). Sintering characteristic and piezoelectric properties of lead-free ($K_{0.5}Na_{0.5}$)NbO_3-$LiNbO_3$ ceramics. *Journal of Inorganic Materials,* 22, 323-327.

200. Wan, D. D., Yang, Y., Li, Q. & Zhu, K. J. (2008). Stable resonance characteristics in CuO-modified lead-free 0.94($K_{0.5}Na_{0.5}$)NbO_3-0.06$LiNbO_3$ ceramics sintered at optimal temperature. *2008 IEEE Ultrasonics Symposium, Vols 1-4 and Appendix*, 1429-1432.

201. Wang, C., Hou, Y. D., Ge, H. Y., Zhu, M. K. & Yan, H. (2009). Crystal structure and orthorhombic-tetragonal phase transition of nanoscale $(Li_{0.06}Na_{0.47}K_{0.47})NbO_3$. *Journal of the European Ceramic Society,* 29, 2589-2594.

202. Wang, K., Li, J. F. & Liu, N. (2008). Piezoelectric properties of low-temperature sintered Li-modified (Na, K)NbO_3 lead-free ceramics. *Applied Physics Letters,* 93, 092904.

203. Zeng, J. T., Zhang, Y. H., Li, G. R., Zheng, L. Y. & Yin, Q. R. (2010). Enhanced piezoelectric properties of high-T_c $(K_{0.5+x}Na_{0.5-x})NbO_3$-$LiNbO_3$ ceramics. *Ferroelectrics,* 403, 127-133.

204. Zhao, Y. J., Zhao, Y. Z., Zhang, X. W., Huang, R. X., Liu, R. Z. & Zhou, H. P. (2012). The effect of sintering and poling processing on the phase structure of $Li_{0.058}(Na_{0.51}K_{0.49})_{0.942}NbO_3$ lead-free ceramics. *Scripta Materialia,* 66, 97-100.

205. Hennings, D., & Rosenstein, G. (1984). Temperature-stable dielectrics based on chemically inhomogeneous $BaTiO_3$. *Journal of the American Ceramic Society,* 67, 249-254.

206. Benabdallah, F., Simon, A., Khemakhem, H., Elissalde, C. & Maglione, M. (2011). Linking large piezoelectric coefficients to highly flexible polarization of lead free $BaTiO_3$-$CaTiO_3$-$BaZrO_3$ ceramics. *Journal of Applied Physics,* 109.

207. Piorra, A., Petraru, A., Kohlstedt, H., Wuttig, M. & Quandt, E. (2011). Piezoelectric properties of $0.5(Ba_{0.7}Ca_{0.3})TiO_3$-$0.5[Ba(Zr_{0.2}Ti_{0.8})O_3]$ ferroelectric lead-free laser deposited thin films. *Journal of Applied Physics,* 109.

208. Su, S., Zuo, R. Z., Lu, S. B., Xu, Z. K., Wang, X. H. & Li, L. T. (2011). Poling dependence and stability of piezoelectric properties of $Ba(Zr_{0.2}Ti_{0.8})O_3$-

$(Ba_{0.7}Ca_{0.3})TiO_3$ ceramics with huge piezoelectric coefficients. *Current Applied Physics,* 11, S120-S123.

209. Wang, P., Li, Y. X. & Lu, Y. Q. (2011). Enhanced piezoelectric properties of $(Ba_{0.85}Ca_{0.15})(Ti_{0.9}Zr_{0.1})O_3$ lead-free ceramics by optimizing calcination and sintering temperature. *Journal of the European Ceramic Society,* 31, 2005-2012.

210. Wu, J. G., Xiao, D. Q., Wu, W. J., Chen, Q., Zhu, J. G., Yang, Z. C. & Wang, J. (2011). Role of room-temperature phase transition in the electrical properties of $(Ba,Ca)(Ti,Zr)O_3$ ceramics. *Scripta Materialia,* 65, 771-774.

211. Xue, D. Z., Zhou, Y. M., Bao, H. X., Zhou, C., Gao, J. H. & Ren, X. B. (2011). Elastic, piezoelectric, and dielectric properties of $Ba(Zr_{0.2}Ti_{0.8})O_3$-$50(Ba_{0.7}Ca_{0.3})TiO_3$ Pb-free ceramic at the morphotropic phase boundary. *Journal of Applied Physics,* 109.

212. Hao, J., Bai, W., Li, W. & Zhai, J. (2012). Correlation between the microstructure and electrical properties in high-performance $(Ba_{0.85}Ca_{0.15})(Zr_{0.1}Ti_{0.9})O_3$ lead-free piezoelectric ceramics. *Journal of the American Ceramic Society,* 95, 1998-2006.

213. Wu, J., Xiao, D., Wu, W., Chen, Q., Zhu, J., Yang, Z. & Wang, J. (2012). Composition and poling condition-induced electrical behavior of $(Ba_{0.85}Ca_{0.15})(Ti_{1-x}Zr_x)O_3$ lead-free piezoelectric ceramics. *Journal of the European Ceramic Society,* 32, 891-898.

214. Yi, X., Li, J., Xie, S., Gong, Y. & Li, L. (2012). Synthesis and characterizations of BZT-BCT lead-free piezoelectric ceramic for energy harvesting applications. *Yadian Yu Shengguang/Piezoelectrics and Acoustooptics,* 34, 140-142+162.

215. Bao, H. X., Zhou, C., Xue, D. Z., Gao, J. H. & Ren, X. B. (2010). A modified lead-free piezoelectric BZT-xBCT system with higher T_c. *Journal of Physics D-Applied Physics,* 43.

216. Li, W., Xu, Z. J., Chu, R. Q., Fu, P. & Zang, G. Z. (2010). Polymorphic phase transition and piezoelectric properties of $(Ba_{1-x}Ca_x)(Ti_{0.9}Zr_{0.1})O_3$ lead-free ceramics. *Physica B-Condensed Matter,* 405, 4513-4516.

217. Li, W., Xu, Z. J., Chu, R. Q., Fu, P. & Zang, G. Z. (2010). High piezoelectric d_{33} coefficient in $(Ba_{1-x}Ca_x)(Ti_{0.98}Zr_{0.02})O_3$ lead-free ceramics with relative high Curie temperature. *Materials Letters,* 64, 2325-2327.

218. Zhang, S. W., Zhang, H. L., Zhang, B. P. & Yang, S. (2010). Phase-transition behavior and piezoelectric properties of lead-free $(Ba_{0.95}Ca_{0.05})(Ti_{1-x}Zr_x)O_3$ ceramics. *Journal of Alloys and Compounds,* 506, 131-135.

219. Xue, D. Z., Zhou, Y. M., Bao, H. X., Gao, J. H., Zhou, C. & Ren, X. B. (2011). Large piezoelectric effect in Pb-free $Ba(Ti,Sn)O_3$-x$(Ba,Ca)TiO_3$ ceramics. *Applied Physics Letters,* 99.

220. Gallagher, P. K., Brown, M. E. & Kemp, R. B. (2007). *Handbook of thermal analysis and calorimetry: recent advances, techniques and applications*, (Ed.) ed. Netherlands: Elsevier Science and Technology.

221. Suryanarayana, C., & Norton, G. (1998). *X-Ray Diffraction: A Practical Approach*: Springer.

222. Van der Heide, P. (2011). *X-ray photoelectron spectroscopy: An introduction to principles and practices*: Wiley.

223. Nakamoto, K. (1986). *Infrared and Raman spectra of inorganic and coordination compounds*: Wiley.

224. Goldstein, J., Newbury, D. E., Joy, D. C., Lyman, C. E., Echlin, P., Lifshin, E., Sawyer, L. C. & Michael, J. R. (2007). *Scanning electron microscopy and X-ray microanalysis*: Springer.

225. Ye, Z. (2008). *Handbook of advanced dielectric, piezoelectric and ferroelectric materials: Synthesis, properties and applications*: Taylor & Francis.

226. Setter, N., & Colla, E. L. (1993). *Ferroelectric ceramics: tutorial reviews, theory, processing, and applications*: Birkhäuser.

227. Nair, K. M., Suvorov, D., Schwartz, R. W. & Guo, R. (2009). *Advances in electroceramic materials: Ceramic transactions*: John Wiley & Sons.

228. Yang, M.-R., Tsai, C.-C., Hong, C.-S., Chu, S.-Y. & Yang, S.-L. (2010). Piezoelectric and ferroelectric properties of CN-doped $K_{0.5}Na_{0.5}NbO_3$ lead-free ceramics. *Journal of Applied Physics,* 108, 094103-5.

229. Paula, A. J., Parra, R., Zaghete, M. A. & Varela, J. A. (2009). Study on the $K_3Li_2Nb_5O_{15}$ formation during the production of $(Na_{0.5}K_{0.5})(1\text{-}x)Li_xNbO_3$ lead-free piezoceramics at the morphotropic phase boundary. *Solid State Communications,* 149, 1587-1590.

230. Zhong, T., Tang, J., Zhu, M., Hou, Y., Wang, H. & Yan, H. (2005). Synthesis and characterization of layered niobate $K_4Nb_6O_{17}$ thin films by niobium-chelated precursor. *Journal of Crystal Growth,* 285, 201-207.

231. Heda, P. K., Dollimore, D., Alexander, K. S., Chen, D., Law, E. & Bicknell, P. (1995). A method of assessing solid state reactivity illustrated by thermal decomposition experiments on sodium bicarbonate. *Thermochimica Acta,* 255, 255-272.

232. Joseph, K., & Gnanasekaran, T. (1999). Thermoanalytical study of the reaction of potassium carbonate with ferric oxide. *Thermochimica Acta,* 342, 153-160.

233. Enzhu, L., Kakemoto, H., Wada, S. & Tsurumi, T. (2008). Enhancement of Q_m by co-doping of Li and Cu to potassium sodium niobate lead-free ceramics. *Ultrasonics, Ferroelectrics and Frequency Control, IEEE Transactions on,* 55, 980-987.

234. Liu, S. J., Wan, B., Wang, P. & Song, S. H. (2010). Influence of A-site non-stoichiometry on structure and electrical properties of $K_{0.5}Na_{0.5}NbO_3$-based lead-free piezoelectric ceramics. *Scripta Materialia,* 63, 124-127.

235. Pang, X., Qiu, J., Zhu, K. & Luo, J. (2011). Study on the sintering mechanism of KNN-based lead-free piezoelectric ceramics. *Journal of Materials Science,* 46, 2345-2349.

236. Mahajan, S., Thakur, O. P., Bhattacharya, D. K. & Sreenivas, K. (2009). Study of structural and electrical properties of conventional furnace and microwave-sintered $BaZr_{0.10}Ti_{0.90}O_3$ ceramics. *Journal of the American Ceramic Society,* 92, 416-423.

237. Zuo, R., Rödel, J., Chen, R. & Li, L. (2006). Sintering and electrical properties of lead-free $Na_{0.5}K_{0.5}NbO_3$ piezoelectric ceramics. *Journal of the American Ceramic Society,* 89, 2010-2015.

238. Malic, B., Jenko, D., Holc, J., Hrovat, M. & Kosec, M. (2008). Synthesis of sodium potassium niobate: A diffusion couples study. *Journal of the American Ceramic Society,* 91, 1916-1922.

239. Kissinger, H. E. (1957). Reaction kinetics in differential thermal analysis. *Analytical Chemistry,* 29, 1702-1706.

240. Bomlai, P., Wichianrat, P., Muensit, S. & Milne, S. J. (2007). Effect of calcination conditions and excess alkali carbonate on the phase formation and particle

morphology of $Na_{0.5}K_{0.5}NbO_3$ powders. *Journal of the American Ceramic Society,* 90, 1650-1655.

241. Du, Z. H., Zhang, T. S., Zhu, M. M. & Ma, J. (2010). PVP-mediated crystallization of perovskite phase in the PMN–PT thin films prepared by sol–gel processing. *Journal of the American Ceramic Society,* 93, 686-691.

242. Ye, Y., Yu, S., Huang, H. & Zhou, L. (2009). A polyethylene glycol-assisted route to synthesize $Pb(Ni_{1/3}Nb_{2/3})O_3$-$PbTiO_3$ in pure perovskite phase. *Journal of Alloys and Compounds,* 480, 510-515.

243. Liu, M., Yan, X., Liu, H. & Yu, W. (2000). An investigation of the interaction between polyvinylpyrrolidone and metal cations. *Reactive and Functional Polymers,* 44, 55-64.

244. Qian, X.-f., Yin, J., Feng, S., Liu, S.-h. & Zhu, Z.-k. (2001). Preparation and characterization of polyvinylpyrrolidone films containing silver sulfide nanoparticles. *Journal of Materials Chemistry,* 11, 2504-2506.

245. Bright, J. H., Drago, R. S., Hart, D. M. & Madan, S. K. (1965). Spectrochemical studies of a series of lactams as ligands with nickel(II) and chromium(III). *Inorganic Chemistry,* 4, 18-20.

246. Nakamoto, K. (1978). *Infrared and raman spectra of inorganic and coordination compounds*. New York: John Wiley and Sons.

247. Gniewek, A., Trzeciak, A. M., Ziółkowski, J. J., Kępiński, L., Wrzyszcz, J. & Tylus, W. (2005). Pd-PVP colloid as catalyst for Heck and carbonylation reactions: TEM and XPS studies. *Journal of Catalysis,* 229, 332-343.

248. Wei, Y., Li, L., Yang, X., Pan, G., Yan, G. & Yu, X. (2009). One-step UV-induced synthesis of polypyrrole/Ag nanocomposites at the water/ionic liquid interface. *Nanoscale Research Letters,* 5, 433 - 437.

249. Wang, D., An, J., Luo, Q., Li, X. & Li, M. (2008). A convenient approach to synthesize stable silver nanoparticles and silver/polystyrene nanocomposite particles. *Journal of Applied Polymer Science,* 110, 3038-3046.

250. Loría-Bastarrachea, M., Herrera-Kao, W., Cauich-Rodríguez, J., Cervantes-Uc, J., Vázquez-Torres, H. & Ávila-Ortega, A. (2011). A TG/FTIR study on the thermal degradation of poly(vinyl pyrrolidone). *Journal of Thermal Analysis and Calorimetry,* 104, 737-742.

251. Li, W., Xu, Z., Chu, R., Fu, P. & Zang, G. (2010). Piezoelectric and dielectric properties of $(Ba_{1-x}Ca_x)(Ti_{0.95}Zr_{0.05})O_3$ lead-free ceramics. *Journal of the American Ceramic Society,* 93, 2942-2944.

252. Naghib-zadeh, H., Glitzky, C., Dörfel, I. & Rabe, T. (2010). Low temperature sintering of barium titanate ceramics assisted by addition of lithium fluoride-containing sintering additives. *Journal of the European Ceramic Society,* 30, 81-86.

253. Pollet, M., & Marinel, S. (2003). Low temperature sintering of $CaZrO_3$ using lithium fluoride addition. *Journal of the European Ceramic Society,* 23, 1925-1933.

254. Roulland, F., Terras, R., Allainmat, G., Pollet, M. & Marinel, S. (2004). Lowering of $BaB'_{1/3}B''_{2/3}O_3$ complex perovskite sintering temperature by lithium salt additions. *Journal of the European Ceramic Society,* 24, 1019-1023.

255. Hennings, D. F. K., & Schreinemacher, H. (1995). Ca-acceptors in dielectric ceramics sintered in reductive atmospheres. *Journal of the European Ceramic Society,* 15, 795-800.

256. Babilo, P., Uda, T. & Haile, S. M. (2007). Processing of yttrium-doped barium zirconate for high proton conductivity. *Journal of Materials Research,* 22, 1322-1330.

257. E. Wu, *POWDMULT*. version 2.1 ed.; School of Physical Sciences: Flinders University of South Australia. Bedford Park. South Australia 5042.